

Flow Induced Crystallization of Polymers

Application to Injection Moulding

CIP DATA LIBRARY TECHNISCHE UNIVERSITEIT EINDHOVEN

Zuidema, Hans

Flow induced crystallization of polymers, application to injection moulding/
by Hans Zuidema. – Eindhoven: Technische Universiteit Eindhoven, 2000.

Thesis – 126p.– with references – with index – with summary in Dutch.

ISBN 90-386-3021-2

NUGI 841

Subject headings: Flow-induced crystallization kinetics, recoverable strain, specific volume,
high cooling rates, injection moulding, dimensional stability.

Copyright © 2000 H. Zuidema

All rights reserved. No part of this book may be reproduced, stored in a database or retrieval
system, or published, in any form or in any way, electronically, mechanically, by print, pho-
toprint, microfilm or any other means without prior written permission of the publisher.

This thesis was prepared with the L^AT_EX 2_ε document preparation system.
Printed in the Netherlands

Flow Induced Crystallization of Polymers

Application to Injection Moulding

Proefschrift

ter verkrijging van de graad van doctor aan de
Technische Universiteit Eindhoven,
op gezag van de Rector Magnificus, prof.dr. M. Rem,
voor een commissie aangewezen door het
College voor Promoties
in het openbaar te verdedigen op
donderdag 7 september 2000 om 16.00 uur

door

Hans Zuidema

geboren te Steenwijk

Dit proefschrift is goedgekeurd door de promotoren:

prof.dr.ir. H.E.H. Meijer
en
prof.dr. P.J. Lemstra

Copromotor:

dr.ir. G.W.M. Peters

Contents

| | |
|--|-----------|
| Summary | vii |
| Notation | ix |
| 1. Introduction | 1 |
| 1.1 Crystallization of polymers related to processing: an overview | 1 |
| 1.1.1 Molecular configuration, conformation and flow | 1 |
| 1.1.2 Crystallization | 2 |
| 1.1.3 Modeling | 4 |
| 1.1.4 Relation with other material properties | 5 |
| 1.1.5 Processing | 6 |
| 1.1.6 Mechanical properties | 6 |
| 1.2 Thesis' objective and overview | 7 |
| 2. Modeling aspects | 9 |
| 2.1 Governing equations | 10 |
| 2.2 Modeling injection moulding | 13 |
| 2.3 Crystallinity | 14 |
| 2.3.1 Viscosity | 14 |
| 2.3.2 Solid layer position | 14 |
| 2.4 Conclusion | 16 |
| 3. Development of a strain based model for flow-induced crystallization | 17 |
| 3.1 Crystallization kinetics equations | 18 |
| 3.2 Experimental results | 20 |
| 3.2.1 Quiescent experiments | 20 |
| 3.2.2 Short term shear experiments | 21 |
| 3.2.3 Steady state experiments | 22 |
| 3.3 Modeling results | 22 |
| 3.3.1 Quiescent experiments | 22 |
| 3.3.2 Short term shear experiments: structure correlation with viscoelastic properties | 23 |
| 3.3.3 Steady state experiments: validation | 26 |
| 3.4 Formulation of a recoverable strain based crystallization model | 31 |
| 3.5 Qualitative validation of the model | 32 |
| 3.6 Discussion | 39 |
| 4. Influence of Cooling Rate on pVT-behavior of Semi-Crystalline Polymers | 41 |
| 4.1 Methods | 44 |

| | | |
|-------|--|-----|
| 4.2 | Results and discussion | 48 |
| 4.3 | Conclusions | 55 |
| 5. | <i>Injection moulding</i> | 57 |
| 5.1 | Experimental analysis | 57 |
| 5.1.1 | Experimental description | 57 |
| 5.1.2 | Experimental results | 58 |
| 5.2 | Numerical analysis | 62 |
| 5.2.1 | Introduction | 62 |
| 5.2.2 | Choice of criteria | 63 |
| 5.2.3 | Morphological sensitivity due to processing conditions | 66 |
| 5.3 | Discussion on dimensional stability | 68 |
| 5.3.1 | Towards an accurate model evaluation | 68 |
| 5.3.2 | The SCORIM process | 69 |
| 5.4 | Conclusion | 71 |
| 6. | <i>Discussion and conclusions</i> | 73 |
| 6.1 | Crystallization | 73 |
| 6.2 | Modeling | 73 |
| 6.3 | Flow-induced crystallization modeling | 74 |
| 6.4 | pVT experiments | 74 |
| 6.5 | Injection moulding | 75 |
| | <i>Bibliography</i> | 77 |
| A. | <i>Material characterization</i> | 85 |
| A.1 | Polyamide 6 | 85 |
| A.2 | Polypropylene (KS10, Borealis) | 86 |
| A.3 | Polypropylene (K2Xmod, Borealis) | 88 |
| B. | <i>Experimental results</i> | 95 |
| C. | <i>Numerical results</i> | 101 |
| | <i>Samenvatting</i> | 107 |
| | <i>Acknowledgments</i> | 111 |
| | <i>Curriculum Vitae</i> | 113 |

Summary

The final properties of a product, produced from semi-crystalline polymers, are to a great extent determined by the internal structure, which itself is established during processing. A complete modeling, providing the means for predicting the final product properties, is still not available. This study presents two important parts of that modeling, which are implemented in a computer code for the numerical simulation of the injection moulding process; (i) a flow-induced crystallization model, based on the recoverable strain in the melt and, (ii) a new experimental technique to determine the specific volume of semi-crystalline polymers, and its relation to cooling rate dependent crystallization kinetics.

Since nucleation and growth of spherulitical structures during cooling of semi-crystalline polymers has been adequately modeled, the structure distribution resulting from different processing conditions, like cooling rate and pressure, can be predicted. In contrast, the development of flow-induced structures is less clear yet. In this thesis, a shear rate based model and a new recoverable strain based model are implemented in our injection moulding simulation code VIp. Based on data of a fully characterized polyamide and polypropylene grade, numerical simulations of quiescent, startup flow and steady state flow experiments have been performed. Results are compared with experiments from the literature. The differences between both models have been studied and compared with some typical phenomena observed. Besides performing better in (at least qualitatively) predicting all phenomena, the new model is a strain based model that can be linked to molecular parameters and, therefore, should be given preference.

An accurate description of the specific volume is needed to predict differential shrinkage during and after moulding, which causes pressure - and thermally - induced stresses and controls the dimensional accuracy and long term dimensional stability. For amorphous polymers, for which often it can be assumed that cooling rate dependence can be ignored, standard techniques enable measurements of the specific volume as a function of temperature and pressure. For semi-crystalline polymers the situation is more complicated, since the specific volume depends strongly on the degree of crystallinity, which itself depends on the thermo-mechanical history, i.e. temperature and pressure for quiescent crystallization. This requires the use of a combined experimental-numerical technique to interpret the data and to determine the specific volume. Standard equipment can only be used at relatively low cooling rates. Since high cooling rates combined with high pressure are present during injection moulding, improved experimental techniques have to be designed. A setup based on the confining fluid technique has been build, which can reach cooling rates up to $60[K s^{-1}]$ and pressures up to $20 \cdot 10^6[Pa]$. During an experiment, the specific volume is measured together with the temperature history and pressure. Using an accurate model to calculate the crystalline structure, together with a specific volume model, which depends on this structure,

enables the determination of model parameters. Comparing both the measurements and the model predictions, led to the conclusion that modeling of the crystallization kinetics results in accurate predictions of the specific volume.

Both parts of the modeling have been used in numerically simulating processing steps for semi-crystalline polymers. Since the injection moulding process has served as an example for the influence of processing conditions on the structure distribution in the product, the complete injection moulding cycle, from the filling stage up to ejection has been modeled. Both the new strain based model for flow-induced crystallization, and the new approach to determine the specific volume of semi-crystalline polymers, have been applied in predicting internal structures (i) as resulting from the SCORIM process (which is a specific procedure ('push-pull') during cooling to enhance mechanical properties like strength and stiffness), (ii) as present in a moulded strip (as a function of different processing conditions) and, finally, (iii) in their relation with long-term dimensional stability. The SCORIM process emphasizes the influence of flow history, experienced by the polymer melt, on the resulting structure distribution, i.e. the presence of flow-induced oriented layers. Since processing conditions, like the temperature of the melt injected, the mould wall temperature and the volume flux during filling, have a large influence on the structure distribution, an experimental and numerical study have been performed for their quantification. General trends are: (i) a higher temperature of the melt and (ii) a higher volume flux both decrease the thickness of the flow-induced oriented layer, while (iii) increasing the temperature of the mould wall has only negligible influence. Despite, some influence on final shrinkage was, experimentally, found.

Since the structure distribution in a polymer product can be calculated, shrinkage data concerning both the spherulitical and flow-induced structures are necessary to predict the dimensional stability of semi-crystalline polymer products. Because these are not available at this time, predictions on dimensional stability are left for the future.

Notation

Operators and functions

| | |
|-------------------------|--------------------------------|
| $\vec{\nabla}$ | the gradient operator |
| \dot{a} | the material derivative |
| \mathbf{A}^c | a conjugation |
| \mathbf{A}^d | the deviatoric part |
| \mathbf{A}^{-d} | the deviatoric part of inverse |
| \mathbf{A}^{-1} | an inverse |
| $\vec{a} \cdot \vec{b}$ | a dot product |
| $tr(a)$ | the trace |
| $exp(a)$ | e^a |
| $ \vec{a} $ | the vector length |

Material properties

| | |
|------------|---|
| ρ | the density |
| η | the viscosity |
| η_ξ | the viscosity influenced by the crystal structure |
| v | the specific volume |
| λ | the thermal conductivity |
| c_p | the thermal capacity |
| G' | the storage modulus |
| G'' | the loss modulus |

List of symbols

| | |
|------------------|----------------------|
| $\dot{\epsilon}$ | the deformation rate |
| γ | the shear |
| $\dot{\gamma}$ | the shear rate |
| $\dot{\gamma}_w$ | the wall shear rate |

| | |
|---------------|--|
| η_j | the Leonov viscosity for the j-th mode |
| θ_j | the Leonov relaxation time for the j-th mode |
| θ_{j0} | the relaxation time for the j-th mode at the reference temperature |
| a | the proportionality factor for the crystal growth rate to the pressure |
| $a_T(T)$ | the time-temperature shift function |
| e | the specific internal energy |
| p | the pressure |
| r_h | the specific heat source |
| t | the time |
| t_s | the shear time |
| G_j | the Leonov modulus for the j-th mode |
| J_2 | the second invariant |
| T | the temperature |
| T_g | the glass transition temperature |
| T_m | the melting temperature |
| T_w | the wall temperature |
| Q | the volume flux |

Vectors and tensors

| | |
|---------------------------|---|
| σ | the Cauchy stress tensor |
| σ_e | the elastic Cauchy stress tensor |
| τ_e | the deviatoric part of the elastic Cauchy stress tensor |
| \vec{f} | the specific (i.e. per unit mass) body force |
| \vec{h} | the heat flux vector |
| \vec{v} | the velocity vector |
| \vec{v}^* | the velocity parallel to the mid-plane of the cavity |
| \vec{x} | the position vector |
| x_3^ϵ | the local thickness coordinate |
| \vec{R} | the chain end-to-end vector |
| \mathbf{B} | the Finger tensor |
| \mathbf{B}_e | the elastic Finger tensor |
| $\overline{\mathbf{B}}_e$ | the volume invariant elastic Finger tensor |
| \mathbf{D} | the rate of deformation tensor |
| \mathbf{F} | the deformation gradient tensor |
| \mathbf{F}_e | the elastic deformation gradient tensor |

| | |
|----------------------|--|
| $\bar{\mathbf{F}}_e$ | the volume invariant elastic deformation gradient tensor |
| \mathbf{F}_p | the plastic deformation gradient tensor |
| \mathbf{I} | the unit tensor |
| \mathbf{L} | the velocity gradient tensor |
| \mathbf{L}_e | the elastic part of the velocity gradient tensor |
| \mathbf{L}_p | the plastic part of the velocity gradient tensor |
| \mathbf{S} | the orientation configuration tensor |
| \mathbf{W} | the spin tensor |

Crystallization parameters

| | |
|------------------|---|
| α | the nucleation rate |
| $\dot{\gamma}_l$ | a typical value for the shear rate for the shish growth |
| $\dot{\gamma}_n$ | a typical value for the shear rate for the spotlike nuclei formation |
| τ_l | the relaxation time for the shish |
| τ_n | the relaxation time for the nuclei |
| ϕ_0 | the undisturbed total volume of the spherulites per unit of volume |
| ϕ_1 | the total surface of the spherulites per unit of volume |
| ϕ_2 | 4π times the sum of the radii of the spherulites per unit of volume |
| ϕ_3 | 8π times the number of the spherulites per unit of volume |
| ψ_0 | the undisturbed total volume of the shish-kebabs per unit of volume |
| ψ_1 | the total surface of the shish-kebabs per unit of volume |
| ψ_2 | 4π times the total length of the shish per unit of volume |
| ψ_3 | 8π times the number of the nuclei per unit of volume |
| ξ | the degree of crystallinity |
| ξ_g | the degree of space filling according to the geometrical approach |
| g_l | a parameter for the shish |
| g_n | a parameter for the nuclei |
| G | the crystal growth rate |
| H | the heat of crystallization |
| L_{tot} | the total length of the shish per unit of volume |
| R_{tot} | the total radius of the spherulites per unit of volume |
| S_{tot} | the total surface of the structure per unit of volume |
| V_{tot} | the total volume of the structure per unit of volume |
| N | the number of spherulites |
| N_f | the number of shish-kebabs |

V_{∞} the maximum degree of crystallinity

Chapter 1

Introduction

The final properties of a product, produced from semi-crystalline polymers, are to a great extent determined by the internal structure, which itself is established during processing of that product. For example, flow gradients act as a source for viscoelastic stresses, which can enhance nucleation and crystallization, not only accelerating the process, but also leading to different types of crystalline structures. A complete modeling, providing the means for predicting the final product properties, is still not available. This study presents two important parts of that modeling; (i) a flow-induced crystallization model, based on the recoverable strain in the melt and, (ii) a new experimental technique to determine the specific volume of semi-crystalline polymers, and its relation to cooling rate dependent crystallization kinetics. Both are implemented in a computer code for the numerical simulation of the injection moulding process, and validated by comparing the predicted results with well defined experiments (partly from literature). Applications are found in predicting internal structures (i) as resulting from the SCORIM process (which is a specific procedure ('push-pull') to enhance mechanical properties like strength and stiffness), (ii) as present in a moulded strip (as a function of different processing conditions) and, finally, (iii) in their relation with long-term dimensional stability.

Crystallization of polymers is influenced by the thermo-mechanical history during processing. Dependent on the amount of strain experienced during flow, the number and type of the nuclei formed will be different, and so will be the final crystalline structure. For example, in the injection moulding process, the absence of shear in the center of a product results in a spherulitical structure, while in the highly strained regions at the cavity walls an oriented structure (in polyolefins often referred to as 'shish-kebabs') can be present (fig. 1.1). To clarify the role of the processing conditions on the crystallization process (and, vice versa, the role of the growing crystal structure on processing behavior), a short overview will be presented concerning their mutual interactions.

1.1 Crystallization of polymers related to processing: an overview

1.1.1 Molecular configuration, conformation and flow

The molecular configuration of polymer materials determines the materials ability for ordering. Three types of molecular structures are generally distinguished: isotactic, all side groups are present at one side of the backbone of the polymer chain; syndiotactic, with alternating side groups; and atactic, with randomly positioned side groups. Crystallization is possible if the chain is symmetric or has only small side groups, which fit in a regularly packed confor-



Fig. 1.1: A cross section of a product. After (44).

mation; the polymer chain has to be linear and stereo specific. Therefore, isotactic polymers have the ability to crystallize; syndiotactic polymers might have this ability, depending on the side groups, while atactic polymers can not crystallize. The influence of isotacticity on the crystallization kinetics during quiescent crystallization has been studied by, for example, Janimak (41).

Polymer molecules, in general, show a random configuration without any orientation, when in solutions or melts. However, their state (conformation and orientation) can be altered by flow gradients, i.e. by stirring solutions or shearing melts. According to Keller (48) only two stages of orientation exist; the fully random and the fully stretched chain, with no stable intermediate stages. The transition from one stage to the other is assumed to be sharp, showing a molecular weight dependent coil-stretch transformation at a critical strain rate and temperature. Thus, with gradually increasing the elongational rate, first only small differences in the chain conformation will appear, but once a critical elongational rate has been reached, the chain will switch to the almost fully stretched stage of the conformation ($\dot{\epsilon}\theta > 1$, with $\dot{\epsilon}$ the deformation rate and $\theta = \theta(M_w, T, \dots)$ the relaxation time). Moreover, not only has the critical elongational rate to be reached, it must be maintained for a certain time as well ($\dot{\epsilon}t > 1$, with t the deformation time). The structures observed in solutions or melts, all are the result of a combination of both these stages.

1.1.2 Crystallization

The crystallization behavior of polymers is determined by their ability to form ordered structures; the configuration determines the conformation, which is influenced by the processing conditions. Crystallization under quiescent conditions is a phase transformation process, which is caused by a change in the thermodynamic state of the system. This change can be a lowering of the temperature or a change in the hydrostatic pressure. In flow, chain extension can occur as explained in the preceding section. Thermodynamically, chain extension will increase the opportunity of crystal formation by increasing the melting point, while kinetically the extended chain is closer to a crystal state than a random chain. By stretching the polymer chains, the rate of crystallization increases. Dependent on the conformation of the

polymer chain, two types of crystals can be formed; the random polymer chain will lead to lamellar, chain folded crystals that finally form spherulites, while the fully extended chain will lead to extended chain crystals, finally resulting in shish-kebab structures (Keller (48)). It has been shown, e.g. by Bashir (2) and Mackley (62), that the high end tail of the molecular weight distribution promotes the formation of extended chain crystals. Following Bashir (2), these high end tail molecules are stretched out while the rest remains practically unchanged; a stronger elongational rate results in a broader part of the molecular weight distribution to be extended. The elongational rate, therefore, determines the amount of oriented molecules (extended chain crystals) present. These extended chain crystals themselves are inadequate to influence the material properties, given their limited number. However, they serve as nuclei for lamellar crystallization of the not oriented lower molecular bulk, which will show lamellar over-growth at a later stage, perpendicular to the central core (Bashir (2)). The structure formed is called a shish-kebab. It has been shown by Petermann (67) that the number of core crystals, nucleated at a specific temperature, depends on the external strain. The core itself consists of a shish-kebab structure on a finer scale (Keller (48)).

A certain strain and strain rate have to be present for shear flow to induce (noticeable) crystallization. After a nucleus has been formed, continuous crystallization of polymers is kinetically controlled, the motion involved refers to the transport of molecules from the disordered liquid phase to the ordered solid phase, and to the rotation and rearrangement of the molecules at the surface of the crystal, similar to quiescent crystallization. The crystallization process can thus be subdivided into three stages:

Nucleation: Nucleation can have different causes like overall nucleation from a nucleation agent, pressure induced nucleation, strain induced nucleation and cooling. The nuclei formed act as starting points for polymer crystallization. There is no complete agreement on the physical background of the nucleation process. For example, Terrill et al. (81) considered, based on experimental evidence (WAXD and SAXS), the nucleation event during spinning of isotactic polypropylene to be the result of density fluctuations, although a repetition of old discussions on the true interpretation of combined WAXD and SAXS data¹ question these results. Even without considering the basic underlying physics precisely, in case of flow, nuclei can be created by flow-induced ordering phenomena in the melt, while the nucleation process for a quiescent melt can be described by a Poisson point process (Janeschitz-Kriegl (40)). For polymers containing nucleation agents, also clustered point processes have some importance.

Growth: The nuclei grow, dependent on the thermo-mechanical history which they experience; if the nuclei are sufficiently strained they will grow into threads, otherwise they stay spherical and will further grow radially. In these, so called spherulites, the lamellae are present like twisted spokes in a sphere, while thread-like nuclei grow mainly perpendicular to the thread (fig. 1.2).

Perfection: Perfectioning is the process of improvement of the interior crystalline structure of the crystalline regions. This is also referred to as secondary crystallization.

¹ In this case the discussion concentrates on whether or not the sensitivity of both methods has an influence on the observations made.

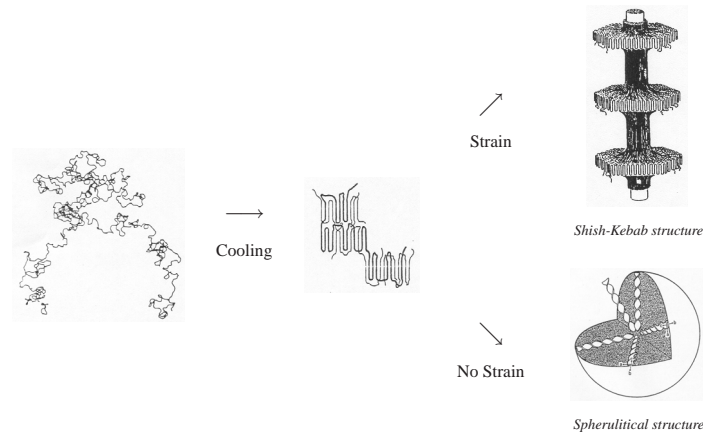


Fig. 1.2: A schematic outline of the concept of crystallization. After (48) and (55).

1.1.3 Modeling

Historically, crystallization transformations are described by using a phase diagram assuming the transformation to be in a quasi-equilibrium state, leading to a front model. An example of this approach is the description of the growth of the ice layer on the polar sea (a Stefan-problem (78)). It has been shown by Berger (5), that the front model is inadequate in describing solidification, if the process is governed by the kinetics of a phase change. For example, the occurrence of completely amorphous layers can never be understood using a front model. A zone model has to be used, where a phase change (crystallization) determines the solidification behavior. Crystallization in a moving zone takes place when the characteristic time of heat diffusion is less than the characteristic time of crystallization. In the limiting case of very fast crystallization, compared with the process of heat conduction, the zone model shows a transition into the front model.

Quiescent crystallization: Describing the growth of the crystalline spherulites in case of quiescent crystallization has been done by representing the spherulites as spheres (Schultz (75)). Spherulitical growth is then accounted for by enlarging the sphere radius. However, the crystallizing medium is limited by free surfaces or other boundaries that induce truncations of crystalline entities and locally modify the crystallization kinetics. Benard (4) formulated a mathematical description for the growth of already existing nuclei and concluded that the kinetics clearly are the controlling factor in the systems investigated. A more complete model for quiescent crystallization has been described by Janeschitz-Kriegl (39), which is based on the Kolmogoroff equation (Kolmogoroff (49)), who formulated the crystallization kinetics in terms of time dependent (bulk) nucleation and crystal growth rate. This formulation has been extended for the influence of confining surfaces and surface nucleation processes by Eder (15; 16). A Poisson point process with special intensity measures for the description of the nucleation process and a deterministic law for crystal growth forms the basis. Using the method proposed by Schneider (74), this generalized Kolmogoroff equation can be trans-

formed in a set of differential equations (Schneider's rate equations), which give a complete description of the crystalline structure. These rate equations are coupled with the energy equation by the source term, which takes into account the latent heat when the polymer crystallizes (Eder (17)).

Flow-induced crystallization: An onset for the description of flow-induced structures has been given by Eder et al. (19), who based their theory on the shear rate as the driving force for crystallization. Their model for flow-induced crystallization resembles their model for quiescent crystallization. It is assumed that the influence of the deformation on crystallization, is due to the formation of thread-like nuclei (shish), on which lamellae grow mainly perpendicular (kebabs). This model is described in chapter 3 of this thesis. Jerschow (45) used this model in analyzing the structure distribution found in isotactic polypropylene, after fast short term shear at low degrees of super-cooling. Besides a flow-induced (shish-kebab) structure at the surface and a spherulitical structure in the center, in between both layers a fine grained layer has been observed. It has been suggested that this layer consists of thread-like structures perpendicular to the flow direction. A model based on the conformation of the molecules in the melt has been proposed by Bushman (8) and Doufas (12), which includes a conformation tensor (the driving force, calculated using a viscoelastic model), an orientation tensor and the degree of crystallinity. No description is available, however, of the final structure (size of structures, etc.). Other models have been proposed by Ito (37), based on the strain present in the melt, and by Verhoyen (86), based on the Cauchy stress. An iso-kinetic approach is used in models based on the Nakamura equations (Nakamura (66)) by Isayev (35) and Guo (29). The (dis)advantages of all these models are discussed in chapter 3.

1.1.4 Relation with other material properties

The evolution of structure (spherulites and shish-kebabs) will influence the material properties. The most severe effects are observed in the viscosity and the specific volume. Effects in other properties like the thermal conductivity and thermal capacity will not be discussed here.

Viscosity: The coupling between the crystal structure and the viscosity of a polymer melt, is not fully clarified yet. For example, in startup flow experiments, it has been observed by Lagasse (52) that a sudden rise in the viscosity correlates with the appearance of crystals in the sheared melt. Experiments by Vleeshouwers (87) showed the same kind of behavior. Initially, the melt still shows an amorphous behavior, since the amount of crystalline material (or the number of crystals) is very low. With increasing amount (or number) the influence on the viscosity will increase. Guo et al. (27) assumed that the melt loses its fluidity upon the occurrence of crystallization, i.e. a step-like change in the viscosity. They do not give a physical explanation although; one could assume that a network occurs in this stage. Another possibility could be, that the crystals form a separate phase in the amorphous melt. The rheology will then be changed like is known from dispersion rheology (see for example Ito (36) and Verhoyen (85)).

Specific volume: In polymer processing, the specific volume is influenced by processing characteristics like temperature, pressure and flow history, and it determines shrinkage which expresses itself by dimensional (in)stability. For amorphous polymers, the pressure and temperature history determine the specific volume and (frozen in) molecular orientation determines the anisotropic dimensional instability via (slow) relaxation processes below the glass transition temperature (Meijer (65)). For semi-crystalline polymers, however, the specific volume is also influenced by the crystalline structure. This structure itself is influenced by the pressure and the temperature history, by the configuration of the polymer chains and flow induced ordering phenomena as well. Consequently, for semi-crystalline polymers the specific volume has to be related to pressure, temperature, cooling rate and the crystalline state (Zuidema (94)). For a correct modeling of the injection moulding of semi-crystalline polymers, accurate measurements and modeling of the specific volume have to be achieved not only in relation to the pressure and temperature, but also to the cooling rate and ordered state of the molecules. This conclusion is subscribed by Fleischmann (22), regarding the influence of the processing conditions on the specific volume. The specific volume will be discussed in more detail in chapter 4.

1.1.5 Processing

For polymer melts it has been observed (Van der Vegt (83)) that the flow through a capillary die can become blocked by crystal formation, induced by the elongational flow at the constriction. Bashir (2; 3) and Keller (48) explored these findings somewhat further and observed a macroscopical rheological effect in capillary flow of high molecular weight polyethylenes; a reduced flow resistance coupled with the absence of extrudate distortions when extruding a polymer melt in a specific processing window. Experiments by Tas (80) showed that, during film blowing of LDPE films, the viscoelastic stresses at the freeze line determine the majority of the mechanical properties by directing the crystallization. Saiu (71) performed an experimental study on the influence of injection moulding conditions on product properties for an isotactic polypropylene. Chiang (11) studied shrinkage, warpage and sink marks resulting from the injection moulding process, using semi-crystalline polymers. The effect of crystallization on the mechanical and physical properties has been studied, for isotactic polypropylenes with different molar masses. It has been observed (Guo (28)) that increasing the injection speed or the melt injection temperature leads to a decrease in the thickness of the flow-induced layer. The complicated thermo-mechanical history, in all these examples, requires a numerical analysis. The effect of processing conditions will be discussed in more detail in chapter 5.

1.1.6 Mechanical properties

The resulting morphology of the product is, together with the molecular composition, the factor determining the mechanical and dimensional properties. Because the solidification behavior of amorphous polymers is quite well understood, prediction of warpage and shrinkage from ejection up to the complete life cycle of a product can be done (Caspers (9), Meijer (65)). This knowledge allows one to reduce shrinkage and warpage by choosing a different polymer

(with different relaxation time/molecular weight (distribution)) by adjusting the processing conditions, or by improving the mould design. For semi-crystalline polymers, the different crystalline structures present (spherulites and/or shish-kebabs) have a different influence on secondary crystallization and physical aging. The mechanical properties of semi-crystalline polymers improve with increasing the amount of long polymer chains that function as 'tie-molecules' between crystals. Also, a preferred molecular orientation in a product enhances the properties in the orientation direction, while perpendicular the properties reduce. An extreme example is the fiber spinning process of HPPE (High Performance Polyethylene fibers), where all molecules are aligned along the thread.

An attempt to quantify the influence of injection moulding processing conditions on the mechanical properties has been performed by Fleischmann (23) who studied the effect of molecular orientation on the tensile behavior of an isotactic polypropylene. The application of packing pressure, the distance from the gate and the orientation of the testing direction relative to the chain orientation, all proved to influence the tensile behavior. Hsiung (34) showed that with decreasing the injection speed, the elongation to break, tensile strength and impact strength increase in injection moulded dumbbells. Gahleitner (25) investigated the influence of the molecular structure on the crystallinity and mechanical properties for two different polypropylene homopolymers, as influenced by their molar mass and heterogeneous nucleation, and he studied (24) the influence of processing on physical ageing. Additional to the generally observed correlation between mechanical properties and spherulite size, it has been shown that mechanical properties are influenced by the formation of highly oriented skin layers through shear induced crystallization. Based on these considerations, we conducted a number of, relatively extreme, experiments at the Borealis laboratory in Linz in cooperation with Markus Gahleitner. Rectangular plates were injection moulded using an isotactic polypropylene. Different injection temperatures, mould temperatures and volume fluxes during filling were applied in order to study their influence on the resulting morphology and the mechanical properties. One of the conclusions was that the strongest effect on skin layer thickness and shrinkage resulted from a change in the melt temperature. Results are discussed in chapter 5. Generally, they are in line with previous examinations at the same polymer. Gahleitner (24) earlier also concluded that an increased melt temperature reduces shrinkage. Moreover, he found that an increased wall temperature only weakly reduces shrinkage, while an increased volume flux during filling reduces shrinkage. Density near the injection gate was higher than far from the gate, while stiffness was higher in longitudinal compared to the transverse direction. Ageing has shown to follow a log-linear behavior, as was confirmed by Fiebig (21). Jansen (42) found that a variation of holding pressure affects both longitudinal and transverse shrinkage.

1.2 Thesis' objective and overview

The main objective of this thesis is to predict the structure distribution during injection moulding in dependence of polymer parameters and processing conditions of semi-crystalline polymers, given its direct relevance to dimensional stability and mechanical properties. Different models that describe (flow-induced) crystallization of semi-crystalline polymers are implemented in our software code VIp (Polymer Processing & Product Properties Prediction Pro-

gram, Caspers (9)). A new model is proposed, based on the molecular conformation in the melt, i.e. the recoverable strain, as expressed by the highest relaxation time using the second invariant of the Finger tensor, and it replaces the until now used process parameter, the shear rate. The development and validation of this model for flow-induced crystallization is elucidated in chapter 3. Specific volume depends strongly on the crystalline structure and represents, therefore, an interesting material property. In chapter 4 the standard methods used to measure the specific volume are summarized and their deficiencies when used to characterize semi-crystalline polymers are discussed. A new experimental setup is proposed, able to measure specific volumes of semi-crystalline polymers dependent on both cooling rate and pressure applied. A model is proposed that relates structure distribution to specific volume. Combining the set of equations that describe crystalline structure development, with the model for specific volume and using our injection moulding simulation software VIp, we are, finally, able to try to study the influence of processing variables, as they influence the structure distribution (chapter 5). The thesis ends with a short discussion and recommendations for future research (chapter 6).

Chapter 2

Modeling aspects

Since factors influencing the structure distribution and mechanical properties cover the whole range of polymer processing conditions, identified by complex thermo-mechanical histories, numerical simulations are necessary to be able to study their interactions. Changes in processing conditions, like e.g. in injection moulding the temperature of the melt injected or the flux during filling, proved to have a yet unpredictable influence on the structure distribution in the final product. Numerical simulations generally enable the determination of the kinematics of the flow and can successfully be combined with crystallization kinetics.

Injection moulding is a widely used production process for large series of geometrically complex, thin walled products. Few geometrical limitations to products design exist, and different materials can be processed. Thermoplastic crystalline polymers are frequently used for the manufacturing of polymer parts and form, by value, the most important group of polymeric materials. In contrast with the rather severe conditions during processing (e.g. large thermal gradients, high pressures, large deformation rates) knowledge of material behavior assessed through standard characterization equipment is restricted to a relatively narrow temperature regime, and small windows of time and deformation rate. For amorphous polymers, the thermo-mechanical history has a, relatively, limited influence on the final performance as compared to semi-crystalline polymers where different crystal structures appear as a result of different thermo-mechanical histories. Moreover, the crystal structure present has a rather vague influence on material properties like specific volume on the one hand and viscosity on the other hand. From a technological point of view the morphology of the solidified product is, together with the molecular composition, the main determining parameter in the resulting mechanical properties, with differences in morphology being the cause for product variability. In addition, the morphology also determines the product's long-term behavior, such as dimensional stability and proneness to crack formation.

Studying moulding processes over the years in our group resulted in the simulation code VIp, a program for the numerical simulation of all stages of different moulding processes, like injection moulding, gas-assisted injection moulding, multi-material injection moulding, reaction injection moulding, resin transfer moulding and related processes, focusing on the qualitative prediction of the resulting material properties (Boshouwers & van der Werf (7), Caspers (9), Douven (14), Haagh (30), Sitters (76), Zoetelief (89)). In the VIp code, the general balance equations are solved together with boundary conditions for the process and constitutive equations for the materials involved (section 2.1). As an extension, in this thesis, different models for structure development during processing are included. They are dis-

cussed in chapter 3. The existing possibilities of particle tracking (Zoetelief (89)) are now used to track the (development of the) crystalline structures. Decoupled from the basic injection moulding simulation, flow-induced recoverable strain and orientation are calculated using the kinematics from the viscous flow simulation (section 2.1). The different modeling aspects are shortly discussed in section 2.2, while interactions between crystalline structure and polymer properties are discussed in section 2.3.

2.1 Governing equations

The balance equations read

$$\dot{\rho} + \rho \vec{\nabla} \cdot \vec{v} = 0 \quad (2.1)$$

$$\vec{\nabla} \cdot \boldsymbol{\sigma}^c + \rho \vec{f} = \rho \vec{v} \quad (2.2)$$

$$\boldsymbol{\sigma} = \boldsymbol{\sigma}^c \quad (2.3)$$

$$\rho \dot{e} = \boldsymbol{\sigma} : \mathbf{D} - \vec{\nabla} \cdot \vec{h} + \rho r_h \quad (2.4)$$

in which ρ is the density, \vec{v} is the velocity vector, $\boldsymbol{\sigma}$ is the Cauchy stress tensor, \vec{f} is the specific (i.e. per unit mass) body force, \mathbf{D} is the rate of deformation tensor, e is the specific internal energy, \vec{h} is the heat flux vector and r_h is the specific heat source. The balance equations are completed with constitutive equations for the Cauchy stress tensor $\boldsymbol{\sigma}$, the heat flux vector \vec{h} and the specific internal energy e as a function of the density ρ , the temperature T and the velocity vector \vec{v} . Generalized Newtonian flow behavior is assumed for the Cauchy stress tensor $\boldsymbol{\sigma}$:

$$\boldsymbol{\sigma} = -p\mathbf{I} + 2\eta\mathbf{D}^d \quad (2.5)$$

$$\eta = \eta(p, T, \mathbf{D})$$

in which p the pressure and \mathbf{D}^d the deviatoric part of the rate of deformation tensor. The only parameter left is the viscosity function, for which several models can be used. For the heat flux vector \vec{h} , Fourier's law is used:

$$\vec{h} = -\boldsymbol{\lambda} \cdot \vec{\nabla} T = -\lambda \mathbf{I} \cdot \vec{\nabla} T \quad (2.6)$$

$$\lambda = \lambda(p, T)$$

in which $\boldsymbol{\lambda}$ is the thermal conductivity tensor. The specific internal energy e can be expressed as

$$\dot{e} = c_p \dot{T} + \frac{p}{\rho^2} \dot{\rho} + \frac{T}{\rho^2} \left(\frac{\partial \rho}{\partial T} \right)_p \dot{p} \quad (2.7)$$

$$c_p = c_p(p, T)$$

under assumption that the elasticity has a negligible contribution to the mechanical dissipation; c_p is the thermal capacity at constant hydrostatic pressure. The constitutive equations

concerning (flow-induced) crystallization are discussed in more detail in chapter 3 and those for the specific volume in chapter 4.

We adapt the concept of thermo-rheological simple materials. This implies that the storage and loss modulus curves, measured at a reference temperatures, can be shifted along the logarithmic time axis. The shift depends on the temperature difference between the master curve and the curve that has to be shifted. Thus

$$\theta_j = a_T(T)\theta_{j0} \quad (2.8)$$

in which $a_T(T)$ is the time-temperature shift function and θ_{j0} is the relaxation time for the j -th component at the reference temperature for the master curve. The shift function $a_T(T)$ can be described using the WLF-equation if $T \geq T_g$:

$$\log(a_T(T)) = \frac{C_1(T - T_0)}{C_2 + T - T_0} \quad (2.9)$$

while below T_g

$$a_T(T) = a_T(T_g) \quad (2.10)$$

In order to predict flow-induced (recoverable) strain and orientation, expressions for the evolution of the recoverable strain are incorporated in VI_p. The total set of resulting equations is solved, as usual, in a decoupled way. Thus the balance equations are solved using a generalized Newtonian model for the stresses and, subsequently, using the computed velocity gradient tensor \mathbf{L} , the recoverable strain is determined from a viscoelastic model. Baaijens (1) showed that the compressible Leonov model gives a reasonable description of flow-induced orientation during injection moulding of (amorphous) polymers. This model is fully determined with the linear viscoelastic spectrum, i.e. the moduli and relaxation times. We will use this model to describe the viscoelastic stresses in the molten phase of semi-crystalline polymers. Despite, other models like, for example the Giesekus model, the Phan-Thien Tanner model, the recently proposed FETA models (Peters (68)) or (modified) POM-POM models (Verbeeten (84)), could easily be implemented. For sake of simplicity only, here the compressed Leonov model is explored to some extent.

In any loaded state materials are deformed. Deformation can be multiplicatively decomposed into an elastic recoverable (\mathbf{F}_e) and a plastic (\mathbf{F}_p) part. Consequently, in the compressible Leonov model the deformation gradient tensor \mathbf{F} is split in an elastic part \mathbf{F}_e and a plastic part \mathbf{F}_p (fig. 2.1)

$$\mathbf{F} = \left(\bar{\mathbf{v}}_0 \bar{\mathbf{x}} \right)^c = \mathbf{F}_e \cdot \mathbf{F}_p \quad (2.11)$$

in which $\bar{\mathbf{x}}$ is the position vector. Volumetric effects in \mathbf{F}_e are separated from deviatoric effects by defining (fig. 2.1)

$$\bar{\mathbf{F}}_e = J^{-\frac{1}{3}} \cdot \mathbf{F}_e \quad (2.12)$$

$$\bar{J}_e = \det(\bar{\mathbf{F}}_e) = 1 \quad (2.13)$$

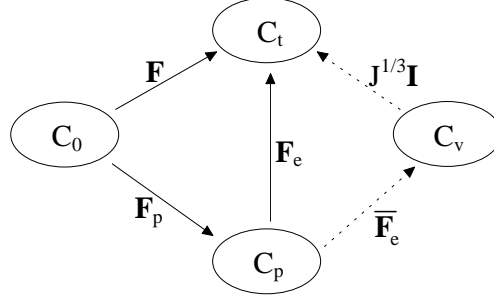


Fig. 2.1: The kinematic decomposition of the deformation tensor \mathbf{F} .

For the material time derivative of the volume invariant elastic Finger tensor $\bar{\mathbf{B}}_e = \bar{\mathbf{F}}_e \cdot \bar{\mathbf{F}}_e^c$ we obtain

$$\dot{\bar{\mathbf{B}}}_e = \left(\mathbf{L}_e - \frac{1}{3} \text{tr}(\mathbf{D}) \mathbf{I} \right) \cdot \bar{\mathbf{B}}_e + \bar{\mathbf{B}}_e \cdot \left(\mathbf{L}_e^c - \frac{1}{3} \text{tr}(\mathbf{D}) \mathbf{I} \right) \quad (2.14)$$

in which $\mathbf{L}_e = \dot{\bar{\mathbf{F}}}_e \bar{\mathbf{F}}_e^{-1}$ is the elastic part of the velocity gradient tensor, \mathbf{D} the rate of deformation tensor and \mathbf{I} the unit tensor. Leonov fixes the intermediate state by assuming no rotation, i.e. $\mathbf{W}_p = 0$; rearrangement of (2.14) results in

$$\dot{\bar{\mathbf{B}}}_e = \left(\mathbf{L}^d - \mathbf{D}_p \right) \cdot \bar{\mathbf{B}}_e + \bar{\mathbf{B}}_e \cdot \left(\mathbf{L}^{dc} - \mathbf{D}_p \right) \quad (2.15)$$

For the plastic part of the rate of deformation tensor \mathbf{D}_p , Leonov (56; 57) proposed the following constitutive expression:

$$\mathbf{D}_p = \frac{1}{4\theta} \left(\bar{\mathbf{B}}_e^d - \bar{\mathbf{B}}_e^{-d} \right) \quad (2.16)$$

Using this in (2.15) results in

$$\dot{\bar{\mathbf{B}}}_e = \mathbf{L}^d \cdot \bar{\mathbf{B}}_e + \bar{\mathbf{B}}_e \cdot \mathbf{L}^{dc} - \frac{1}{2\theta} \left(\bar{\mathbf{B}}_e \cdot \bar{\mathbf{B}}_e - \mathbf{I} - \frac{1}{3} \left(\text{tr}(\bar{\mathbf{B}}_e) - \text{tr}(\bar{\mathbf{B}}_e^{-1}) \right) \bar{\mathbf{B}}_e \right) \quad (2.17)$$

Elastic stresses are decomposed in a hydrostatic part and the extra stress tensor $\boldsymbol{\tau}_e$ (the deviatoric part):

$$\boldsymbol{\sigma}_e = p \mathbf{I} + \boldsymbol{\tau}_e \quad (2.18)$$

For the multi-mode case, the extra stress tensor can be written as

$$\boldsymbol{\tau}_e = \sum_{j=1}^n G_j \bar{\mathbf{B}}_{ej}^d \quad (2.19)$$

in which G_j the modulus for the j -th mode, and using n different $\bar{\mathbf{B}}_{ej}^d$. With every $\bar{\mathbf{B}}_{ej}^d$, different plastic rate of deformation tensors \mathbf{D}_p can be defined. Notice that by choosing the

appropriate expression for \mathbf{D}_p , rather than the specific choice of Leonov (eqn. 2.16), most of all known viscoelastic models can be regained or new viscoelastic models can be obtained (Peters (68)). The extra stress tensor can also be modeled in terms of the configuration statistics of the molecules. When the polymer chains are considered as Hookean springs, the viscoelastic stress for a mono-disperse material is given by (Larson (53))

$$\boldsymbol{\sigma}_e = 2\nu kT\beta^2 \langle \vec{R}\vec{R} \rangle \quad , \quad \beta^2 = \frac{3}{2\langle \vec{R}\cdot\vec{R} \rangle_0} \quad (2.20)$$

where $\langle \cdot \rangle$ is an average over the non-equilibrium distribution function Ψ of the chain end-to-end vector \vec{R} . When comparing this result with the phenomenological Leonov model, it is concluded that the deviatoric part of the configuration tensor $\langle \vec{R}\vec{R} \rangle^d$ plays the same role as the deviatoric part of the elastic Finger tensor \mathbf{B}_e^d . We, therefore, assume that the elastic Finger tensor is a representative measure for the molecular configuration in the molten phase. For a multi mode model the highest relaxation time will correlate most strongly with the high-end tail of the molecular weight distribution.

2.2 Modeling injection moulding

Because in most applications the thickness of an injection moulded product is small compared to the other dimensions, any cavity can be described by using a Hele-Shaw or thin film approximation (Douven (14), Hieber (33) and Tucker III (82)). The main assumptions made are:

- (i) inertial and body forces are negligible compared to the viscous forces,
- (ii) pressure is constant across the thickness, the velocity component in the thickness-direction is small compared to those tangent to the mid-plane,
- (iii) velocity gradients parallel to the mid-plane are small compared to those in the thickness-direction,
- (iv) thermal conductivity parallel to the mid-plane is negligible compared to the conduction in the thickness direction.

In this approach, the pressure only has to be calculated in the mid-plane of the cavity (2D), while the velocity and temperature have to be calculated fully 3D. Using these assumptions, the balance equations can be simplified to (following Caspers (9)):

$$\vec{\nabla}^* \cdot \vec{v}^* + \frac{\partial v_3^\epsilon}{\partial x_3^\epsilon} = -\frac{\dot{\rho}}{\rho} \quad (2.21)$$

$$\vec{\nabla}^* p = \frac{\partial}{\partial x_3^\epsilon} \left(\eta \frac{\partial \vec{v}^*}{\partial x_3^\epsilon} \right) \quad , \quad \frac{\partial p}{\partial x_3^\epsilon} = 0 \quad (2.22)$$

$$\rho c_p \dot{T} = \frac{\partial}{\partial x_3^\epsilon} \left(\lambda \frac{\partial T}{\partial x_3^\epsilon} \right) + \eta \dot{\gamma}^2 - \frac{T}{\rho} \left(\frac{\partial \rho}{\partial T} \right)_p \dot{p} + \rho H \dot{\xi} \quad , \quad \dot{\gamma} = \left| \frac{\partial \vec{v}^*}{\partial x_3^\epsilon} \right| \quad (2.23)$$

in which \vec{v}^* indicates the velocity parallel to the mid-plane of the cavity, x_3^ϵ the local thickness coordinate, H the heat of crystallization, and $\dot{\xi}$ the rate of the degree of crystallinity. In the flow front region, these simplifications obviously cannot be applied since the velocity in the thickness direction is not negligible there. Following Caspers (9), the area influenced by the

flow front is assumed to be small. Given the entrance position of the material particle in the flow front region, together with the mass balance, the exit position is calculated using the local velocity profile. Elongational flow is neglected, which may lead to errors in the flow-induced stresses close to the mould wall, while the residence time of the material in the flow front region is assumed to be zero, and the flow is assumed to be isothermal at the flow front. The material, which ends up at the mould wall from the center of the mould is cooled at a high rate to the mould wall temperature. The thermal capacity c_p , the thermal conductivity λ and the heat of crystallization H are assumed to be constant. The numerical aspects concerning the finite element method, used to obtain approximate solutions for the governing equations, can be found in Caspers (9). As stated, in order to calculate the flow-induced recoverable strain- and orientation, a decoupled modeling is used. Non-isothermal generalized Newtonian flow modeling gives the kinematics which are used in the fully 3D viscoelastic calculation (Caspers (9), Douven (14)) to compute stresses. Both a 4th order Runge-Kutta explicit integration scheme and a modified streamline upwind Petrov Galerkin Eulerian implicit integration scheme can be used in the solution for the recoverable strain and orientation. All calculations can easily be extended to fully 3D (Haagh (30)), dropping almost all of the assumptions and restrictions mentioned above.

2.3 Crystallinity

If crystalline structures are present, they will influence different material properties, like the specific volume and viscosity (see subsections 2.3.1 and 2.3.2). The constitutive equation for the specific volume will be discussed in detail in chapter 4. The thermal capacity c_p and the thermal conductivity λ are assumed to be unaffected by the crystalline structure. Dependent on the degree of space filling, the material will show a transition from fluid to solid behavior, which is, to some extent, addressed below.

2.3.1 Viscosity

Different models for the viscosity can be used in VIp, like a power law model, the Carreau model or the multi-mode Leonov model (Caspers (9)). Since the influence of the crystalline structure is not clear yet (see subsection 1.1.4), it is assumed that the crystals form a separate phase in the amorphous melt, and change the viscosity like is known from the most elementary ideas from dispersion rheology (Ito (36)):

$$\eta_\xi = \eta e^{2.5\xi_g} \quad (2.24)$$

in which η_ξ is the viscosity influenced by the crystalline structure, η the viscosity of the fully amorphous melt and ξ_g the local degree of space filling, calculated from yet to be specified models for the crystallization kinetics (see chapter 3).

2.3.2 Solid layer position

For injection moulding simulations using amorphous polymers, the position of the solidified layer is determined by the temperature; the front of the solid layer has a temperature equal to the glass transition temperature of the polymer involved or is determined via any other,

more realistic, no-flow condition (e.g. Caspers (9)). For semi-crystalline polymers this issue is somewhat more complicated, since both a solidified front or a zone containing solid and amorphous polymer will be present dependent on the cooling rate applied. This problem has been dealt with in an empirical manner by Guo et al. (27), who assumed that the melt loses its fluidity upon the occurrence of crystallization, i.e. a step-like change in the viscosity. Verhoyen (85) defined the position of the solid layer, as the position where the viscosity reaches a limit value of $\eta = 1 \cdot 10^6 [Pa.s]$. The viscosity, in its turn, has been related to the degree of crystallinity by assuming the crystals to form a separate phase in the amorphous melt. To take care of this effect in VIP, the viscosity of the melt is assumed to be dependent on the degree of space filling, while the polymer is assumed to be solidified, if the degree of space filling $\xi_g \geq 0.99[-]$. Although we only calculate the appearance of the α -phase structures, at high cooling rates these structures will be present in a (solid) mesomorphic matrix. For the very high cooling rates at the mould wall, the material will thus be quenched and the degree of space filling (with α -phase) will not reach $\xi_g = 0.99[-]$ there. Somewhere across the thickness of the mould it will, while in between this position and the mould wall, the polymer will most likely be present in the mesomorphic phase.

In fig. 2.2 (upper part), an example of the distribution of the degree of space filling ξ_g over the thickness of the mould is shown. With increasing time (arrow direction), at a position

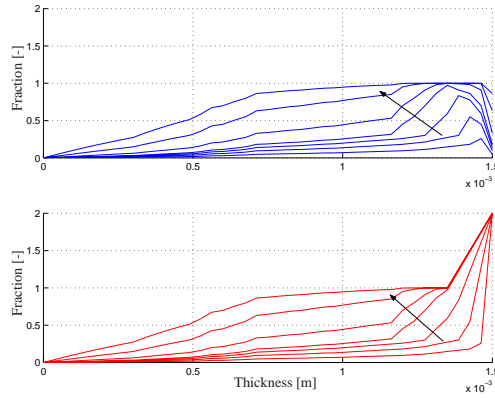


Fig. 2.2: Example of the distribution of the degree of space filling from the center of the mould to the mould wall with increasing time (arrow direction). The upper part shows the calculated distribution, while the lower part shows the modified distribution.

in the polymer melt, the value $\xi_g = 0.99[-]$ is reached. If only the α -phase structures are considered, the position of the solidified layer will change from the mould wall to a position in the polymer. The discontinuity encountered in this change (fig. 2.3, upper part) will cause numerical instabilities in the solution of the velocity, decreasing the accuracy of the calculation. To solve this, an ad hoc solution for the influence of the mesomorphic phase on the solid layer position is used. The value for the degree of space filling at the mould wall is temporary set to $\xi_g = 2[-]$, while an interpolation is performed from this wall value

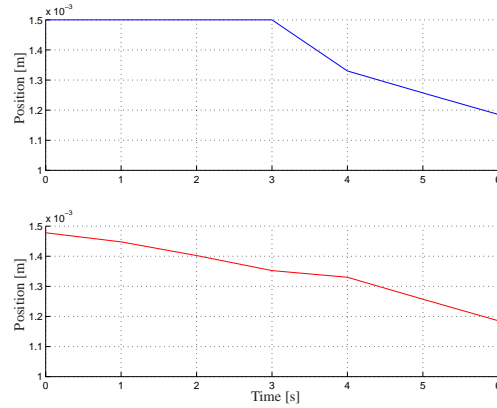


Fig. 2.3: Example of the position of the interface between the fully solidified polymer and the polymer melt. The mould wall is located at a position of $1.5 \cdot 10^{-3}$, while the center is located at a position of $0.0 \cdot 10^{-3}$. The upper part shows the position determined from fig. 2.2, upper part, while the lower part shows the position determined from fig. 2.2, lower part.

to the maximum in the distribution of the degree of space filling (fig. 2.2, lower part). With increasing time (arrow direction), the position of the interface will smoothly vary from the mould wall to the peak value. As soon as the maximum in the degree of space filling reaches a value $\xi_g = 0.99[-]$, the original position (fig. 2.3, upper part), will match the modified position (fig. 2.3, lower part). As a result, the calculation will stay numerically stable.

2.4 Conclusion

To the framework used to study moulding processes (governing equations), equations to predict (flow-induced) recoverable strain and orientation are added. Although the compressible Leonov model is used, other models could easily be implemented. This framework is used to study the injection moulding process, for which different assumptions simplify the governing equations. Choices for the influence of the crystal structure on material properties are made. Now this part of the modeling is set, we can focus on flow-induced crystallization in chapter 3 and density measurements and modeling in chapter 4, which complete the modeling.

Chapter 3

*Development of a strain based model for flow-induced crystallization*¹

In contrast to the development of the spherulitical structure, which can be described accurately by e.g. Schneider's rate equations (74), the description of the development of the flow-induced crystalline structure is a topic that only relatively recently received attention. Different models have been proposed, some based on strain (Ito (37)), Cauchy stress (Verhoyen (85)), the conformation of the molecules (Bushman (8), Doufas (12)) or iso-kinetic models (Nakamura (66)). A Nakamura model (66) is used by Isayev (35) and Guo (29), combined with a phenomenological approach to model molecular deformation. The most common shortcomings of these models are:

- (i) except for the degree of crystallinity they do not provide any further information concerning the final crystalline structure ((8),(12), (29), (35), (37), (66)),
- (ii) they can not describe processes in which a reverse flow occurs during solidification / crystallization of the polymer ((37), (85)).

A striking example of the last process can be found in 'push-pull' moulding, notably the SCORIM process (46) where, after the mould has been filled, the flow is kept in motion backwards and forwards. For example in Doufas' model (12), which is based on the Hamiltonian Poisson Bracket formalism combined with the Avrami equation (12), the resulting set of equations describe a conformation tensor, an orientation tensor and the degree of crystallinity, but no description is available of the final structure (size of structures, etc.). For models that incorporated the Nakamura model for crystallinity (35) the same problem arises. Moreover, with Nakamura's iso-kinetic approach (66), where it is assumed that the kinetics of nucleation and growth should show the same temperature dependence, any influence of the thermal history on the texture is erased per definition (39). In Ito's and Verhoyen's work, the number of nuclei depends on the amount of strain, or viscous stress, respectively. This implies that the number of nuclei would vary, or even could go to zero, when the total amount of strain during the backward flow equals that of the forward flow in the SCORIM process. However, as is clear from experiments, such a flow history still results in shear induced layers. The shear rate dependent phenomenological model of Eder (18) has the advantage that it predicts structure properties such as the number of shish-kebabs, their length, etc. This model gives a reasonably good description of the phenomena as observed during experiments (43). However, it is based on the kinematics of the flow, not on the dynamics of the molecules in the melt. This leads to the idea that, although the structure of the Eder model is useful and should be remained, another driving force should be used in the model. For instance,

¹ This chapter is reproduced in part from Zuidema et al. (94)

can the nucleation rate be made dependent on the recoverable strain (which is equivalent to the viscoelastic stress), which is considered to be a representative measure for the molecular orientation and strain. Experimental evidence is found by McHugh (64) who concluded that one or another type of viscoelastic molecular strain, due to flow-orientation, may be the controlling process rather than the thermodynamic nucleation-controlled growth often used to describe flow-induced crystallization. Moreover, the results from Kumaraswamy (51) suggest that the critical shear rate in the model of Eder (18) might be related to the rheological relaxation time of the melt.

3.1 Crystallization kinetics equations

Dependent on the mechanical history of the melt, different crystalline structures, like spherulitical and shish-kebab, will be present in the final material (see subsection 1.1.2). The contributions of both types of crystals should be combined to give the total degree of crystallinity. For the spherulitical structures Schneider's rate equations (74) are used. They fully characterize the resulting structure, i.e. mean number of spherulites, their radius, surface and volume. A simple series of nested differential equations results:

$$\begin{aligned}
 \dot{\phi}_3 &= 8\pi\alpha & (\phi_3 &= 8\pi N) \\
 \dot{\phi}_2 &= G\phi_3 & (\phi_2 &= 4\pi R_{tot}) \\
 \dot{\phi}_1 &= G\phi_2 & (\phi_1 &= S_{tot}) \\
 \dot{\phi}_0 &= G\phi_1 & (\phi_0 &= V_{tot})
 \end{aligned} \tag{3.1}$$

in which ϕ_0 is the undisturbed total volume V_{tot} of the spherulites per unit of volume, ϕ_1 is the total surface S_{tot} of the spherulites per unit of volume, ϕ_2 is 4π times the sum of the radii R_{tot} of the spherulites per unit of volume, ϕ_3 is 8π times the number of the spherulites N per unit of volume (if impingement and swallowing are disregarded, meaning that the nucleation rate does not depend on the volume fraction of already crystallized material), α is the nucleation rate, G is the crystal growth rate and the 'dot' denotes the time derivative. The crystal growth rate G and the nucleation rate α have to be measured as a function of temperature. These so called rate equations are based on the generalized Kolmogoroff equation (Janeschitz-Kriegl (39)), in which the nucleation is random in time and spatially uniform. Schneider's rate equations can be combined with one of the models for spherulitical impingement as, for example, the Avrami model

$$-\ln(1 - \xi_g) = \phi_0 \tag{3.2}$$

or the Tobin model

$$\frac{\xi_g}{1 - \xi_g} = \phi_0 \tag{3.3}$$

in which ξ_g is the degree of space filling. The degree of crystallinity ξ can be obtained by multiplying the degree of space filling with the degree of crystallinity in each spherulite. The crystallization enthalpy is taken into account in the energy equation (2.1) through the source term r_h .

Simultaneous with (and independent from) the process of spherulitical nucleation and crystal growth, flow-induced nucleation and crystallization processes take place during flow. It is assumed by Eder (18; 20), that the influence of the deformation on this type of crystallization is due to the formation of thread-like nuclei (shish) on which lamellae grow mainly perpendicular (kebabs). The development of this contribution is described using Eder's rate equations for shear induced crystallization, which include different aspects of the flow-induced structure (59). Each shish-kebab is represented by a cylindrical volume:

$$\begin{aligned}\dot{\psi}_3 + \frac{\psi_3}{\tau_n} &= 8\pi \left(\frac{\dot{\gamma}}{\dot{\gamma}_n}\right)^2 g_n & (\psi_3 &= 8\pi N_f) \\ \dot{\psi}_2 + \frac{\psi_2}{\tau_l} &= \psi_3 \left(\frac{\dot{\gamma}}{\dot{\gamma}_l}\right)^2 g_l & (\psi_2 &= 4\pi L_{tot}) \\ \dot{\psi}_1 &= G\psi_2 & (\psi_1 &= S_{tot}) \\ \dot{\psi}_0 &= G\psi_1 & (\psi_0 &= V_{tot})\end{aligned}\tag{3.4}$$

$$-\ln(1 - \xi_g) = \psi_0$$

in which ξ_g is the degree of space filling, ψ_0 the undisturbed total volume V_{tot} of the shish-kebabs per unit of volume, i.e. impingement and swallowing are disregarded, ψ_1 the total surface S_{tot} of the shish-kebabs per unit of volume, ψ_2 is 4π times the total length L_{tot} of the shish per unit of volume, ψ_3 is 8π times the number of flow-induced nuclei N_f per unit of volume, τ_l the temperature and shish length dependent relaxation time for the shish during axial growth, $\dot{\gamma}_l$ a typical value for the shear rate for the extension of the shish, g_l a parameter for the axial shish growth, τ_n the temperature dependent relaxation time for the nuclei formation, $\dot{\gamma}_n$ a typical value for the shear rate for the nuclei-growth and g_n a parameter for the nucleation rate. As a first step, spot-like nuclei are formed sporadically with a frequency proportional to the square of the shear rate. It is assumed that the spot-like nuclei grow out into shish during further shearing. According to Liedauer (59) one can assume that, upon cooling, the nuclei can no longer disappear as soon as shish have grown out of them, which results in an infinite relaxation time τ_n once a nucleus starts growing into a shish. Thickening of the shish is caused by lamellar crystal growth by the remaining polymer molecules like in spherulitical growth. In this way the model represents the shish-kebab structure as found in highly deformed regions. However, in this model the orientation is not captured.

Since both the spherulitical and the flow-induced structures contribute to the degree of space filling, they can easily be combined using the models for impingement:

$$-\ln(1 - \xi_g) = \phi_0 + \psi_0 \quad \frac{\xi_g}{1 - \xi_g} = \phi_0 + \psi_0\tag{3.5}$$

3.2 Experimental results

When using experiments for the development of models for flow-induced crystallization kinetics of semi-crystalline polymers, the influence of the thermal and deformation history should preferably be separated. Moreover, when processing conditions can be controlled, like e.g. in the SCORIM process, the resulting crystal structure can be related to the influence of the known deformation history using numerical simulations. As nucleation/crystallization is enhanced by deformation, and the deformation varies over the thickness for a flow in a duct, the degree and type of crystallinity (shish-kebabs) in the highly strained regions at the cavity walls, differs from the spherulitical core. This results in a layered structure over the thickness of the duct, which' position and thickness depends on the thermal and mechanical history. These layers can be visualized by making microtome cuts and characterized using a polarization microscope (44). Results of three types of crystallization experiments are used; a quiescent, a startup flow and a steady state flow experiment.

3.2.1 Quiescent experiments

During crystallization of a melt in a quiescent state, the crystallization process can be kept up with by measuring the temperature distribution over the thickness of the sample. Malkin (63) quenched a polyamide 6 plate of 20 [mm] from 478 [K] to 453 [K] (see appendix A.1). This results in a temperature development as shown in fig. 3.1. As is clear, the heat of crystal-

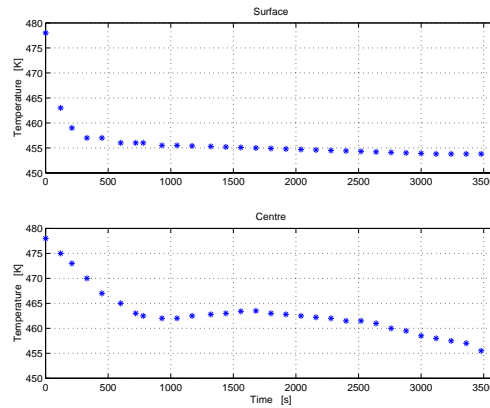


Fig. 3.1: Measured temperatures at the surface of a Polyamide 6 plate of 20[mm] (top) and at the center (bottom). After (63).

lization results in a provisional increase of the temperature in the center of the plate. Schneider (73) used these measurements to test his rate equations. The surface temperature was used as a boundary condition, and the temperature and the degree of crystallinity at the center of the sample were calculated together with the degree of crystallinity at the surface. By using the same procedure, our VIp predictions of the temperature history in the center and the degree of crystallinity both at the surface and at the center of the plate, will be compared

with the experimental data and predictions by Schneider, respectively.

3.2.2 Short term shear experiments

In experiments done by Jerschow (43), a duct ($155 \times 10 \times 1$ [mm^3]) is filled with an isotactic polypropylene at $473[K]$ (see appendix A.2). The duct is equipped with two windows placed in opposite positions near the end of the gate in the large duct walls to enable optical observations of the material passing the cross-section. After filling, the flow is stopped and a waiting period of 20 minutes is applied to get rid of filling history. Subsequently, the duct is quenched to the desired experimental temperature ($423[K]$). Next the flow in the duct is started again for a chosen time. In this way experiments can be done for different shearing times t_s and wall shear rates $\dot{\gamma}_w$. Shearing times at this temperature are such that during flow, when the material experiences deformation, no crystallization can be observed. After this shearing procedure, which lasts up to 30 seconds, the light intensities at perpendicular and parallel polars are monitored for a time period of 30 to 90 minutes. Finally, the duct is cooled to room temperature. More detailed information can be found in (18), (20) and (43). For experiments using different shearing times and shear rates, the thickness of the flow-induced layers can be obtained by making microtome cuts across the thickness parallel to the flow direction. Viewing these cuts under a microscope, using polarized light, clearly shows three different layers across the thickness if the shear flow is strong enough (fig. 1.1); a highly oriented layer near the walls of the duct, a core with large spherulites and a fine grained layer in between. Measuring the thickness of these layers resulted in a relation between the shearing time applied and the corresponding, calculated shear rates at the boundaries of these layers (fig. 3.2). Notice that for isothermal duct flow the shear rate can be calculated quite accu-

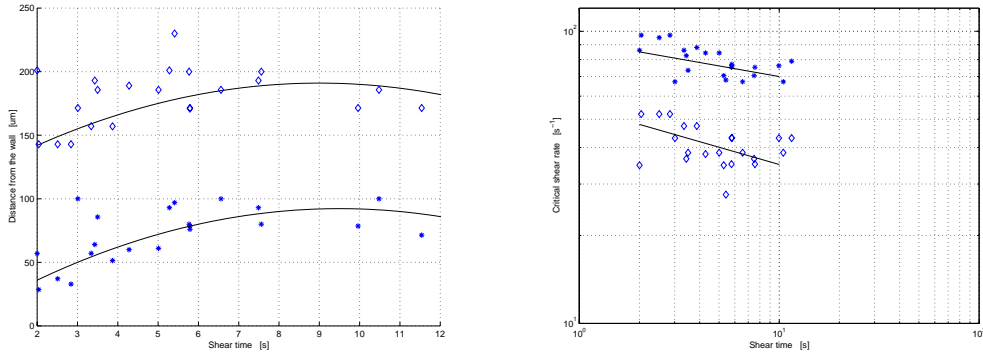


Fig. 3.2: Measured distance from the wall of the boundaries of the flow-induced (*) and fine grained (◇) layers (left) and accompanying shear rate at these positions (right) as a function of shear time, for a wall shear rate of $115 [s^{-1}]$. After (43).

rately when the viscosity curve is known, using for example a Carreau-Yasuda model. From his experiments, Jerschow (43) concluded that for shear induced crystallization, precursors are formed during the flow, which reach the same effectiveness at $\dot{\gamma}^4 t_s^2 = constant$. He also concluded that the boundary between the fine grained layer and the core is characterized

by $\dot{\gamma}_c^2 t_s = \text{constant}$, in which $\dot{\gamma}_c$ is the critical shear rate at the boundary. Similarly it was concluded that the boundary between the fine grained layer and the highly oriented layer is characterized by $\dot{\gamma}_c^4 t_s = \text{constant}$. Finally, based on the results of these measurements, a shear-induced crystallization model was formulated by Eder (18), which was discussed in section 3.1.

3.2.3 Steady state experiments

Another type of flow experiment is described by Eder (20). A steady state flow is generated in a duct of rectangular cross section ($110 \times 10 \times 1 \text{ [mm}^3\text{]}$) using an isotactic polypropylene (see appendix A.2). The temperature is selected such that when the material has passed the duct, no crystallization can be observed. When steady state flow conditions are reached, the duct is quenched immediately after cessation of steady flow. Microtome cuts are made across the thickness parallel to the flow direction to determine the position of the interface between the highly oriented layer near the walls of the duct and the fine grained layer next to it as a function of the distance from the duct entrance. For different flow rates at a temperature of 473[K] the results are shown in fig. 3.3. At these positions, the calculated shear rate supports

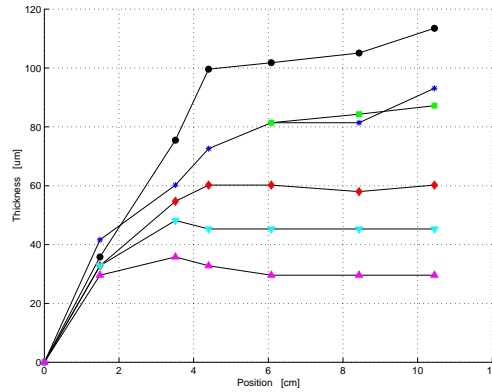


Fig. 3.3: Boundary layer thickness vs distance from the entrance to the duct, as obtained by a quench applied immediately after cessation of steady flow at a temperature of 473[K] for different flow rates (● : $11.26 \cdot 10^{-7}[\text{m}^3\text{s}^{-1}]$, * : $9.940 \cdot 10^{-7}[\text{m}^3\text{s}^{-1}]$, ■ : $7.898 \cdot 10^{-7}[\text{m}^3\text{s}^{-1}]$, ◆ : $5.724 \cdot 10^{-7}[\text{m}^3\text{s}^{-1}]$, ▽ : $4.439 \cdot 10^{-7}[\text{m}^3\text{s}^{-1}]$, △ : $3.352 \cdot 10^{-7}[\text{m}^3\text{s}^{-1}]$). After (20).

the formulated shear-induced crystallization model by Eder (18).

3.3 Modeling results

3.3.1 Quiescent experiments

To test the implementation of the modeling for quiescent crystallization in our code VIp, the experimental results described in the previous section are used. Predictions on both the temperature and the degree of crystallinity from the center to the surface are obtained. In fig. 3.4

the results for Schneider's rate equations using Avramis (left) and Tobins (right) model of impingement are shown (solid lines: surface and center predictions; dashed lines: predictions at positions in between), together with the temperature measurements by Malkin (circles) and Schneider's resulting predictions on the degree of crystallinity (squares). The agreement

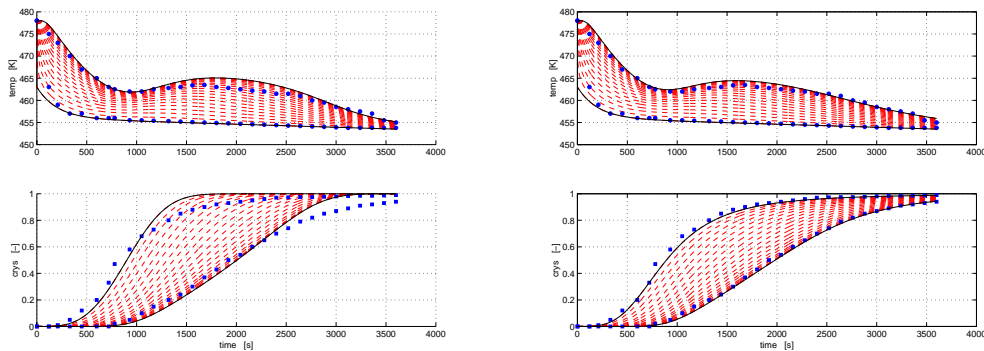


Fig. 3.4: The results for Schneider's rate equations using Avramis (left) and Tobins (right) model of impingement. The lines are simulation results using *Vip*, circles are temperature measurements and squares are Schneider's resulting predictions on the degree of crystallinity.

is good for the Avrami model and excellent for the Tobin model, indicating that Schneider obviously used the latter. While the Schneider rate equations do not only describe the resulting degree of crystallinity, but also give a full description of the average properties of the resulting structure, it is possible to reproduce the structure development during crystallization by generating (at random) nuclei with an average rate equal to the local nucleation rate. For different times during crystallization, the distribution of the structure over the thickness of the sample is shown (fig. 3.5), where the upper parts show the spherulitical structure (i.e. similar to photographs of microtome cuts using a microscope). The lower parts give the local degree of crystallinity (solid), calculated by counting pixels in the upper part, together with the global average degree of crystallinity, calculated using Schneider's rate equations (line).

3.3.2 Short term shear experiments: structure correlation with viscoelastic properties

Solving the balance equations combined with the Schneider rate equations for spherulitical crystallization, the model for flow-induced nucleation and crystallization as proposed by Eder et al. (20) can be used to reproduce the full thermo-mechanical and structural history of these experiments numerically. With the viscoelastic Leonov model for the orientation and the rheological data of the material, also the evolution of the state of the orientation of the molecules can be determined. The basic idea that is applied here, is to correlate the predicted viscoelastic state with the predicted flow-induced structure and, in this way, check concepts on flow-induced nucleation/crystallization which are based on previous observations (Vleeshouwers (87), Tas (80)). In (87) it was observed that the high-end tail of the molecular weight distribution was the main factor in enhancing the crystallization process. However, no underlying mechanism was proposed. In (80) it was observed that, during film blowing of

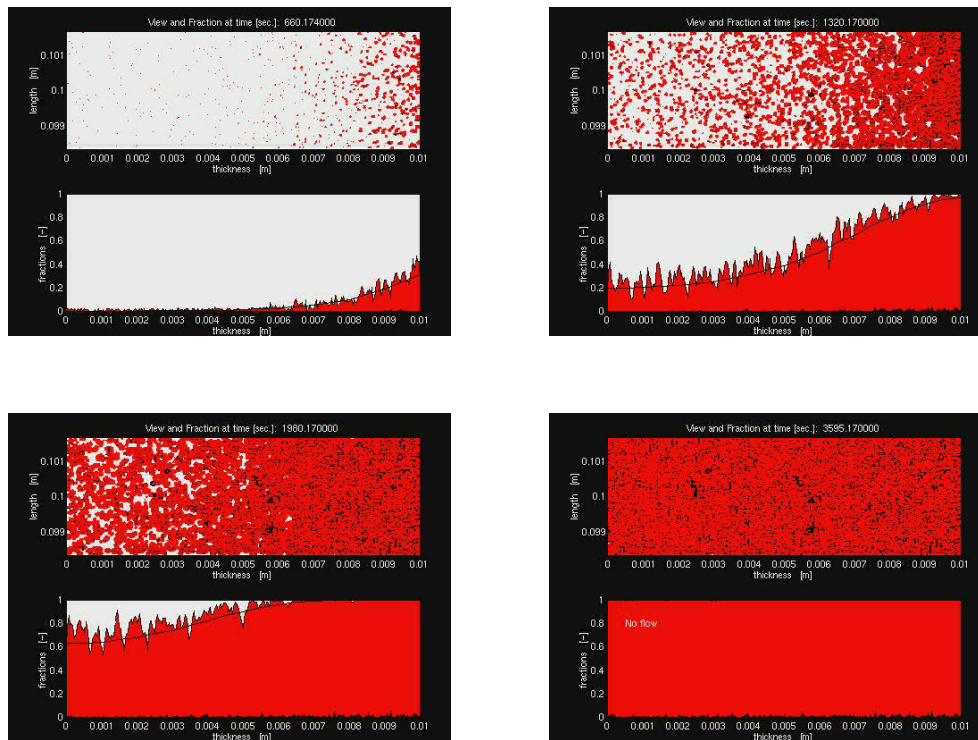


Fig. 3.5: Reproduction of the structure from the center of the plate (thickness = 0 [m]) to the surface (thickness = 0.01 [m]) for different moments during crystallization (upper parts), together with an impression of the local and global degree of crystallinity (lower parts).

LDPE films, the viscoelastic stresses at the freeze line, determine the morphology, and the resulting mechanical properties of blown films made of LDPE

The basic concept that is used here is the following. Flow gradients will induce a more ordered molecular state, lowering the entropy, due to orientation. This will apply to a greater extend to the high molecular weight molecules given their larger relaxation times. This more ordered state will facilitate nucleation/crystallization or, in other words, increase the probability that fluctuations lead to nucleation. (For too strong flow gradients there is experimental evidence (Blundell (6)) that nucleation/crystallization is hampered because molecules are too far from the equilibrium state). Although a spectrum of relaxation times obtained from rheological measurements (oscillatory simple shear providing G' and G'') is very often limited and probably does not show the full range of relaxation times for a given polymer melt, it seems reasonable to expect that the highest measured relaxation time will correlate most strongly with the high-end tail of the molecular weight distribution. We, therefore, postulate that the flow induced structure will correlate most strongly with the viscoelastic mode with the highest relaxation time. Moreover, as flow gradients will not only induce (extra) nucle-

ation and crystallization but also introduce orientation, it is postulated that the high relaxation mode will predict the orientation of the flow-induced structures. The molecules corresponding to the high molecular weight tail will constitute the backbone/precursor of the shish.

This can be summarized in a formal way by stating that the number of flow-induced nuclei and/or the growth rate of these flow induced structures is a functional of the invariants of the conformation tensor corresponding to the highest relaxation time (or invariants of the corresponding elastic Finger tensor; as was discussed in the modeling chapter (2), the conformation tensor is replaced by the elastic Finger tensor). If this statement is true, then material which experienced a history leading to the same value of this (unknown) functional should show the same flow-induced structure. We will choose those positions in a sample which are clearly visible, i.e. the transitions between the highly oriented and the fine grained layer and between the fine grained layer and the common spherulitical core.

First we will check whether the proposed correlations are valid. Based on some preliminary work, where a correlation was sought with the first normal stress difference (Zuidema (93)), the following is restricted to the second invariant of the deviatoric part of the volume invariant elastic Finger tensor

$$J_2(\overline{\mathbf{B}}_e^d) = \frac{1}{2} \overline{\mathbf{B}}_e^d : \overline{\mathbf{B}}_e^d \quad (3.6)$$

For simple shear flows, where all experiments discussed here belong to, this second invariant scales with the square of the first normal stress difference for large deformations. Notice that this does not give the sought functional; it only indicates how it might look ². Experiments from Jerschow (43) (section 3.2) with a wall shear rate of 79 and 115 [s^{-1}] were simulated. The experimentally determined distance from the wall of the boundaries of the flow-induced and fine grained layers are reproduced in fig. 3.6 for 79 [s^{-1}] and in fig. 3.2 (left) for 115 [s^{-1}]. Simulations have been done for experiments with different shearing times, including the relaxation period of the recoverable strain. The viscoelastic part of the calculation is stopped after the first mode value for the recoverable strain has reached a value smaller than approximately 0.5 % of the maximum values. Then, the most simple functional of $J_2(\overline{\mathbf{B}}_e^d)$ is chosen to correlate with the structure, i.e. the layer boundaries, namely the integral in time of $J_2(\overline{\mathbf{B}}_e^d)$. Results for this time integral of the second invariant as a function of shearing time and position in the cavity are presented in fig. 3.7 for the first three modes (counted starting with the highest relaxation time) out of the four modes used (table A.7). The highest (first) mode correlates most strongly with the high-end tail of the molecular weight distribution, while the second and third mode correlate most strongly with a part of the molecular weight distribution containing shorter molecules. The time integral of the second invariant is then compared with the experimentally determined position of the layer boundaries. From these results the values of this integral at the layer boundaries can easily be obtained (fig. 3.8). A striking feature in fig. 3.8 is that for both experiments with different

² It is interesting to see the equivalence of this tensor, and its second invariant, with the tensor order parameter as defined in the Onsager theory (53) for the transition from isotropic to nematic of non-dilute solutions of rod-like molecules. This order parameter is defined as the deviatoric part of the orientation configuration tensor $\mathbf{S} = \langle \bar{u}\bar{u} \rangle$. The maximum of the scalar order parameter S is, defined by $S^2 = \frac{3}{2} \mathbf{S} : \mathbf{S}$ (Larson (54)).

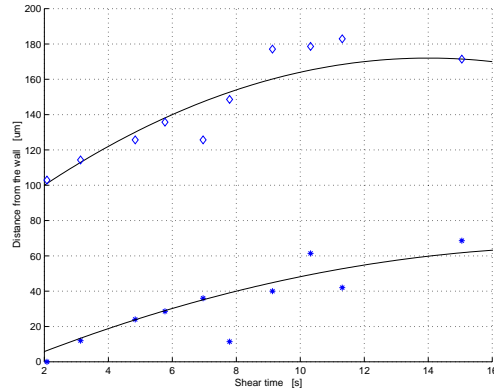


Fig. 3.6: Experimentally determined distance from the wall of the boundaries of the flow-induced (*) and fine grained layers (◊) for experiments with a wall shear rate of 79 (after (43)).

wall shear rates, the results do match for all modes. The most striking however, is that the values for the mode with the largest relaxation time are almost constant for the time integral of the second invariant $J_2(\overline{\mathbf{B}}_e^d)$ (fig. 3.8), which confirms the basic concept stated above that the flow induced structure will correlate most strongly with the viscoelastic mode with the highest relaxation time and, therefore, this is a good candidate for the driving force in a model for flow-induced crystallization.

3.3.3 Steady state experiments: validation

For the steady state experiments, section 3.2.3 (20), simulations were carried out giving the development of stresses until a steady state was present in the duct, including a spatially steady time integral of the second invariant of the recoverable strain tensor. Numerically, quenching was done by forcing the wall temperature to be $T_w = 293[K]$. For a number of experiments, all performed at $T = 473[K]$ and with different flow rates ($11.26 \cdot 10^{-7}$, $9.940 \cdot 10^{-7}$, $7.898 \cdot 10^{-7}$ and $5.724 \cdot 10^{-7} [m^3 s^{-1}]$) results are shown in fig. 3.9. For the low flow rates ($4.439 \cdot 10^{-7}$ and $3.352 \cdot 10^{-7} [m^3 s^{-1}]$) the determined distance from the wall of the interface is more an estimate than a measurement. Because of this inaccuracy, they are left out.

From the results of figure 3.9 it is clear that, also for a range of steady state experiments, the time integral of the second invariant of the recoverable strain tensor tends to a constant value at the layer boundaries, supporting the previously presented results and ideas. However, its value ($\approx 1 \cdot 10^5$) is smaller than the one obtained with the short term shear experiments ($\approx 2 \cdot 10^5$), compare fig. 3.8. This is most probably due to the (not modeled) influence of the flow in the extruder and the entrance region to the duct.

By using the Eder and Schneider rate equations, a complete description of the final structure is available. Since no data are present at $T = 473[K]$, it is assumed that the coefficients

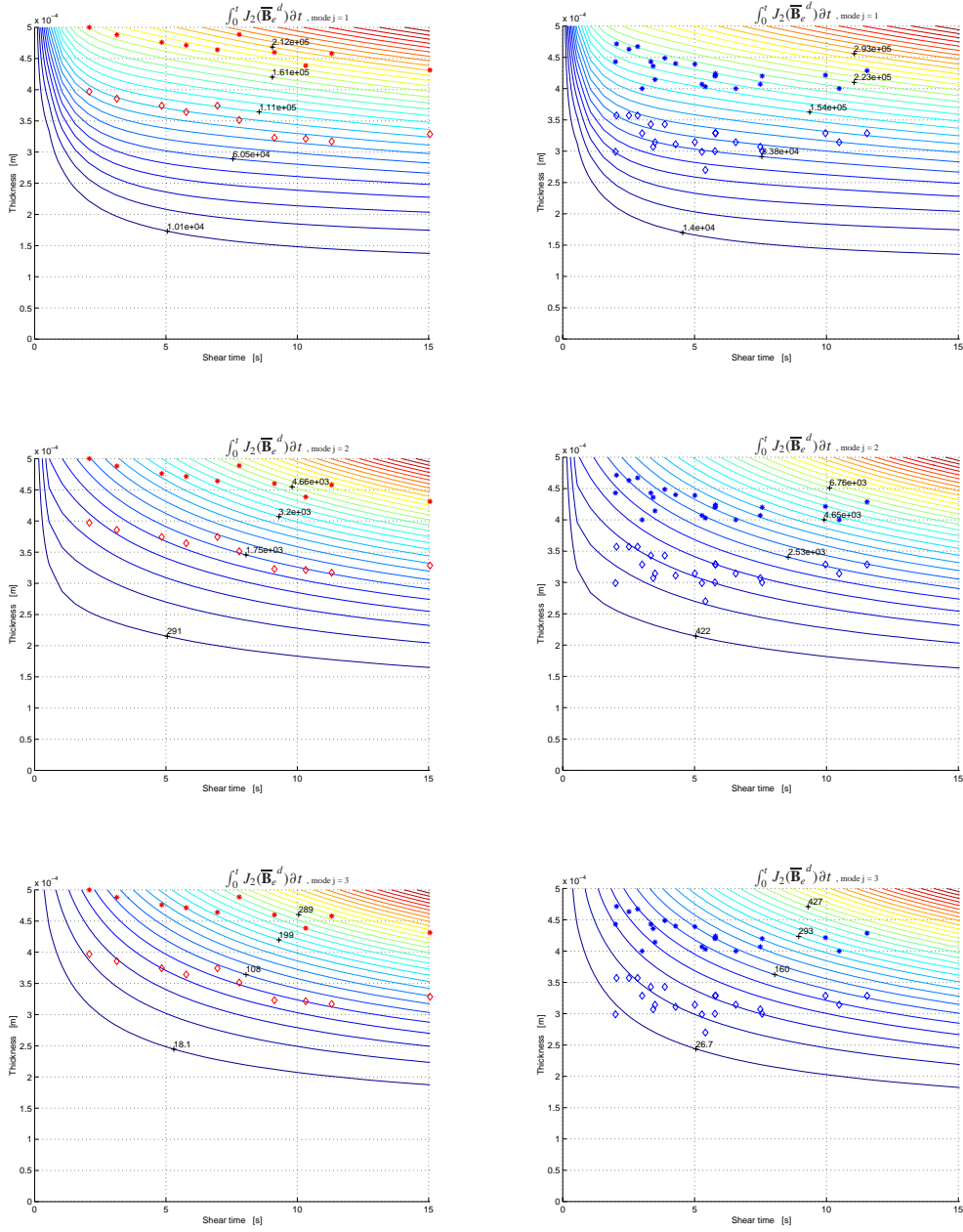


Fig. 3.7: Numerically determined contours for the time integral of the second invariant of the deviatoric part of the recoverable strain for experiments with a wall shear rate of 79 (left) and 115 $[s^{-1}]$ (right) together with the experimentally determined position of the boundaries of the flow-induced (*) and fine grained layer (◇). Results are for mode 1 (top), 2 (middle) and 3 (bottom). The center of the cavity is located at position zero.

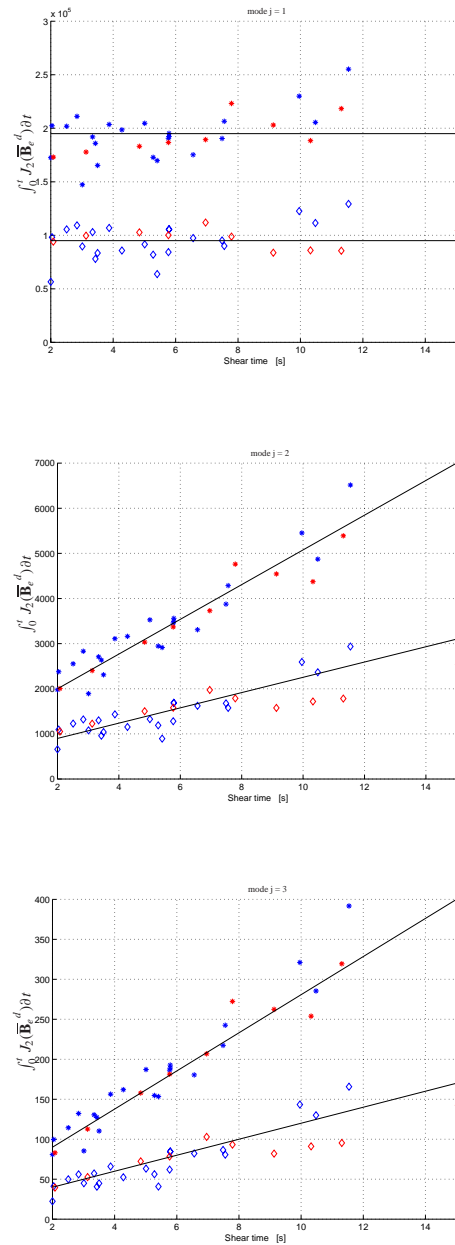


Fig. 3.8: Numerically obtained values for the time integral of the second invariant of the recoverable strain at the position of the boundaries of the flow-induced (*) and fine grained layer (◇) for experiments with a wall shear rate of 79 and 115 $[s^{-1}]$ Results are for mode 1 (top), 2 (middle) and 3 (bottom).

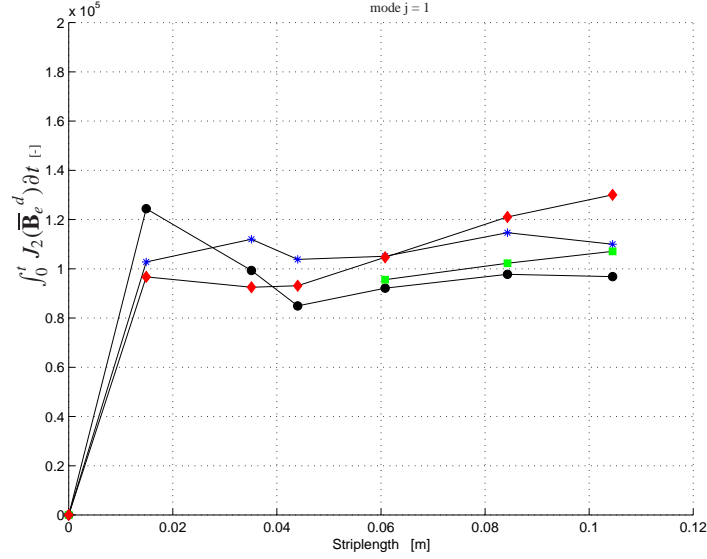


Fig. 3.9: Numerically obtained values for the time integral of the second invariant of the recoverable strain vs distance from the entrance to the duct, as obtained by a quench applied immediately after cessation of steady flow at a temperature of 473[K] for different flow rates (● : $11.26 \cdot 10^{-7} [\text{m}^3 \text{s}^{-1}]$, * : $9.940 \cdot 10^{-7} [\text{m}^3 \text{s}^{-1}]$, ■ : $7.898 \cdot 10^{-7} [\text{m}^3 \text{s}^{-1}]$, ◆ : $5.724 \cdot 10^{-7} [\text{m}^3 \text{s}^{-1}]$).

in the flow-induced crystallization equations 3.4 $\frac{g_n}{\dot{\gamma}_n^2} = 4.685 \cdot 10^{12}$ and $\frac{g_L}{\dot{\gamma}_L^2} = 2.690 \cdot 10^{-10}$ also hold at this temperature. They are used to visualize the development of the resulting structure during subsequent quenching of the steady state flow experiments for a cross section relatively close to the entrance (fig. 3.10, left) and one relatively close to the exit (fig. 3.10, right) of the duct (the quench started at 10 [s]). The upper parts show the spherulitical and shish-kebab structure (i.e. similar to photographs of microtome cuts using a microscope). The lower parts give again the local degree of crystallinity (solid), calculated by counting pixels in the upper part, together with the global average degree of crystallinity, calculated using the Schneider and Eder rate equations and summing up both contributions (line). When different crystals capture the same pixel by growth, this is registered as an interface indicating the amount of intermingled spherulites and shish-kebabs. The difference in layer thickness of the oriented structure over the length of the duct is clearly present in these representations of microtome cuts. Moreover, the slow cooling in the center of the duct enables a few crystals to grow at low rates resulting in a more coarse crystal structure compared to regions closer to the wall of the duct. There, the faster cooling enables nuclei formation at lower temperatures. Consequently, more nuclei are formed that grow at higher rates resulting in a fine grained structure.

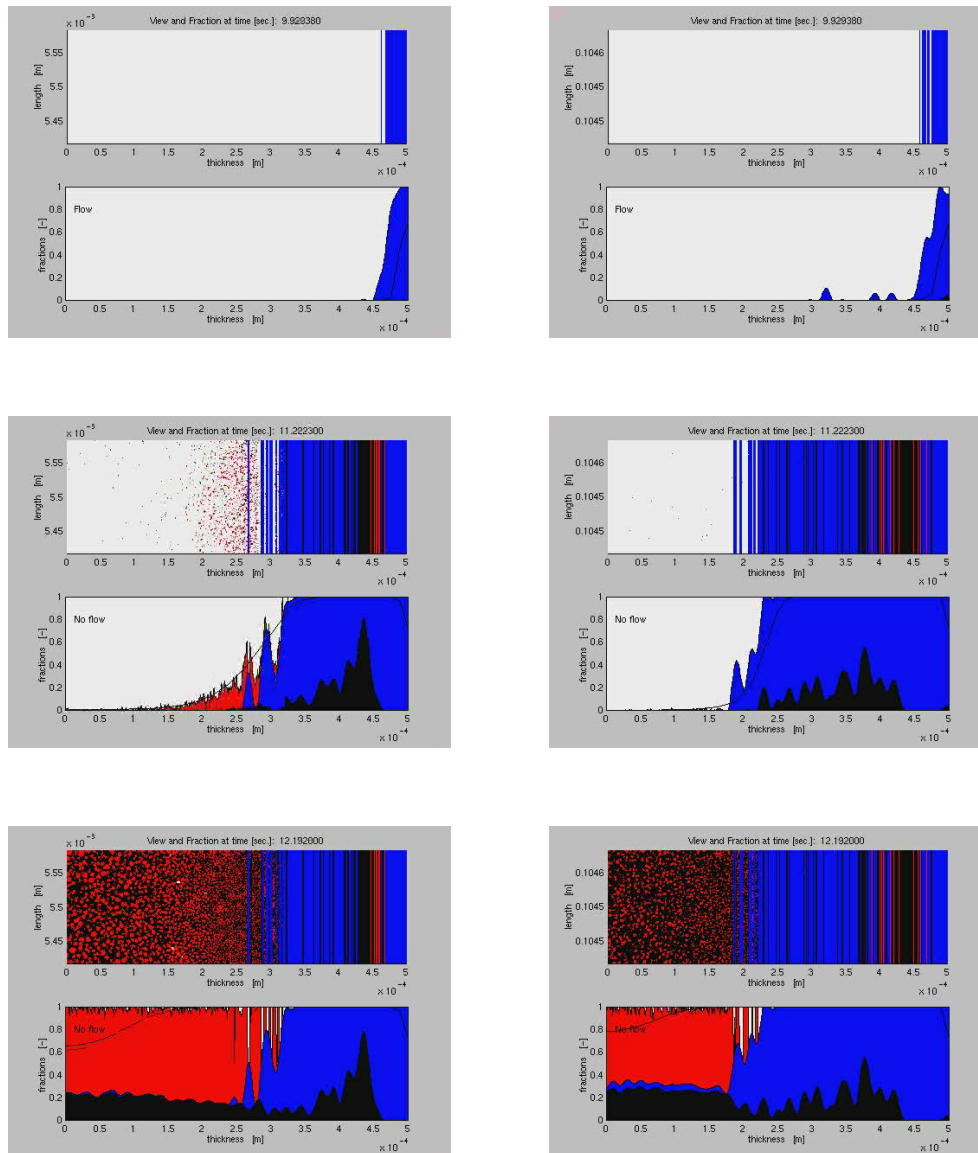


Fig. 3.10: Reproduction of the structure development from the center of the plate (thickness = 0 [m]) to the surface (thickness = 0.0005 [m]) for different moments during crystallization (upper parts), together with an impression of the local and global degree of crystallinity (lower parts).

3.4 Formulation of a recoverable strain based crystallization model

Based on the modeling results presented in section 3.3, a modification of the flow-induced model of Eder (section 3.1) is now applied and instead of the shear rate as a driving force for nucleation and shish extensioning, the molecular orientation represented by the recoverable strain is used. The second invariant of the deviatoric part of the recoverable strain, J_2 , gives the model proposed (S_{J_2} -model) its name and it can be summarized by the following set of differential equations:

$$\begin{aligned}
 \dot{\psi}_3 + \frac{\psi_3}{\tau_n} &= 8\pi J_2 g'_n & (\psi_3 = 8\pi N_f) & \quad (a) \\
 \dot{\psi}_2 + \frac{\psi_2}{\tau_l} &= \psi_3 J_2 \frac{g'_l}{g'_n} & (\psi_2 = 4\pi L_{tot}) & \quad (b) \\
 \dot{\psi}_1 &= G\psi_2 & (\psi_1 = S_{tot}) & \quad (c) \\
 \dot{\psi}_0 &= G\psi_1 & (\psi_0 = V_{tot}) & \quad (d) \\
 -\ln(1 - \xi_g) &= \psi_0 & & \quad (e)
 \end{aligned} \tag{3.7}$$

In eqn. 3.7, ξ_g is the degree of space filling, ψ_0 the undisturbed total volume V_{tot} of the shish-kebabs per unit of volume (impingement and swallowing are disregarded), ψ_1 the total surface S_{tot} of the shish-kebabs per unit of volume, ψ_2 4π times the total length of the shish L_{tot} per unit of volume, ψ_3 8π times the number of flow-induced nuclei N_f per unit of volume, τ_n the relaxation time for the nuclei, τ_l the relaxation time for the shish, J_2 the second invariant of the deviatoric part of the recoverable strain tensor (driving force), g'_l the scaling parameter for the influence of J_2 on the thread-like growth of the nuclei and g'_n the scaling parameter for the influence of J_2 on the number of nuclei.

The driving force J_2 acts twofold. First, in the equation for the nucleation rate (3.7a) the $\dot{\gamma}^2$ term is replaced by J_2 and the corresponding parameter g_n is replaced by a new parameter g'_n . The underlying idea is that the molecular orientation, generated by the flow, increases the possibility that part of a molecule reaches a conformation close to the crystalline state and so enhances nucleation. Second, in the equation for shish growth (3.7b) the $\dot{\gamma}^2$ term is replaced by J_2 and a parameter g'_l is introduced. The orientation by flow enhances the possibility that nuclei grow to shish and the shish increase their length. As a shish is a crystalline structure, relaxation, governed by the relaxation time τ_l , can only occur via melting. Since we do not consider this, the relaxation time is set to $\tau_l = \infty$.

If in nucleation different molecules are involved, nucleation sites act as physical crosslinks which cause the rheological relaxation time to increase. As shown, only the highest rheological relaxation time correlates with flow induced crystallization and this relaxation time is, in its turn, most strongly related to the high-end tail of the molecular weight distribution. Accordingly, the high molecular weight molecules are most influenced by this crosslinking. We, therefore, propose a link between the number of nuclei and the highest rheological relaxation

time. A simple linear relationship is chosen,

$$\theta_j = a_T(T) \theta_{j0} \left(1 + \frac{\alpha N_f}{g'_n}\right) \quad (3.8)$$

with θ_{j0} the rheological relaxation time at the reference temperature, $a_T(T)$ the time-temperature shift function and α the scaling parameter of the influence of the number of nuclei on the rheological relaxation time. This part of the model proves to be essential for obtaining the same distribution of nuclei and shish across the thickness, in comparison with the Eder model (18). Since an increasing relaxation time renders an increased orientation, flow induced nucleation becomes a self-enhancing process creating locally strongly oriented domains. Moreover, we could speculate that memory effects often observed (the effect of flow on nucleation and crystallization is still present, even after prolonged heating well above the melting temperature) could be related to this process. While the Eder model only describes the creation of the shish-kebab structures during shear, the relaxation time for the shish length has to be set to infinity after the flow has stopped, to prevent the structure calculated from disappearing. Moreover, the driving force $\dot{\gamma}$ in the Eder model is present instantaneously and disappears immediately after the flow has stopped. For the S_{J2} -model however, the startup behavior of the melt results in an increasing driving force J_2 after the start of flow. After the cessation of flow, the driving force J_2 very slowly decays and the structure calculated relaxes very slowly, which correlates with the observed memory effects, as memorized previously. Given the close connection between the number of nuclei and the rheological relaxation time θ_j , the last is also used as the relaxation time for the number of nuclei present; $\tau_n = \theta_j$. However, also other choices can be made. Finally, without being restrictive, the model parameters can be determined more easily if the two parameters: (i) the influence of the number of nuclei on the rheological relaxation time (α) and (ii) the scaling parameter for the total length of the shish (g'_l), are themselves scaled with the scaling parameter for the number of nuclei (g'_n).

3.5 Qualitative validation of the model

Simulations are performed for the short term shear experiments described earlier (section 3.2), using both the Eder model and the new S_{J2} -model. They include two wall shear rates (79 and 115 [s^{-1}]) and different shearing times. The viscoelastic part of the calculation is stopped after the value of the first mode of the recoverable strain becomes $\leq 0.5\%$ of the maximum value. The parameters in the model are obtained by fitting only one benchmark experiment (wall shear rate 72 [s^{-1}], shear time 7 [s]) and are listed in table 3.1.

All numerical results are compared with the experimental results and predictions from the Eder model. In fig. 3.11 the predicted position of the interface between the highly oriented layer and the fine grained layer, next to it, is shown. For a wall shear rate of 79 [s^{-1}] both models predict almost exactly the same position for the interface, while for a wall shear rate of 115 [s^{-1}] the S_{J2} -model gives slightly better results in the low shear time region (when compared with experimental results) and almost exactly the same result for the higher shear times. Fig. 3.12 shows the number (left) and total length of the shish (right) across the sample thickness for the benchmark experiment. Again both models predicted nearly the same

| | | |
|----------|-----------------------|-----|
| g'_n | $2.017 \cdot 10^{11}$ | [–] |
| g'_l | $1.429 \cdot 10^{-1}$ | [–] |
| α | $7 \cdot 10^{-6}$ | [–] |

Tab. 3.1: Parameters for the S_{J_2} -model of isotactic polypropylene Daplen KS10 (Borealis), in which g'_n is the scaling parameter for the influence of the driving force J_2 on the number of nuclei, g'_l the scaling parameter for the influence of the driving force J_2 on the thread-like growth of the nuclei and α the scaling parameter for the influence of the number of nuclei on the rheological relaxation time.

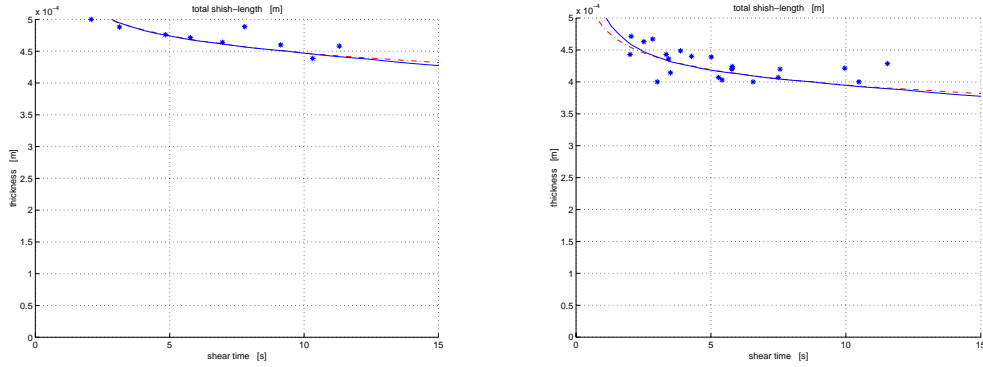


Fig. 3.11: Measured (*) position of the boundary of the flow-induced layer for different shear times, together with the numerically determined position of this boundary using both the Eder model (dashed line) and the S_{J_2} model (solid line), for a wall shear rate of approximately 79 (left) and 115 [s^{-1}] (right).

distribution.

In fig. 3.11, we noticed a small difference between the numerical results of the Eder and S_{J_2} -model for a wall shear rate of 79 [s^{-1}] at high shear times, increasing with increasing shear time (larger strains) and at a wall shear rate of 115 [s^{-1}] another difference is present at small shear times (small strains).

We will now investigate seemingly small differences like these in more detail by considering typical phenomena, observed in the literature ((18), (20), (29), (44), (51), (52), (87)). In order to do so, the induction time, or onset time, needs to be defined, by equalizing it to the time needed to reach a degree of crystallinity of $\xi_g = 0.001[-]$ at a temperature of $T = 423[K]$. In fig. 3.13 results are shown for the Eder model (top, left), for the S_{J_2} -model (top, right) and the difference between both (bottom) in shear flow after different shear rates and times. The main difference is present at low strains and high shear rates. This is consistent with the differences found in fig. 3.11, and it causes e.g. a deviation between both models at the entrance of the duct and at the flow front when simulating the injection moulding process. The relevancy of these differences in predictions will now be made more transparent by comparing them with some striking experiments from the literature. Despite that all materials

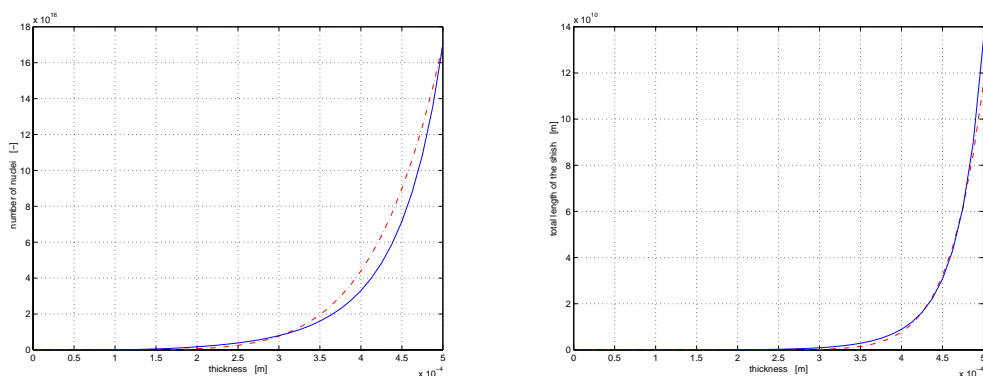


Fig. 3.12: Calculated number of nuclei (left) and their total length (right) for both the Eder model (dashed line) and the S_{J2} model (solid line), for a wall shear rate of $72 [s^{-1}]$ and a shear time of $7 [s]$ at a temperature of $423 [K]$.

used are isotactic polypropylenes, in the following (most of) the numerical simulations can only qualitatively be compared with experimental results, because of the lack of a full set of material data.

In experiments by Vleeshouwers (87), three isotactic polypropylenes with different molar mass distribution were studied. After a well defined shear treatment of the melt on a standard RDS II rheometer, using a cone and plate configuration, at an elevated temperature, and a subsequent quench to the crystallization temperature, the storage (G') and loss modulus (G'') were monitored. The onset of crystallization was graphically determined by drawing tangents along G' and G'' in the nearly horizontal regime, where crystallization hardly influences the moduli, and in the regime of maximum rate of change. The intercept is called the induction time, a measure for the time evolved before crystallization becomes noticeable. Experiments at a constant total shear treatment showed that increasing the shear rate (and consequently decreasing the shear time) lowers the induction time (fig. 3.14, right). Using the data for polypropylene (Daplen KS10, Borealis), crystallization kinetics are calculated, using a temperature profile that resembles the one Vleeshouwers (87) used, and induction times are calculated for a constant total shear of $\gamma = 250[-]$. In fig. 3.14 (left side) the results are shown for both the Eder and the S_{J2} -model. Both models confirm the experimental observations by Vleeshouwers (87), although the Eder-model shows the effect at constant shear more pronounced. However, measurements by Vleeshouwers (87) indicate the presence of a plateau region at low shear times. This probably is related to the difference in startup behavior of the material used by Vleeshouwers (87) and the polypropylene Daplen KS10 (Borealis) used for the prediction of the induction time. Vleeshouwers (87) also performed experiments with a constant shear rate during various shear times. These experiments showed a strong decrease in induction time in the low total strain region (low shear times), while in the high total strain region (high shear times) the induction time decreases much more gradually, including a sharp transition from one region to the other (fig. 3.14, right). In fig. 3.14

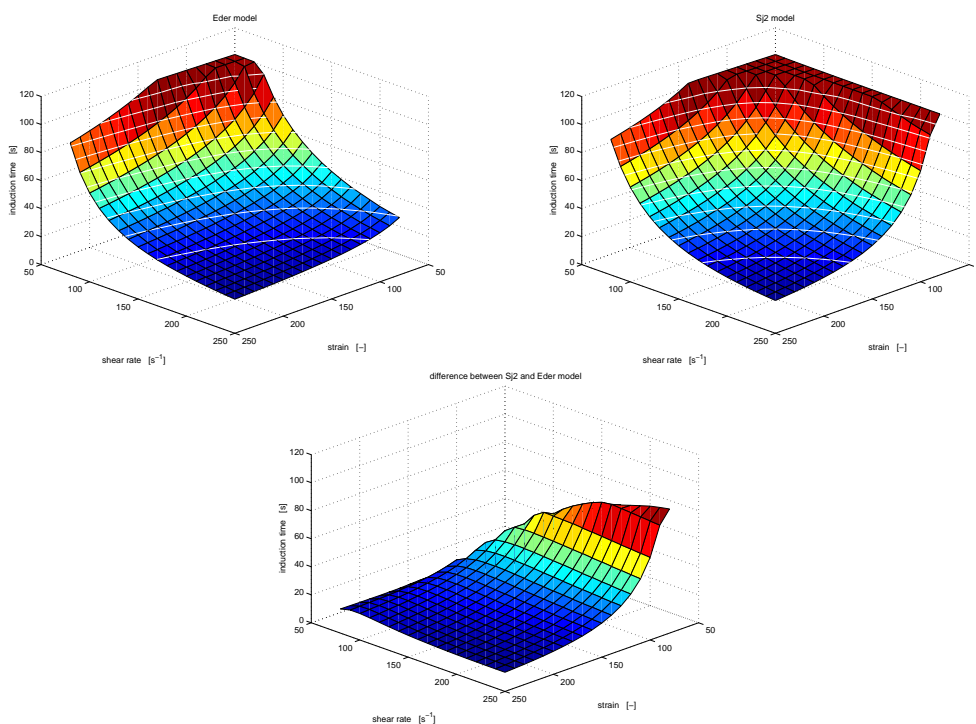


Fig. 3.13: The induction time according to the Eder model (top, left), the S_{J2} -model (top, right) and the difference between both (bottom) for polypropylene Daplen KS10 (Borealis).

(left side) the calculated induction time is shown as well for a constant shear rate $\dot{\gamma} = 5[s^{-1}]$, using the procedure described previously. Both the Eder and the S_{J2} -model confirm to the observations, although for the Eder model the transition is present at a slightly lower total strain (lower shear time) than for the S_{J2} -model.

The influence of molar mass (distribution) on the crystallization process after a shear treatment, was studied by Vleeshouwers by comparing the storage (G') and loss modulus (G'') in time of two isotactic polypropylenes (iPP1: $M_w = 500[kg/mol]$ and $M_n = 100[kg/mol]$; iPP2: $M_w = 375[kg/mol]$ and $M_n = 50[kg/mol]$). Experiments showed that for quiescent crystallization the polymer with the low molar mass (iPP2) crystallizes faster than the one with the high molar mass (iPP1). For iPP2 the application of shear hardly enhances the crystallization rate, while for iPP1 a large effect of shear is observed. This is in accordance with observations by Jerschow (44), who concluded that if long polymer chains are present, shear induced crystallization is more sensitive to shear treatment. Using the data for polypropylene (Daplen KS10, Borealis), crystallization kinetics are calculated for a shear rate $\dot{\gamma} = 5[s^{-1}]$, different shear times $t_s = 0, 25, 38, 50, 100$ and $200[s]$ and a temperature profile which resembles the one Vleeshouwers used. Studying the influence of the molar

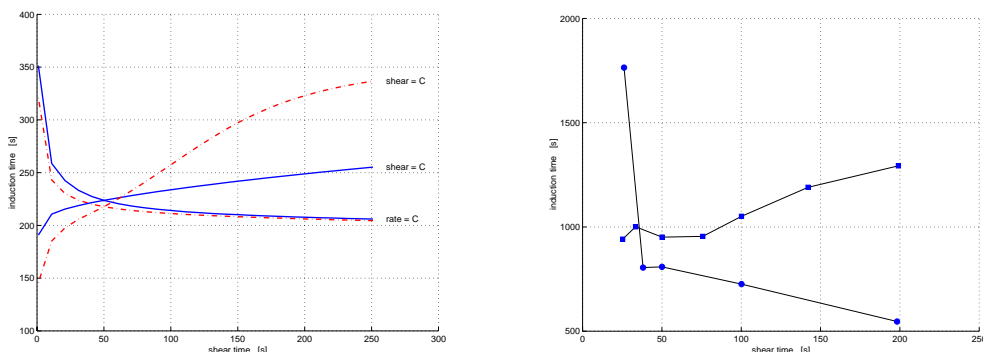


Fig. 3.14: Left side: The induction time at a constant shear rate ($\dot{\gamma} = 5[s^{-1}]$) according to the S_{J2} -model (solid line) and the Eder-model (dashed-dotted line), together with the induction time at a constant total shear ($\gamma = 250[-]$) according to the S_{J2} -model (solid line) and the Eder-model (dashed-dotted line) at different shear times. Right side: The measured induction time at a constant shear rate ($\dot{\gamma} = 5[s^{-1}]$) after Vleeshouwers (87) (●), together with the induction time at a constant total shear ($\gamma = 250[-]$) after (87) (■).

mass is hardly possible in the typical process related (shear rate based) Eder model. It can be done by adjusting the model parameters g_n and g_l (eqn. 3.4), although it can not be linked to any material parameter. Fitting the models predictions with experimental results, a very labour-intensive procedure, therefore is the only possibility of studying the influence of the molar mass. In the material related, recoverable strain based S_{J2} -model, this influence can, however, be modeled; one of its major improvements and innovations. To this end (and since no detailed rheological data of Vleeshouwers' materials are available), the high-end tail of the molecular mass distribution of the 'standard' polypropylene is 'removed' in the model by decreasing the largest rheological relaxation time to (an arbitrary value of) half the value of the 'standard' polypropylene ($\theta_1 = 14.97[s]$ and $\theta_1 = 29.7[s]$ respectively). Because the degree of crystallinity is closely related to the modulus, we assume that the degree of crystallinity is a direct measure for the changes in the modulus as observed by Vleeshouwers. Results are presented in fig. 3.15 for both the 'standard' (upper part) and the 'modified' polypropylene (lower part). The difference clearly shows that lowering the maximum relaxation time, representing a change in the high end tail of the molar mass, has a pronounced influence on the crystallization kinetics, similar to the effect observed by Vleeshouwers (87). This again supports the idea that the flow induced structure correlates most strongly with the viscoelastic mode with the highest relaxation time as postulated in section 3.3 and, moreover, proves the superiority of the S_{J2} -model over the Eder model.

Similar experiments like those by Vleeshouwers (87) were done by Lagasse (52) on an isotactic polypropylene. A parallel plate rheometer was used during isothermal flow ($T = 394[K]$) at a constant shear rate ($\dot{\gamma} = 4.25, 2.13, 1.07$ and $0.533[s^{-1}]$). The crystallization rate was characterized by the time (induction time) elapsed from the start of shearing until the rise in the melt viscosity due to crystallization was noticed. It was found that this

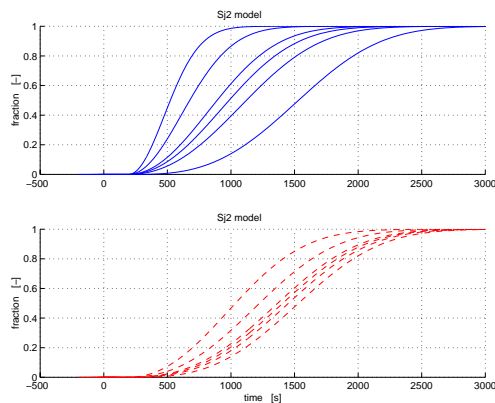


Fig. 3.15: Degree of crystallinity as a function of time for a shear rate $\dot{\gamma} = 5[s^{-1}]$ and different shear times $t_s = 0, 25, 38, 50, 100$ and $200[s]$, using 'standard' (upper part) and 'modified' polypropylene (numerically removed high-end tail of the molecular mass distribution, lower part).

rise in viscosity correlated with the appearance of crystals in the sheared melt. The results suggest a plateau region for the induction times at shear rates lower than $\dot{\gamma} = 0.7[s^{-1}]$. Critical values for the shear rate applied for (more than) a critical shear time were also observed by Eder (18; 20), and Kumaraswamy (51). Critical shear rate and induction time are used in modeling flow induced crystallization kinetics by Guo (29). In their work the induction time for shear induced crystallization is an explicit function of a molecular deformation factor, which in its turn is related to a critical shear rate of activation for a specified type of crystalline structure. Using the S_{J2} -model (which does not contain an explicit function for the induction time), the 'induction time' ($t(\xi_g = 0.001[-])$) for polypropylene Daplen KS10 (Borealis) was calculated for shear rates ranging from $\dot{\gamma} = 0.1[s^{-1}]$ until $\dot{\gamma} = 10[s^{-1}]$. This range includes the shear rates as used by Lagasse (52). In figure 3.16 the induction times measured by Lagasse (52) are presented together with numerical predictions using the S_{J2} -model. Although two different kinds of polypropylenes are used, the numerical results not only show the same kind of behavior as the measurements but (coincidentally) the same level. On the one hand, both show a plateau region at a shear rate lower than $\dot{\gamma} = 0.7[s^{-1}]$. The plateau value obtained numerically is a little lower than the measured plateau value, which can be due to our criterion for the induction time. On the other hand, both show a decreasing induction time above $\dot{\gamma} = 0.7[s^{-1}]$, although the slope differs slightly, which is probably due to different material characteristics (nuclei and crystal growth rate distribution).

Finally, verification of some, until now, not very well understood experimental results by Jerschow (44) is possible. The experiments performed were already described in section 3.2.2 using polypropylene (Daplen KS10, Borealis) (Jerschow (43)). They observed a significant difference in the crystallization behavior, when the monitoring time at which a particular amount of oriented structure is found, is plotted against the applied shearing time.

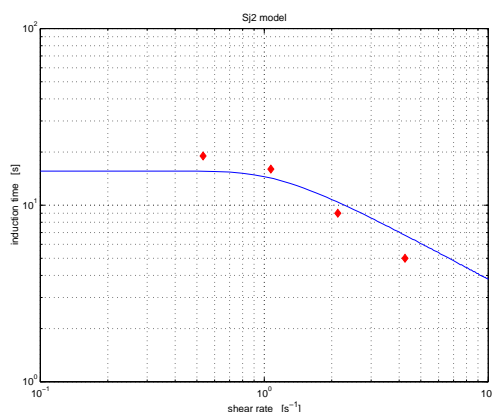


Fig. 3.16: The induction time according to the S_{J2} -model for polypropylene Daplen KS10 (Borealis) together with measurements by Lagasse (52) (◆) for their polypropylene.

The slope of the experimentally obtained results is -1 in the case of high shear rates, while the slope decreases at lower shear rates (fig. 3.17). The reason for this can not be captured by the Eder model. Since these experiments were done isothermally, the difference in slope is related to the nucleation and growth behavior of the shish-kebabs in the material during flow. Using the S_{J2} -model the monitoring half time (in our definition $t(\xi_g = 0.5[-])$) is calculated for the same polypropylene (Daplen KS10, Borealis) for shear times ranging from $t_s = 1[s^{-1}]$ until $t_s = 10[s^{-1}]$ for shear rates of $\dot{\gamma} = 15, 65$ and $115[s^{-1}]$ and a temperature of $T = 423[K]$. Results (fig. 3.17) at a shear rate of $\dot{\gamma} = 115[s^{-1}]$ have a slope of approximately -1, while at a lower shear rate ($\dot{\gamma} = 65[s^{-1}]$) the slope decreases. At a very low shear rate ($\dot{\gamma} = 15[s^{-1}]$) the slope even changes with increasing shear time. This is related to the startup behavior of the material. All these results agree with the observations of Jerschow (44). Following our model, a higher shear rate alters the viscoelastic state of the material more strongly. Consequently, molecular ordering is increased, which results in a higher nucleation rate and stronger shish growth by the driving force J_2 . Since a higher nucleation rate and, consequently, a higher nuclei density, increases the rheological relaxation time of the highest mode (eqn. 3.8), the relaxation time for the number of nuclei increases. The higher this relaxation time is, the more effective is the shear treatment for creating shish-kebabs, which results in an increasing slope.

Jerschow (44) also observed a significant difference in the crystallization behavior between an old and a new grade of the same material (Daplen KS10, Borealis). When the monitoring time at which a particular amount of oriented structure is found, is plotted against the shearing time applied, the slope of the experimentally obtained results is -1 in the case of the new grade, while the old grade results in a slope of -2 (fig. 3.18). Using the S_{J2} -model, at a constant shear rate, for example $\dot{\gamma} = 115[s^{-1}]$ at a temperature of $T = 423[K]$, a change in the material behavior is obtained similar to that observed by Jerschow (44) when the scaling parameter for the influence of the number of nuclei on the rheological relaxation time α is

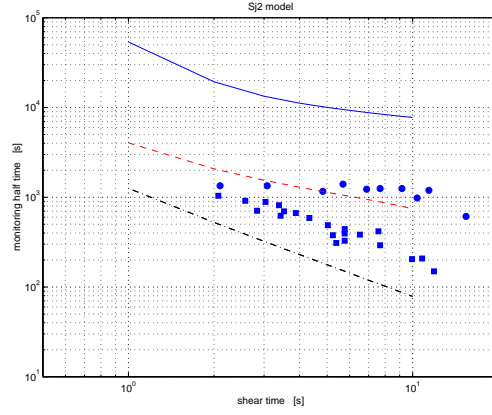


Fig. 3.17: The monitoring half time according to the S_{J2} -model for polypropylene Daplen KS10 (Borealis) at different shear rates (solid line: $\dot{\gamma} = 15[s^{-1}]$, dashed line: $\dot{\gamma} = 65[s^{-1}]$ and dashed-dotted line: $\dot{\gamma} = 115[s^{-1}]$), together with measurements by Jerschow (44) at different shear rates (\bullet : $\dot{\gamma} = 76[s^{-1}]$, \blacksquare : $\dot{\gamma} = 115[s^{-1}]$, both at a temperature $T = 423[K]$).

modified. For three different values ($\alpha = 6 \cdot 10^{-6}[-]$, $\alpha = 7 \cdot 10^{-6}[-]$ and $\alpha = 8 \cdot 10^{-6}[-]$) the monitoring half time (in our definition $t(\xi_g = 0.5[-])$) is calculated for these α values using the S_{J2} -model. Results (fig. 3.18) show the increasing slope with increasing α . This indicates that the difference in material behavior observed by Jerschow (44) could be related to the influence of the number of shish-kebabs created by flow, on the rheological behavior of the material, although a physical explanation is not available at this time. This type of behavior can not be obtained by varying one of the other parameters g'_i and g'_n .

3.6 Discussion

From the shear flow experiments done by Jerschow (43) and the resulting shear induced crystallization model of Eder (18), it was concluded that for shear induced crystallization precursors are formed during flow, which reach the same effectiveness at $\dot{\gamma}^4 t_s^2 = \text{constant}$, indicating that the boundary between the observed fine grained layer and the highly oriented layer is characterized by $\dot{\gamma}_c^4 t_s = \text{constant}$. In the same way it was concluded that the boundary between the fine grained layer and the core is characterized by $\dot{\gamma}_c^2 t_s = \text{constant}$. An improvement of Eder's model is proposed that replaces the process parameter 'shear rate' by the material parameter 'recoverable strain'. For very different thermo-mechanical histories, like isothermal flows with different shear rates, shear time and steady flows, a strong correlation is found between the experimentally determined position of these layers and the ones predicted by the model that is based on the most simple functional (the integral in time) of the second invariant of the deviatoric part of the recoverable strain $J_2(\bar{\mathbf{B}}_e^d)$ for the maximum rheological relaxation time. A real material constant is found for the prediction of these transition layers. The evolution of the recoverable strain is described using the Leonov model, however differ-

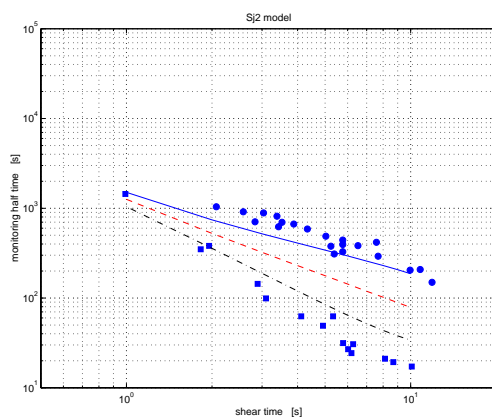


Fig. 3.18: The monitoring half time according to the S_{J_2} -model for 'modified' polypropylene Daplen KS10 (Borealis) at a shear rate of $\dot{\gamma} = 115[\text{s}^{-1}]$. The parameter α for the scaling of the influence of the number of nuclei on the rheological relaxation time differs (solid line: $\alpha = 6 \cdot 10^{-6}[-]$, dashed line: $\alpha = 7 \cdot 10^{-6}[-]$ and dashed-dotted line: $\alpha = 8 \cdot 10^{-6}[-]$), together with measurements by Jerschow (44) (\bullet : new grade at $\dot{\gamma} = 115[\text{s}^{-1}]$, \blacksquare : old grade at $\dot{\gamma} = 112[\text{s}^{-1}]$, both at a temperature $T = 423[\text{K}]$).

ent models like for example the Giesekus model, the Phan-Thien Tanner model, the recently proposed FETA models (Peters (68)) or (modified) POM-POM models (Verbeeten (84)) can easily be implemented.

The correlation between the layers in the flow-induced structure and the time integral of $J_2(\overline{\mathbf{B}}_e^d)$ corresponding to the maximum rheological relaxation time, indicates that reformulating the Eder model (18) for flow-induced nucleation and crystallization in terms of the elastic Finger tensor could be very successful. Such an approach is in the line with the work of McHugh et al. (12), which is based on a conformational tensor. However, the McHugh-model only gives a set of equations describing a conformation tensor, an orientation tensor and the degree of crystallinity, while no description is available of the final structure (size of structures, etc.). Indeed, the state of the material should be an important driving force and not the shear rate as in the Eder model (18). However, Eder's model has the important features of including all the properties that characterize the structure, it is simple in its design and, therefore, rather transparent and, finally, can be validated. Therefore, we kept Eder's structural model and reformulated it. The proposed formulation (section 3.4) serves as a starting point for further validation using different experiments (Swartjes (79)) and, if necessary, further adaptations of the model can be made. An important difference between both models is, moreover, the ability of the S_{J_2} -model to predict the influence of the molecular weight distribution, that can be measured via *independent*, rheological, experiments. In detail, the Eder model is based on the shear rate with the consequence that the elongational component in the strain rate is not included. In contrast, the S_{J_2} -model is based on the complex strain present, which is, nowadays, readily calculated even in complex flows.

Chapter 4

*Influence of Cooling Rate on pVT-behavior of Semi-Crystalline Polymers*¹

Two different techniques are commonly applied when measuring the specific volume:

The piston-die technique: The material is enclosed and pressurized in a die using a piston. The volume of the material is registered during the measuring cycle using the displacement of the piston. Both temperature and pressure can be varied, however the pressure applied is not hydrostatic because the material sticks to the wall (He (31)). According to Zoller (92) this technique only gives accurate results when the shear modulus of the material is much smaller than its bulk modulus, which is the case for polymer melts. However, when the degree of crystallinity increases, due to crystal growth in the sample, the material will behave more like a rubber/solid and measurements will become inaccurate. Other problems are the possible leakage between the piston and the die, and the formation of voids in the sample when solidifying. The technique was, for instance, applied by Chang (10) who used a pVT-100 apparatus from SWO Germany (26).

The confining fluid technique: The sample is enclosed in a sample cell containing a confining fluid. The cell is closed using a bellows, whose displacement is registered during a measuring cycle, giving the relative volume difference of the sample. The absolute specific volume can be obtained by correcting for the relative volume difference with the specific volume of the confining fluid. Both pressure and temperature can be varied. Moreover, the pressure is purely hydrostatic as the sample is surrounded by the confining fluid. Other advantages are the absence of leakage and friction problems. Problems with this technique are the possible interaction of the confining fluid with the sample. Most of the time mercury is used as the confining fluid although no published pVT data for mercury above about 463[K] are available (92). The technique is, for instance, applied by Moldflow (61) using a GNOMIX PVT testing apparatus.

With both techniques two different measuring modes can be performed:

Isobaric mode: The volume is measured while a constant pressure is maintained and the temperature is varied, with a constant cooling or heating rate. When the temperature scan is completed, another pressure is selected and the temperature is varied again. If an increasing temperature scan is used, the initial crystal structure of the sample has to be known for semi-crystalline polymers in order to have a reference point for the specific volume measured. For the piston-die technique only a decreasing temperature sequence can be used since the material has to melt in order to fill the die completely.

¹ This chapter is reproduced in part from Zuidema et al. (95)

Isothermal mode: The volume is measured at selected temperatures, while the pressure is varied. Again, using an increasing temperature scan, the initial crystal structure of the sample has to be known, and for the piston-die technique only a decreasing temperature sequence can be used.

During a measuring cycle a steady state in the material is assumed, which implies that cooling and heating rates are restricted to $0.83[K s^{-1}]$ at maximum in a DSC (He (31)) and to $0.167[K s^{-1}]$ for the confining fluid or piston-die technique (due to the sample size). However, in injection moulding, cooling rates depend on the thickness of the product. They change from very high values at the cavity walls to almost zero at the product core. For amorphous polymers one could assume that the specific volume measured still holds at these high cooling rates; for semi-crystalline polymers however, it will certainly not. Consequently, these standard techniques (confining fluid and piston die) can only be used for amorphous polymers or at low cooling rates for semi-crystalline polymers. Specific volume measurements at low cooling rates were done by Douillard (13) ($\dot{T}_{max} = 0.333[K s^{-1}]$), He (31) ($\dot{T}_{max} = 0.042[K s^{-1}]$) and Ito (38) ($\dot{T}_{max} = 0.033[K s^{-1}]$). The actual specific volume was measured during a cooling run. Sato (72) measured the specific volume of a semi-crystalline polypropylene and studied the effect of a sample cup holder and the sample form. Because crystallization kinetics were not included, direct and quantitative conclusions on the influence of the crystallization kinetics on the specific volume could not be drawn. Moreover, the absence of the influence of cooling rate in these measurements makes them inadequate for the use in injection moulding simulations.

An attempt to measure the specific volume of semi-crystalline polymers at higher cooling rates was performed by Lobo (60) using a combination of standard pVT and DSC measurements. DSC measurements were done on an injection moulded sample at the same heating rates as those in the pVT measurement. These were used in the analysis to calibrate the results from the DCS against the pVT apparatus. Isothermal measurements were first performed in the solid state over a wide temperature range using the pVT apparatus. Afterwards, the melting behavior at low pressures was determined. High cooling rate DSC measurements were performed to determine the cooling rate dependence of the crystallization transition. The pVT data were then constructed by piecing together the measured solid state pVT data of the injection moulded part with the measured melt state pVT properties using the cooling rate dependent crystallization transition. The maximum cooling rate applied was $1.667[K s^{-1}]$. However, it was shown by Wu (88) that DSC curves cannot correctly be interpreted if internal heat transfer problems of the DSC apparatus are ignored and, for cooling rates of $1.667[K s^{-1}]$, the influence of the temperature difference in the sample on the measurements is severe. Similar conclusions were drawn by Piccarolo (69).

To measure the specific volume for semi-crystalline polymers at high cooling rates, a different technique has to be applied. Piccarolo (69) measured the temperature at the sample surface during cooling of a sample from one side. The temperature distribution in the sample was calculated using the energy equation. After extracting the sample, the density distribution was measured using a density column. The structure of the sample was characterized using WAXD and optical microscopy. In this way, cooling rates up to $\dot{T} = 311[K s^{-1}]$ were

reached. However, since the specific volume is determined afterwards, information on the crystallization process in the sample (expressed by the specific volume) was not obtained.

When numerical simulations are involved, a mathematical representation of the specific volume is necessary. Many models, like the Tait equation (91), assume that the specific volume only depends on pressure and temperature. Modifying the Tait equation for cooling rate effects was done by Chang (10). The resulting set of equations only holds for amorphous polymers at a maximum cooling rate of approximately $0.167[K s^{-1}]$ and it was shown by Zoller (90) that, on the one hand, the Tait equation does not yield a good representation of the compressibility behavior of *solid* semi-crystalline polymers like polypropylene but, on the other hand, semi-crystalline polymer *melts* are represented well. Ito (37) adopted the specific volume equation for polystyrene proposed by Spencer and Gilmore (77), which is based on the van der Waals equation, in order to describe the specific volume of the isotactic polypropylene used. The specific volume is divided into three states (melt, crystallization and solid), with the knee-points obtained from crystallization kinetics calculated at the actual cooling rate. Although this results in a first order approximation for the specific volume of a semi-crystalline material, the actual crystallization kinetics are not included thoroughly. Crystallization kinetics equations were incorporated by Hieber (32), who used a two-domain Tait equation for the asymptotes at high and low temperatures. The specific volume at the transition was calculated using the Nakamura equation for crystallization kinetics and a linear interpolation from one asymptote to the other. For cooling rates up to $0.04[K s^{-1}]$ the modeling captures the transition to a first order approximation. For a cooling rate of $2[K s^{-1}]$, however, it was found from measured data at smaller cooling rates and modeling, that the measured data are suspect. Nevertheless, although it was concluded that their model oversimplifies the physics, they did not cast doubt. A different approach was followed by Fleischmann (22) who noticed that the specific volume for semi-crystalline polymers below the melting point increases with increasing cooling rates. This results from a suppressed crystallization process as low temperatures are reached fast. In order to get a grip on the phenomenon, a specific volume corrected for high pressures and high cooling rates was calculated, instead of using a calculated crystal structure distribution to determine the specific volume.

In summary, problems with standard pVT measurements on semi-crystalline polymers are:

- In both the isothermal and isobaric mode, when using an increasing temperature run, the initial crystal structure of the sample is not known. The reference point for such an experiment is absent.
- In both the isothermal and isobaric mode, when using a decreasing temperature run, the cooling rate influences the crystal structure and resulting specific volume. Moreover, a steady state in the material is assumed, while crystalline structures are continuously changing the specific volume. Specific volume measurements only show a moment in time of the processes during these measurements.
- In both an increasing and decreasing temperature run, when using the isothermal mode, pressure enhanced nucleation/(re)crystallization can occur. This means that all measured points at a particular pressure are influenced by the other pressures in the cycle. The material in accompanying pressure measurements possibly has a different crystalline structure and, as

a result, a different specific volume.

- Since high cooling rates cannot be reached in standard techniques, the results of these measurements are inadequate for injection moulding simulations.

A different experimental setup to measure the specific volume of semi-crystalline polymers could solve these problems. Since the cooling rate influences the crystal structure, measurements at different cooling rates are necessary; however, temperature gradients in the sample have to be prevented. Therefore, a setup based on the confining fluid technique was developed, that can reach cooling rates of the sample up to $60[Ks^{-1}]$ and pressures up to $20 \cdot 10^6[Pa]$. During an experiment the specific volume and temperature history of the thin sample are registered together with the pressure applied. Sample thickness is such that temperature gradients in the sample are negligibly small. The time-temperature development in the sample, an accurate model for the crystallization kinetics, and a crystallinity dependent model for the specific volume, and combining all these three aspects, results in accurate predictions of the specific volume. Measurement and simulation results can be compared to determine model parameters.

4.1 Methods

The material investigated is an isotactic polypropylene (K2Xmod, Borealis, see appendix A.3). When using the confining fluid technique, the basic experiment is the following:

- include the sample in the fluid cell,
- fill the cell with the confining fluid,
- build up the required pressure level,
- heat the cell to the required starting temperature,
- cool the sample.

Since in the injection moulding process high pressures can be present, the experimental setup has to be able to reach these values too in order to generate useful data. For this reason pressures have to be reached up to $p = \cdot 10^8[Pa]$. Temperatures should be able to reach $T = 623[K]$ to cover the melting temperatures of several polymers, while cooling rates should be as high as possible. Two experimental runs are necessary; one with the sample and one without the sample as a baseline for setup influences.

While cooling rates are high, the thickness of the sample should be as small as possible in order to minimize temperature gradients in the sample. A manageable maximum thickness of $\leq 0.35[mm]$ is chosen. Samples with a length of approximately $30[mm]$ and a width of approximately $18[mm]$ were formed by compression moulding pellets at a temperature $T = 500[K]$ at low pressures. Sample cooling was done at atmospheric pressure. Measurement of the experimental temperature takes place at six different positions at the cavity surface (T_{Lb}, \dots, T_{Ro}), while the pressure is measured at the top and the bottom of the cavity (P_b, P_o). The volume difference is registered using a LDVT displacement transducer (D) mounted to the bellows bottom (figure 4.1). To minimize the influence of heat on the rest of the measuring equipment, cooling channels are present at the top and the bottom of the heated area to create heat sinks (figure 4.2). When steady conditions are reached, the vicinity of the sample is quenched with pressurized water via cooling channels positioned close to the sam-

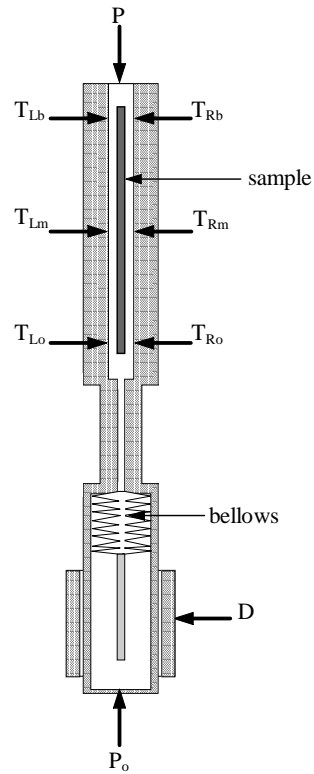


Fig. 4.1: Basic outline of the setup.

ple holding area (figure 4.2). During cooling, the temperature history, pressure and volume difference are measured at a frequency of 50 to 100[Hz], dependent on the cooling applied. Notice that the cooling rate is never constant but is determined by the flux and temperature of the coolant in combination with the heat capacity of the sample holding area. Since the flux is kept constant and the cooling rate thus varies, the actual temperature history will be used in analyzing the experimental results. The maximum in the time derivative of the temperature (\dot{T}_{max}) is called the cooling rate. The maximum cooling rate achieved is $54.2[K s^{-1}]$ (figure 4.3). The maximum pressure achieved up to now, without any experimental problem, was $p = 177 \cdot 10^5[Pa]$. The specific volume is obtained by relating the volume difference to the specific volume of the polymer melt at the starting temperature, measured using standard pVT measurements (Moldflow (61)).

Modeling the degree of crystallinity ξ is done using Schneider's rate equations (Schneider (74)). They fully characterize the structure, i.e. mean number of spherulites, their radius, surface and volume. These equations consist of a serie of nested differential equations (eqn. 3.1). The crystal growth rate G and the nucleation rate α have to be measured as a function of temperature. These rate equations are based on the generalized Kolmogoroff equation

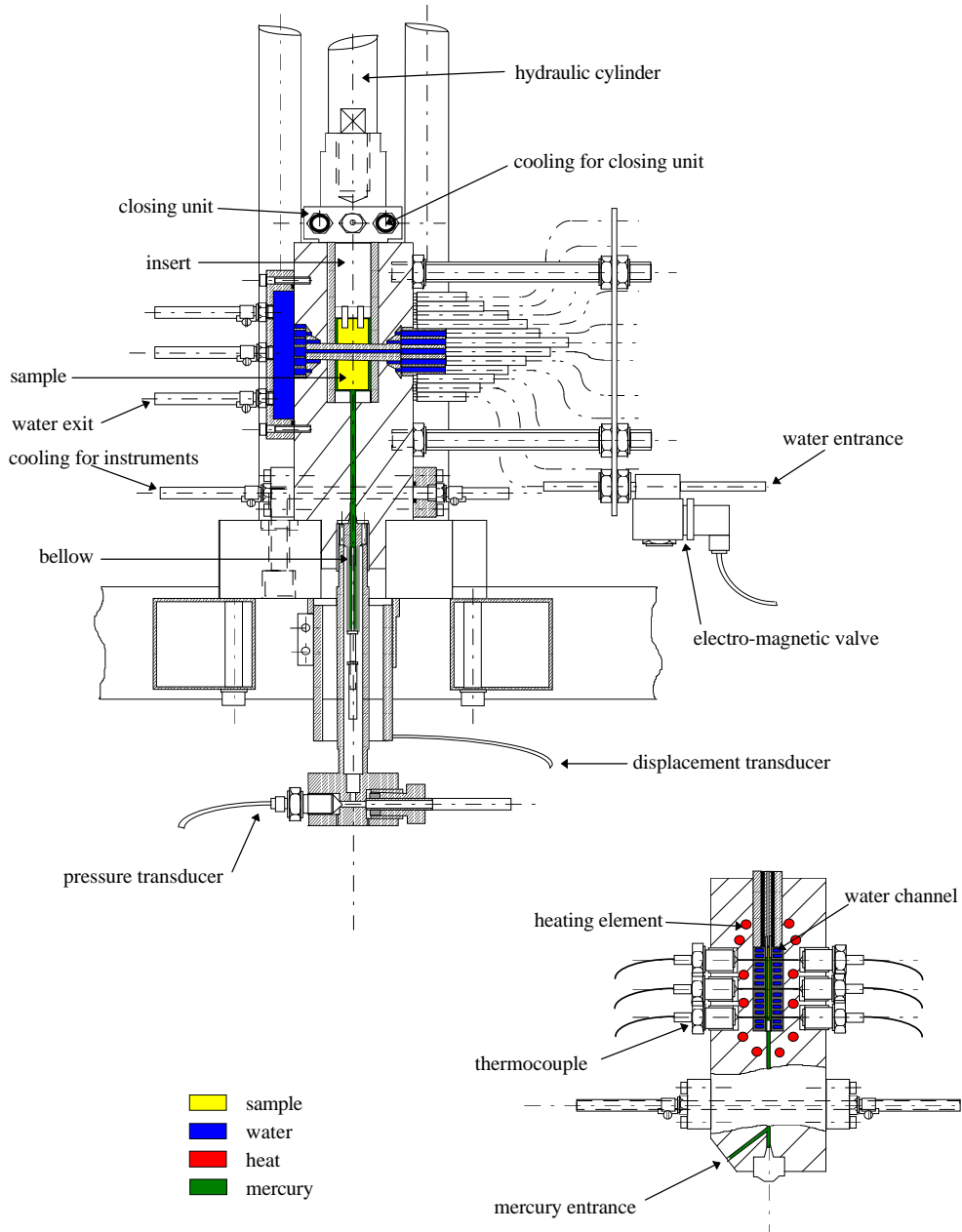


Fig. 4.2: Detailed outline of the setup.

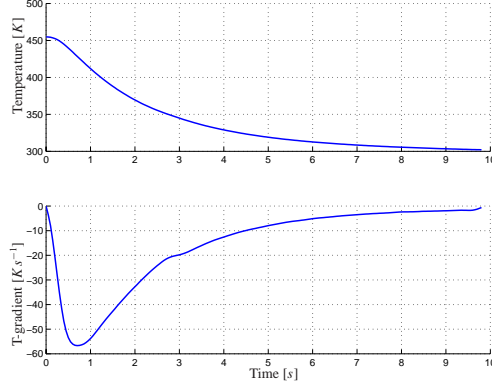


Fig. 4.3: Measured temperature signal in time (top), together with the calculated time derivative (bottom) in time.

(Janeschitz-Kriegl (39)), in which the nucleation is random in time and spatially uniform. Crystal impingement is described using the Avrami model (94) (eqn. 3.2). The degree of crystallinity ξ can be obtained by multiplying the degree of space filling with the local degree of crystallinity V_∞ in each spherulite. This set of equations (3.1, 3.2) fully characterizes the spherulitical structure development during an experimental run and the structure present in the sample is known all the time. When the degree of space filling ξ_g does not reach unity during an experimental run, the remaining portion of the material is assumed to be in a mesomorphic phase. This results, at high cooling rates, in a material consisting of spherulites in a mesomorphic matrix.

Since the specific volume v of a semi-crystalline polymer is always a combination of the amorphous and crystalline structure present, it is assumed that both phases are not influenced by each other. A crystallinity dependent model for the specific volume distinguishes between the amorphous ρ_a^* and the crystalline contribution ρ_c^* to the density ($\rho = \frac{1}{v}$) using the volume fraction of crystallized material $\xi_g V_\infty$, without mutual influences;

$$\rho = \xi_g V_\infty \rho_c^* + (1 - \xi_g V_\infty) \rho_a^* \quad (4.1)$$

Since the Tait equation does not yield a good representation of the compressibility behavior of solid semi-crystalline polymers (Zoller (90)), and the transition from melt to solid by crystallization is not a transition explicitly, it is not clear when the Tait equation can be used. Therefore, both the amorphous ρ_a^* and the crystalline contribution ρ_c^* are modeled using a Taylor series in temperature and pressure;

$$\Delta T = T - T_{ref} \quad (4.2)$$

$$\Delta p = p - p_{ref} \quad (4.3)$$

$$\rho_i^* = \rho_{ref,i} + \frac{\partial \rho_i}{\partial T} \Delta T + \frac{\partial \rho_i}{\partial p} \Delta p + \frac{\partial^2 \rho_i}{\partial T \partial p} \Delta T \Delta p + \frac{\partial^2 \rho_i}{\partial T^2} \Delta T^2 + \frac{\partial^2 \rho_i}{\partial p^2} \Delta p^2 \quad i = a, c \quad (4.4)$$

4.2 Results and discussion

The temperature and specific volume measured during an experimental run in the isobaric mode at $p = 1 \cdot 10^5 [Pa]$ are shown in fig. 4.4. The effect of the crystallization on the specific

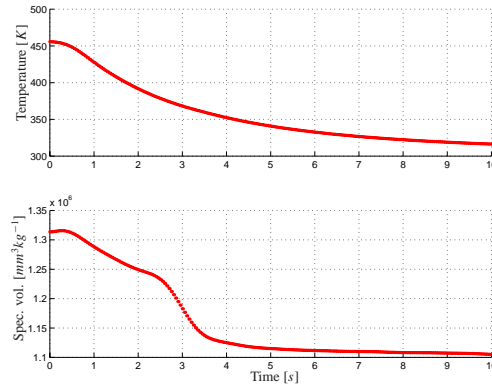


Fig. 4.4: Measured temperature signal in time (top) together with the measured specific volume signal in time (bottom) during an experimental run in the isobaric mode at $p = 1 \cdot 10^5 [Pa]$.

volume of the sample becomes noticeable around approximately $t = 3[s]$ after the start of the cooling (fig. 4.4, bottom). Using the time-temperature measurement as a boundary condition, predictions on the degree of crystallinity can be made using Schneider's rate equations (eqn. 3.1) and Avrami's model of impingement (eqn. 3.2). The specific volume can be calculated using the proposed formulation (eqn. 4.1 to eqn. 4.4) and the parameters shown in table A.9.

Comparison between the measured and the predicted specific volume is shown in fig. 4.5, together with the measured specific volume according to the standard procedure (Moldflow (61)). The most striking agreement between the measured and calculated specific volume is the temperature of the crystallization transition. The position of this transition depends on the crystal growth rate and the number of crystals present, which are both a function of the (local) temperature. A deviation in the measured temperature, which is used as a boundary condition for the simulations, will cause a difference in the position of this transition. Consequently, the modeling of the crystallization kinetics is in accordance with the physical phenomena measured. The main difference between the standard data and the measured specific volume is due to the influence of the procedure used. The standard data (Moldflow (61)) are measured using an increasing temperature run, which results in a melting transition around approximately $T = 430[K]$. The new measurements are performed using a decreasing temperature run, which results in a crystallization transition around $T = 370[K]$. The difference between these measurements, therefore, consists of the influence of the cooling rate on the crystallization kinetics (studied in the next subsection) together with a different physical phenomenon; melting versus crystallization. The latter can be observed in DSC runs as well. A similar difference in the transition temperature for the melting and crystallization

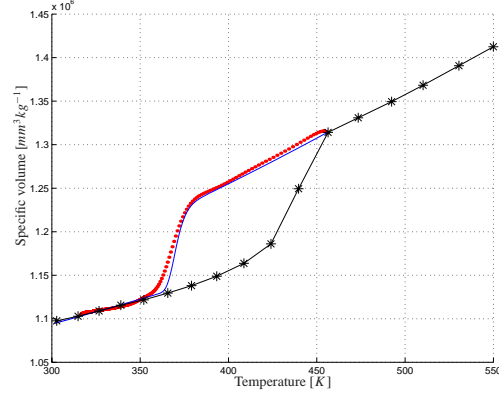


Fig. 4.5: Calculated (—) and measured (cooling cycle) (●) specific volume as a function of the measured temperature (see fig. 4.4, top) together with the measured (heating cycle) (*) specific volume according to the standard procedure (Moldflow (61)).

of polypropylene was observed by He (31). Moreover, from Fleischmann (22), Hieber (32), Zoller (90) and others, it is known that the crystalline phase has a much smaller temperature and pressure sensitivity than the amorphous phase. Our results are not in contradiction with this.

While the Schneider rate equations do not only describe the resulting degree of crystallinity, but also give a full description of the average properties of the resulting structure, it is possible to reproduce the structure development during crystallization by generating (at random) nuclei with an average rate equal to the local nucleation rate. For different times during crystallization, the distribution of the structure over the thickness of the sample is shown (fig. 4.6, left side), where the upper parts show the spherulitical structure. The lower parts give the local degree of crystallinity (solid), calculated by counting pixels in the upper part. When different crystals capture the same pixel by growth, this is registered as an interface. Moreover, the resulting structure in the sample can be compared easily by transforming the reproduction of the structure (fig. 4.6, left side) to the same structure when viewed using polarized light under a microscope (fig. 4.6, right side). The resulting main spherulite radius is approximately $7[\mu\text{m}]$, which is smaller than the $25[\mu\text{m}]$ measured by Piccarolo (69) under similar experimental conditions. However, as nucleation density in a material has large influence on this, the different polypropylenes used are probably the reason for this discrepancy.

Influence of cooling rate:

Different cooling rates are applied ($\dot{T}_{max} = 0.21, 33.96, 44.58$ and $54.22[\text{K s}^{-1}]$). In figure 4.7 the measured specific volume is shown together with the calculated one using the procedure described in the previous subsection. The shift in the crystallization transition, due to the different crystallization kinetics in the sample, is approximately $50[\text{K}]$ from a cooling rate of $\dot{T}_{max} = 0.21[\text{K s}^{-1}]$ to $\dot{T}_{max} = 54.22[\text{K s}^{-1}]$. At a low cooling rate ($\dot{T}_{max} = 0.21[\text{K s}^{-1}]$),

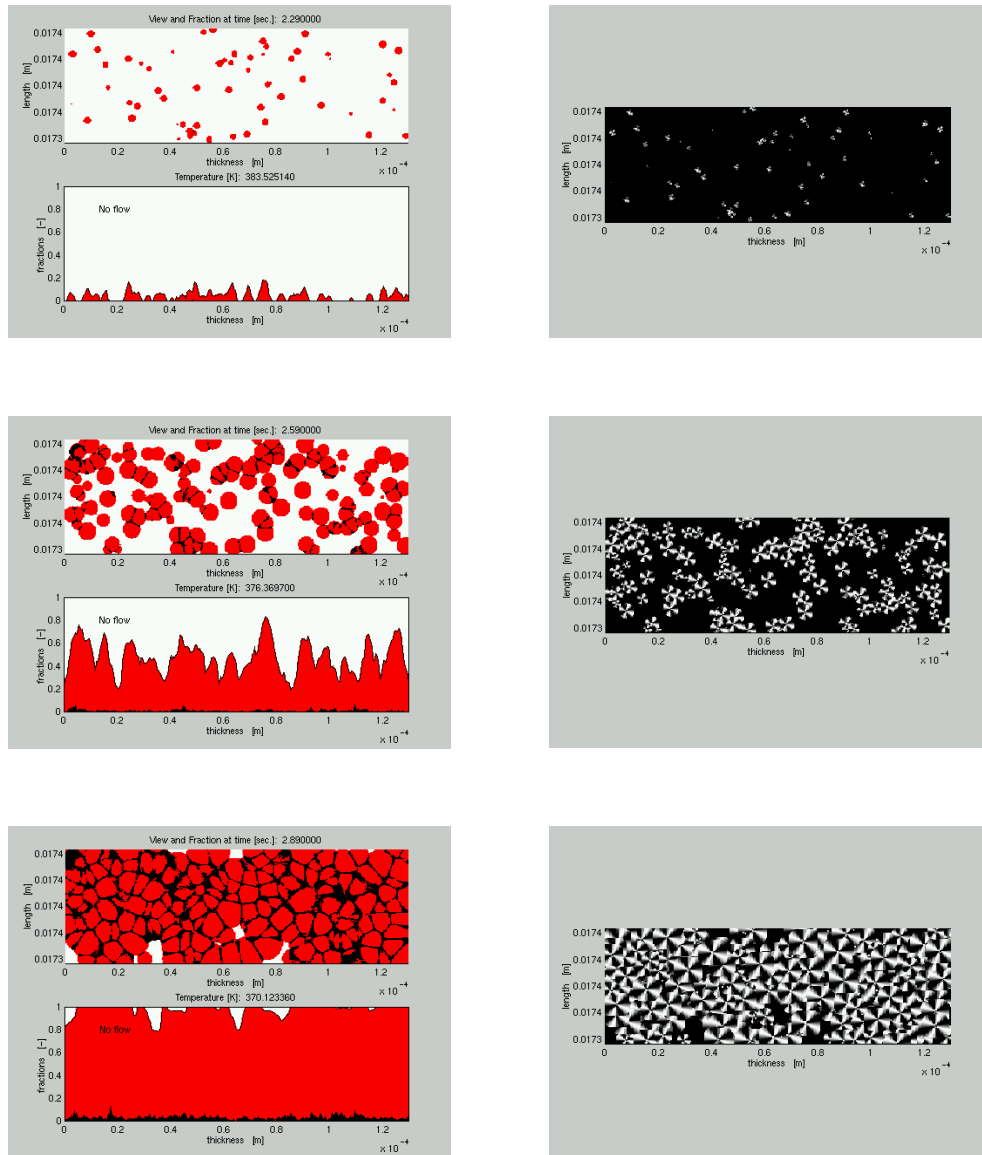


Fig. 4.6: Left side: Computed reproduction of the structure using Schneider's rate equations from the center of the sample (thickness = 0 [m]) to the surface (thickness = 0.00013 [m]) for different moments during crystallization (upper parts), together with an impression of the local degree of crystallinity (lower parts). Right side: visualization of the structure from the center of the sample to the surface when viewed using polarized light microscopy.

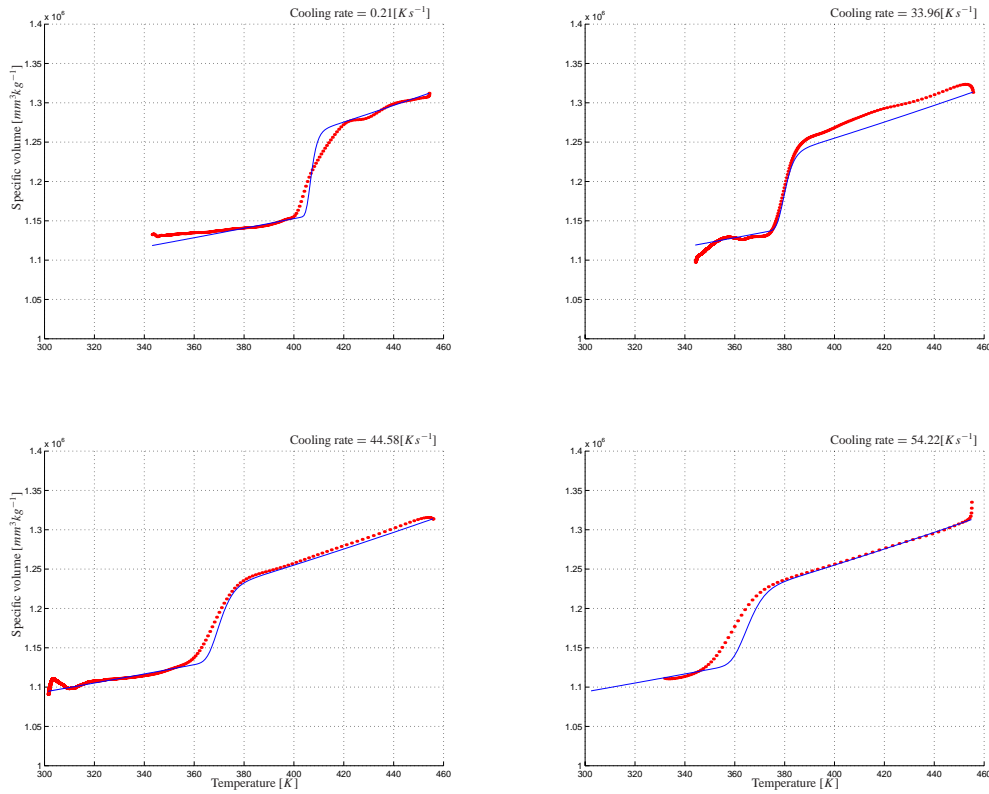


Fig. 4.7: Calculated (—) and measured (•) specific volume as a function of the measured temperature for different cooling rates ($\dot{T}_{max} = 0.21, 33.96, 44.58$ and $54.22[K s^{-1}]$).

the residence time at higher temperatures enables the growth of less crystals at low rates. In contrast, at a high cooling rate ($\dot{T}_{max} = 54.22[K s^{-1}]$) the residence time at higher temperatures is that low, that the degree of crystallinity hardly increases in that range. However, as cooling progresses to lower temperatures, the number of crystals and their crystal growth rate increases (see fig. A.5 and fig. A.6 respectively) and so will the degree of crystallinity. As a result, the transition in specific volume shifts to lower temperatures.

In the utmost case that the cooling rate is that high that the degree of crystallinity is still minor at very low temperatures ($T = 293...353[K]$), the crystal growth rate decreases with decreasing temperatures due to the lower molecular mobility at these temperatures (fig. A.6). Consequently, the degree of crystallinity will not reach the maximum value and the crystallization transition will be at a very low temperature and be less pronounced. The resulting structure then will consist of spherulites in a mesomorphic matrix as discussed in section 4.1. The agreement between the measured and the calculated specific volume is rather good at low cooling rates, while at high cooling rates there is a little difference. This might be caused by a different crystal structure at these cooling rates, which has a different crystal growth rate

distribution. This is in accordance with the work of Piccarolo (70), who stated that, at high undercoolings, the mesomorphic phase forms faster and with a high degree of disorder, while at low undercoolings mobility allows high growth rates to be obtained with the gain of a well-ordered α -monoclinic structure. For the low cooling rate experiment ($\dot{T}_{max} = 0.21[K s^{-1}]$), the crystallization transition temperature is around $T \approx 407[K]$, which is comparable with the value found by Ito (36), $T \approx 398[K]$, at a cooling rate of $\dot{T} = 0.0167[K s^{-1}]$ and atmospheric pressure.

Influence of pressure:

Different pressures are applied to study the influence of the pressure on the crystallization kinetics. The cooling rate applied in these experiments was around $\dot{T}_{max} = 40[K s^{-1}]$ (table 4.1).

| p | [Pa] | \dot{T}_{max} | [K s ⁻¹] |
|------------------|------|-----------------|----------------------|
| $3 \cdot 10^5$ | | 40.24 | |
| $26 \cdot 10^5$ | | 40.74 | |
| $101 \cdot 10^5$ | | 37.40 | |
| $177 \cdot 10^5$ | | 39.71 | |

Tab. 4.1: Different pressures applied to study the influence of the pressure on the crystallization kinetics together with the experimentally observed cooling rate.

In fig. 4.8 the measured specific volume is presented for all pressures. Besides a normal shift to a lower specific volume at a higher pressure, an extra shift in the crystallization transition temperature is present. This is caused by the shift in the crystal growth rate distribution to higher temperatures at an increasing pressure.

For a polypropylene, it was shown by Ito (38), that the melting and glass transition temperature depend linearly on pressure with a proportionality factor $a = 3 \cdot 10^{-7}[K Pa^{-1}]$. He (31) found this factor to be $a = 2.899 \cdot 10^{-7}[K Pa^{-1}]$ for the melting temperature and $a = 2.287 \cdot 10^{-7}[K Pa^{-1}]$ for the glass transition temperature, while Leute (58) determined $a = 3.8 \cdot 10^{-7}[K Pa^{-1}]$ independent of molecular weight. If the transition temperatures depend on pressure in a linear way, one can assume that the crystal growth rate curve, which is related with these, is shifted in the same way. Therefore, the crystal growth rate distribution is shifted to higher temperatures with increasing pressure without changing the shape (eqn. A.6, fig. A.6). Using the factor $a = 5 \cdot 10^{-7}[K Pa^{-1}]$ (table A.11), fitted using the measurements (fig. 4.8), the calculation of the crystal structure (specific volume) is made dependent on the pressure. Results are presented in fig. 4.8 as well. The factor a used is somewhat larger than the values mentioned previously, but is of the same order. This small difference can be due to material characteristics (nucleation and crystal growth rate distribution). It can be concluded accordingly, that the crystallinity dependent model for the specific volume is able to describe the phenomena observed during the experiments. Moreover, modeling the crystallization process accurately, results in accurate predictions for the specific volume.

Influence of cooling rate and pressure:

Using the results from the experiments described above, a numerical study for higher cool-

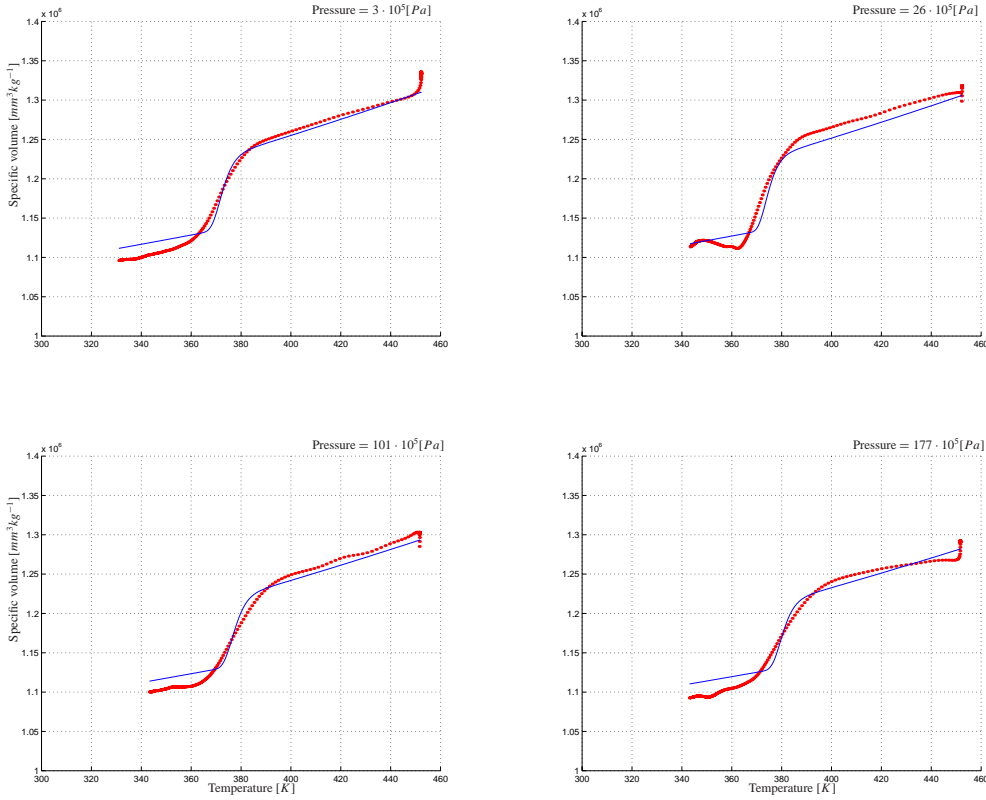


Fig. 4.8: Calculated (—) and measured (•) specific volume as a function of the measured temperature for different pressures ($p = 3 \cdot 10^5, 26 \cdot 10^5, 101 \cdot 10^5$ and $177 \cdot 10^5 [Pa]$) at a cooling rate around $\dot{T}_{max} = 39.52 [K s^{-1}]$.

ing rates and higher pressures can be performed in order to demonstrate the behavior of the modeling in this range. Of course, these results should be considered with some reservation, as they are extrapolations. The specific volume is calculated for a range of pressures ($p = 0.1, 40, 80, 120$ and $160 [MPa]$) and different temperature histories. A starting temperature $T_{start} = 550 [K]$ and an end temperature $T_{end} = 300 [K]$ were applied together with a range of constant cooling rates $\dot{T} = 0.017, 40, 80$ and $120 [K s^{-1}]$.

At a very low cooling rate $\dot{T} = 0.017 [K s^{-1}]$, the calculated specific volume (fig. 4.9, top left) matches the experiments done by Moldflow (fig. A.4). The temperature of the crystallization transition differs from the melting transition in the Molflow data as discussed previously. When the cooling rate is increased to $\dot{T} = 40 [K s^{-1}]$ (fig. 4.9, top right), the crystallization transition is shifted to lower temperatures, although the resulting specific volume at the end temperature remains the same. However, when cooling is increased to $\dot{T} = 80 [K s^{-1}]$ (fig. 4.9, bottom left), the residence time at a temperature which enables crystal growth is that low, that the material does not crystallize fully. As a result, the specific volume at the

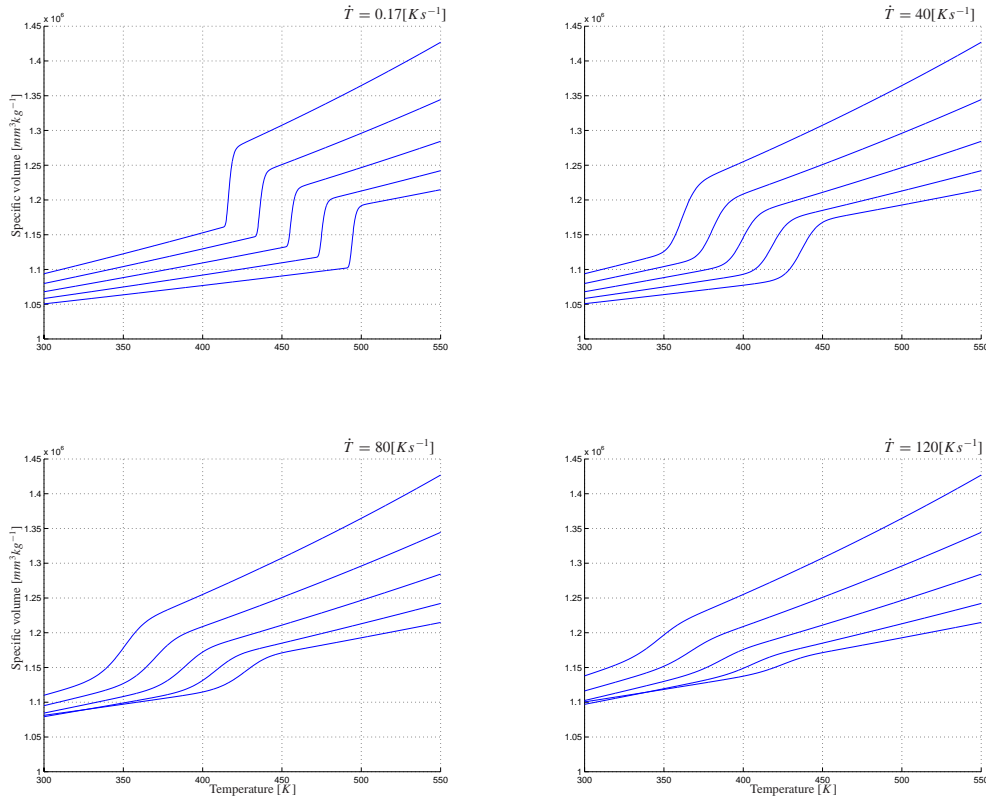


Fig. 4.9: Calculated (—) specific volume for a cooling rate $\dot{T} = 0.017$ (top left), 40 (top right), 80 (bottom left) and $120[K s^{-1}]$ (bottom right). The pressures applied are $p = 0.1, 40, 80, 120$ and $160[MPa]$.

end temperature is higher, because not all material has crystallized in the spherulite form, but partly a mesomorphic phase is present.

Since no information is available on the change of the distribution of the number of crystals with increasing pressure, it is assumed that this distribution stays unchanged. Moreover, it has been shown that increasing the pressure does not fundamentally alter mechanisms of nucleation (He (31)). Consequently, the final degree of crystallinity of the sample will be less at higher pressures. The crossover in fig. 4.9 (bottom left) from a pressure of $p = 120$ to $160[MPa]$ is a result of this. Experimental verification of the number of crystals at different pressures has to be done to confirm this. Increasing the cooling rate to $\dot{T} = 120[K s^{-1}]$ shows the same effect but more pronounced (fig. 4.9, bottom right).

Observations by Piccarolo (69) made clear that increasing the cooling rate from $\dot{T} \approx 0[K s^{-1}]$ to $\dot{T} = 311[K s^{-1}]$ results in a transition from a mainly spherulitical structure to a mainly mesomorphic structure. The model enables us to calculate such a transition (fig. 4.10).

Using the same temperature history as described above, the cooling rate is varied from

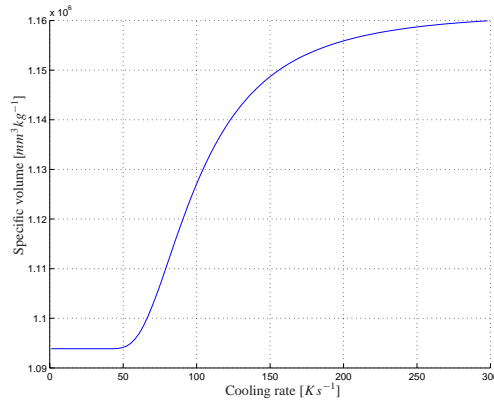


Fig. 4.10: Calculated specific volume for cooling rates up to $\dot{T} = 300[K s^{-1}]$ for the isotactic polypropylene (K2Xmod).

$\dot{T} \approx 0[K s^{-1}]$ to $\dot{T} = 300[K s^{-1}]$ The transition is present around $\dot{T} \approx 50 \leftrightarrow 250[K s^{-1}]$ while the measurements of Piccarolo (69) showed this transition at $\dot{T} \approx 20 \leftrightarrow 80[K s^{-1}]$. The difference probably is caused by the different material characteristics (nuclei and crystal growth rate distribution) of the isotactic polypropylenes used.

4.3 Conclusions

When using standard pVT measurements on semi-crystalline polymers, problems range from no hydrostatic pressures (piston-die technique), low cooling rates (piston-die and confining fluid technique) to an unknown specific volume distribution during cooling (Piccarolo's quenching technique), as expressed in the introduction of this chapter. Therefore, a setup based on the confining fluid technique is developed, that can reach cooling rates of the sample up to $60[K s^{-1}]$ and pressures up to $20 \cdot 10^6[Pa]$. In this way, the specific volume can be measured during cooling at cooling rates comparable with the ones present during the injection moulding process. Comparing measurements using the confining fluid technique in an increasing temperature run, with measurements using the new setup in the isobaric mode show the influence of the procedure used on the specific volume of a semi-crystalline polymer. The confining fluid technique results in a melting transition around approximately $T = 430[K]$, while measurements with the new setup show a crystallization transition around $T = 370[K]$. This difference consists of the influence of the cooling rate on the crystallization kinetics together with the difference between melting and crystallization, also known from DSC experiments. The influence of the pressure on the crystal growth rate distribution is determined by measuring the specific volume at a constant cooling rate at pressures up to $p = 177 \cdot 10^5[Pa]$. Besides a normal shift to a lower specific volume at a higher pressure, an extra shift in the crystallization transition temperature is present. Modeling the specific

volume is done by combining a set of equations that fully describe the crystal structure during an experimental run, with a Taylor series in pressure and temperature. This combination accurately describes the specific volume measured at cooling rates of $\dot{T} = 0.21[K s^{-1}]$ and $\dot{T} = 33.96[K s^{-1}]$, while at cooling rates of $\dot{T} = 44.58[K s^{-1}]$ and $\dot{T} = 54.22[K s^{-1}]$ there is a little difference. This difference might be caused by a different crystal structure at these cooling rates, which results in a different crystal growth rate distribution.

In conclusion, the new setup enables measurements of the specific volume at injection moulding conditions. Moreover, results at low cooling rates are in accordance with results presented by Ito (36), Moldflow (61) and Zoller (90), results at elevated pressures are in accordance with results presented by He (31), Ito (38) and Leute (58) and results at high cooling rates show a resemblance with the work of Piccarolo (69). The results moreover stress that standard techniques are not able to characterize the specific volume of semi-crystalline polymers. Therefore, crystallization kinetics in the sample have to be known in order to get detailed information on the specific volume for semi-crystalline polymers. An experimental-numerical approach seems inevitable. On the one hand, modeling the crystallization process accurately, results in accurate predictions for the specific volume. On the other hand, measuring the specific volume at a range of cooling rates and pressures, gives a first impression of the crystallization kinetics in the material. These experiments will be extended to higher pressures and cooling rates, while the influence of flow will be studied by using different kind of experiments (Swartjes (79)) and modeling (Zuidema (94)).

Chapter 5

Injection moulding

The modeling aspects presented in the previous chapters, contribute to the framework that is needed to predict the final properties of injection moulded products. However, this framework is certainly not complete. For example, oriented crystalline structures will cause anisotropic shrinkage, of which almost nothing is known yet. Therefore, the relation between the experimental and numerical results on shrinkage, presented in this chapter, can only be qualitative. We will focus on the most important trends with varying processing conditions, and show that they correlate with predicted oriented structures. Such a comparison indicates on how to fill the gap in the theoretical framework and which experiments have to be performed in the future. Especially with regards to experiments on injection moulding, still a lot has to be improved. For many past experiments, initial and boundary conditions are not recorded precisely enough, and thus these experiments are not very useful for validation.

Experiments have been performed to determine the main parameters, that influence the resulting structure distribution, i.e. the thickness of the flow-induced oriented layer (section 5.1). Numerical results are presented in section 5.2. Subsequently, in section 5.3 the implications of these results for the prediction of dimensional stability will be discussed. The influence of the flow history on the resulting structure is demonstrated by simulating the SCORIM process, a ‘push-pull’ moulding process where, after the mould has been filled, the flow is kept in a backwards and forwards motion (subsection 5.3.2).

5.1 *Experimental analysis*

An experimental study has been performed on the influence of different processing conditions on the distribution of the oriented layers in the final (injection moulded) product, and the accompanying dimensional stability. In subsection 5.1.1, the experiments performed are described and in subsection 5.1.2, the results are presented.

5.1.1 *Experimental description*

Experiments were performed at Borealis in Linz to study the influence of processing conditions on the resulting morphology in the product and the dimensional stability of the product. Using polypropylene K2Xmod (appendix A.3), a rectangular strip (length $l = 150 \cdot 10^{-3}[m]$, width $w = 80 \cdot 10^{-3}[m]$ and thickness $d = 2 \cdot 10^{-3}[m]$) with a line gate entrance region (see fig. 5.1) has been injection moulded. Variations in the temperature of the melt injected, the volume flux during filling and the temperature of the mould wall are used. The different pro-

cessing conditions applied represented the limiting values possible on the machine, in order to create examples that show maximum differences. After moulding, the strips were stored

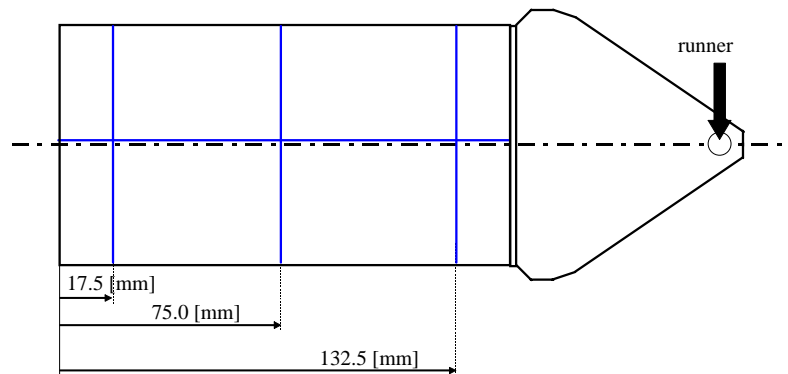


Fig. 5.1: The mould used for the injection moulding experiments. The positions for the shrinkage measurements (—) are shown.

at a temperature of $T = 296[K]$ and a humidity of 65%. On different time intervals during a period of 220 days, starting one hour after actual moulding, the longitudinal shrinkage of the product was measured at one position, and the width shrinkage at three (see fig. 5.1). The morphology was studied using polarized light microscopy on microtome cuts parallel to the flow direction, at the same positions as those for the shrinkage measurements (see fig. 5.1). These microscopy measurements were carried out at Linz University (Austria) in the group of prof. Eder. Density and mechanical properties measurements on these strips (Gahleitner (24)) will not be discussed here.

5.1.2 Experimental results

Shrinkage shows semi-logarithmic behavior in time, which is observed for other (semi-crystalline) polymers as well (Fiebig (21)). The amount and rate of shrinkage differ dependent on the position along the flow path. These differences are related to the crystalline structures formed during processing, and they demonstrate that the processing conditions can have a significant influence on the final shape of the product. Since shrinkage in the width is measured at three positions along the flow path, together with longitudinal shrinkage, the influence of processing conditions can be related to the shape of the final product. All experimental results can be found in appendix B. The global (exaggerated) product shapes, as obtained 220 days after moulding, are presented in fig. 5.2. Comparing the left column (low flux during filling) with the right one (high flux), shows that with increasing volume flux, both the longitudinal and the width shrinkage decrease for all experiments. Comparing experiments for a high mould wall temperature (upper part) with that of the lower temperature (lower part) shows that changing the temperature of the mould wall does not have a great influence on the dimensional stability in absolute sense, although for high injection temperatures ‘mirrored’ shapes are found. The temperature of the melt injected is highest for the experiments in the first and third row. Decreasing the temperature of the melt, increases the

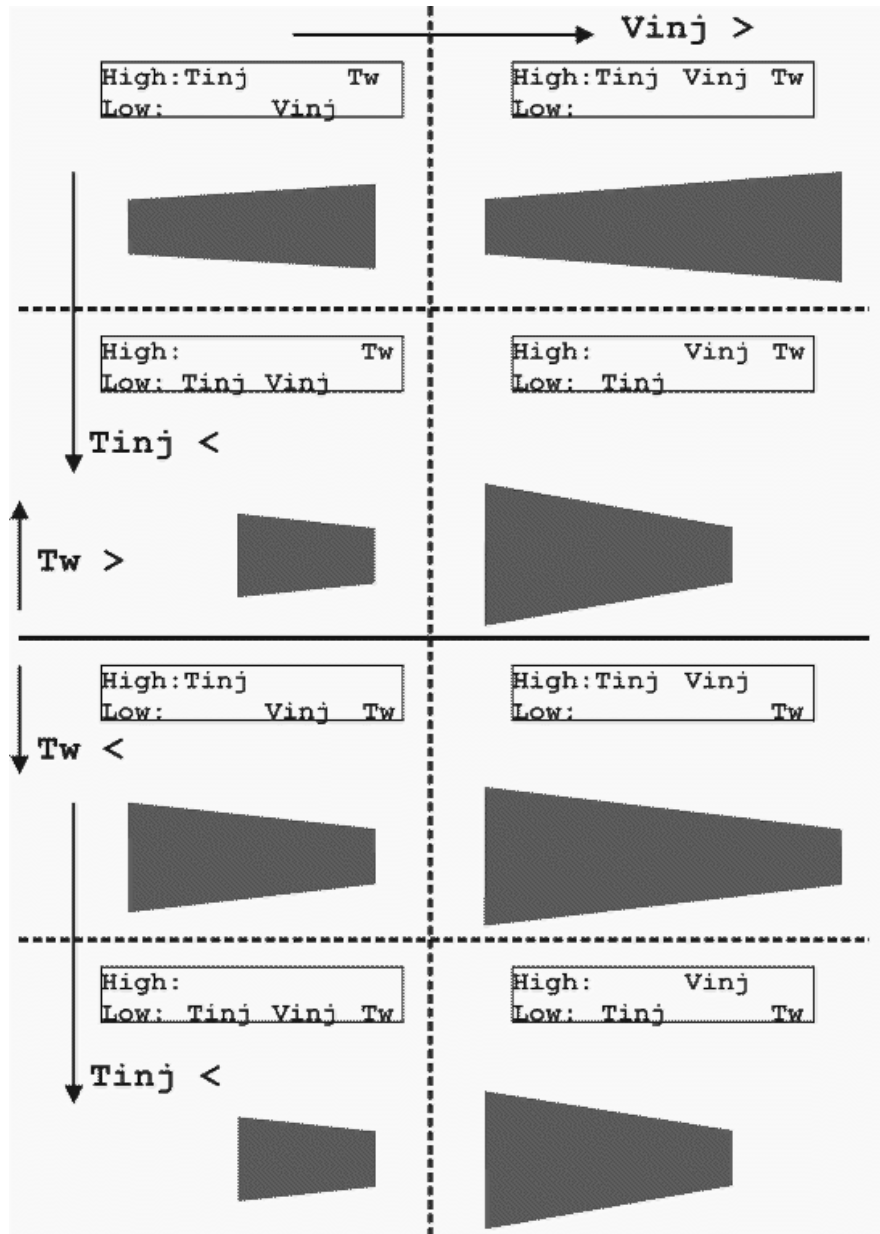


Fig. 5.2: Representation of the products shape, 220 days after injection moulding a rectangular strip, for the different processing conditions (absolute shrinkage values range from 1.2% at minimum to 1.9% at maximum, see fig. 5.6 and appendix B).

longitudinal shrinkage, while the width shrinkage is not effected consistently.

Due to the nucleation agent present, the material did not show a variation in the fine spherulitical core morphology. Therefore, all attention is focused on the flow-induced oriented layer. The thickness of this layer is determined using polarized light microscopy measurements (see for example fig. 5.3, where the oriented layer is present like a white band at the products surface), which procedure resembles the one used by Eder (18) and Jerschow (43). In this way, the transition position from the oriented material to the mainly unoriented mate-

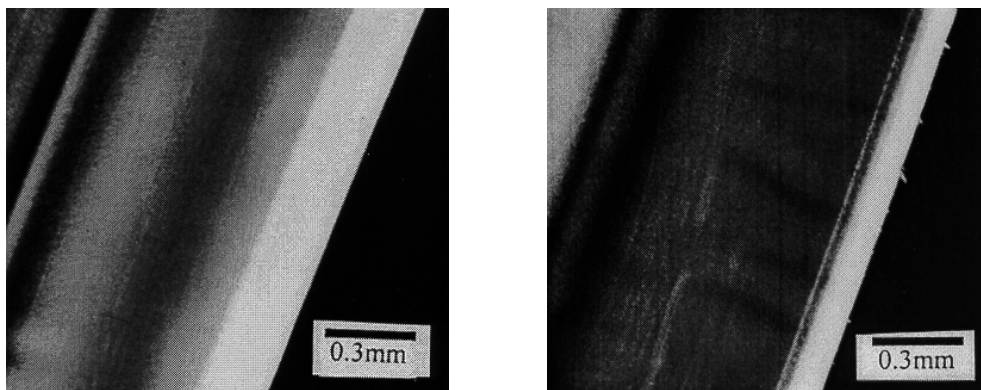


Fig. 5.3: An example of the (flow-induced) oriented layer distribution close to the gate (left) and far from the gate (right). The flow-induced oriented layer appears as the white band, at the products surface.

rial is determined, but the distribution of the amount of oriented material across the thickness remains unclear. Notice the considerably thinner layer thickness at the end of the mould, where at the wall material is present that has been supplied through the core of the flow and, thus, has experienced less deformation. In fig. 5.4, the dimensionless thickness of the flow-induced oriented layer is shown along the flow path for different experimental processing conditions and for the lower (left) and higher (right) mould wall temperature. Trends for different processing conditions are apparent. A higher melt temperature as well as a higher volume flux during filling decrease the thickness of the flow-induced oriented layer, while the mould wall temperature shows no significant influence.

Using the shrinkage and flow-induced layer thickness measurements, the anisotropy has been determined as a function of the layer thickness (the anisotropy is defined as the shrinkage in longitudinal direction over the shrinkage in width direction). In fig. 5.5 the anisotropy is shown for all experiments, at all three width positions along the strip (black symbols: near the gate; white symbols: far from the gate, and gray symbols: in between) as a function of the measured thickness of the oriented layer at the corresponding position. Anisotropy clearly correlates with the thickness of the flow-induced oriented layer, although the points corresponding to the end of the mould lay somewhat 'off line'. Since the material, present at the end of the mould, only experienced a thermo-mechanical history during transport through

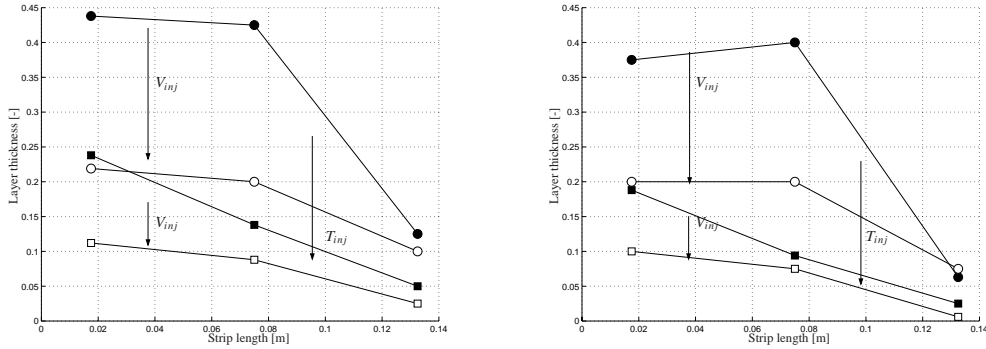


Fig. 5.4: The measured dimensionless thickness of the flow-induced oriented layer along the flow path. The entrance to the strip is located at the left side. Results are presented for a low (circles) and high (squares) temperature of the melt injected, and for low (filled symbols) and high (open symbols) volume fluxes during filling. At the left the results are presented for the lower mould wall temperature, at the right for the higher one.

the core of the cavity (and the elongational strain at the flow front), the anisotropic behavior can differ. When no flow-induced oriented layer is present, as in quiescent crystallization, the orientation of lamellae in the spherulites is random, and the material is expected to be isotropic. However, the material shows (measured) isotropic behavior (anisotropy equals 1) for a thickness of the flow-induced oriented layer of approximately $\delta = 400[\mu\text{m}]$ (40% of the thickness), see fig. 5.5. A problem here could be that (because of lack of data) the longitudinal shrinkage was assumed to be uniform along the flow path, while it has been shown by Jansen (42), that longitudinal shrinkage shows variations along the flow-path. These variations were shown to depend most strongly on the mould wall temperature and holding pressure and the longitudinal shrinkage was largest at the central position along the flow path in the cavity. As a result, taken these aspects into account, the data of fig. 5.5 would rearrange, but the physical explanation for these observations still would not be clear.

Apart from relating the thickness of the flow-induced oriented layer with the anisotropy, it could be investigated whether a relation with the actual shrinkage exists (see fig 5.6). For all experiments performed, the shrinkage measured after 220 days at all positions in the width direction, is shown as a function of the measured local thickness of the flow-induced oriented layer. Since the results close to the gate are influenced by the transient character of the flow of polymer entering the mould, and the results far from the gate by the fountain flow, these are separated from the results at the central position. It can be concluded, that shrinkage does not correlate with the thickness of the flow-induced oriented layer. As stated before, when using optical microscopy measurements to determine the thickness of the flow-induced oriented layer, only the position is found where the amount of oriented material is that low, that a fading of the oriented structure is observed, while the distribution across the thickness remains unclear. Since all unoriented and oriented material has its influence on the shrinkage (and not only the part present in the observed layers for which also the content is not known),

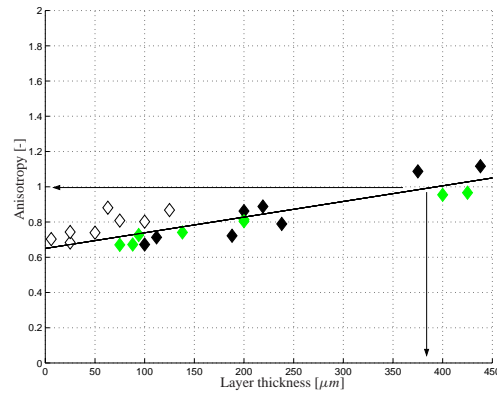


Fig. 5.5: The measured anisotropy as a function of the measured thickness of the flow-induced oriented layer for all experiments, at all three width positions along the strip (black symbols: near the gate; white symbols: far from the gate; gray symbols: in between and, the line is to guide the eye).

this can be a reason for the lack of correlation in fig 5.6.

The experimental trends, presented in this section, will be analyzed qualitatively in section 5.2, using numerical simulations.

5.2 Numerical analysis

5.2.1 Introduction

The absence of shear in the center of injection moulded products results in a spherulitical structure, while in the highly strained regions at the cavity walls an oriented structure can be present (fig. 1.1). The structure is the result of the thermo-mechanical history experienced by the material and, therefore, accurate modeling of this distribution should also include (at least) a calculation of the flow in the runner system. Since no information is available about the geometry of the runner system of the machine used for the experiments presented in section 5.1.2 and its thermal properties, only flow in the cavity is included in the simulations. Moreover, the elongational strain, experienced by the material in the flow front region, is not dealt with (see section 2.2). As a result, the structure distribution will not match the corresponding experimental results and only the influence of the different processing conditions can be studied and trends may be captured. In order to study these trends, i.e. the changes in the thickness of the flow-induced oriented layer depending on differences in the processing conditions, criteria have to be formulated for the position of the interface between the oriented and unoriented material. In subsection 5.2.2, different possibilities are enumerated and one will be selected.

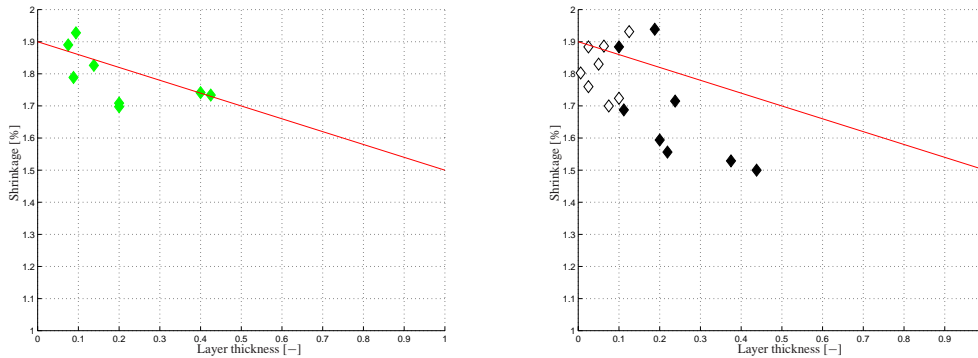


Fig. 5.6: The measured width shrinkage after 220 days at different positions of the strip, as a function of the measured thickness of the flow-induced oriented layer. At the left side the gray symbols show the results at the central position and the line is to guide the eye for these results. At the right the black symbols show the results near the gate; the white symbols far from the gate, while the line is the indication for the results at the central position.

5.2.2 Choice of criteria

The injection moulding cycle is studied using the methods discussed in chapter 2. The structure distribution is calculated using the S_{J2} -model for the flow-induced crystalline structures (eqn. 3.7) and Schneider's rate equations for the spherulitical crystalline structures (eqn. 3.1). Since both models fully describe the resulting structure after processing, the structure distribution across the thickness of the mould can be visualized. In fig. 5.7 an example is given. This complete description of the structure distribution can be used to determine the position

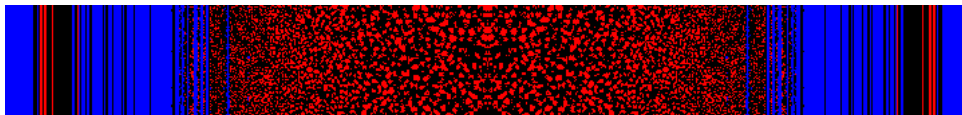


Fig. 5.7: Example of the structure distribution across the thickness of the mould, after processing. Oriented structures, close to the mould wall are represented by lines, while the spherulitical structures, present towards the center of the mould, are represented by the 'circular' areas. The interfaces between all structures are marked black (compare fig. 3.5, fig. 3.10, and fig. 4.6).

of the interface between the oriented material at the cavity wall and the unoriented material at the core. As presented in chapter 3, this interface can be characterized by a value for the time integral of the second invariant of the recoverable strain of $\approx 2.0 \cdot 10^5[-]$ for the startup flow experiments, as shown in fig. 3.8, and $\approx 1.2 \cdot 10^5[-]$ for the steady state flow experiments, as shown in fig. 3.9. From these results it is clear that, the time integral of the second invariant of the recoverable strain tensor tends to a constant value at the layer boundary. However, its value differs, probably due to the (not modeled) influence of the flow in the extruder and the entrance region to the duct, as expressed in chapter 3. Also the dependence of the maximum

rheological relaxation time θ_1 on the number of flow-induced nuclei (eqn. 3.8), will change the value for the time integral of the second invariant of the recoverable strain. Moreover, the experiments described in chapter 3, all are performed at a constant temperature across the duct. The only mutual difference is the flow treatment applied. As a result, the difference between the structures created consists of a difference in amount of shish created, because the over-growth of kebabs on these shish is the same in both cases since that is determined by the temperature of the melt. Consequently, at the interfaces, visualized using polarized light microscopy, not only the volume fraction oriented material is constant, but also the total length of the shish. In injection moulding, the complex thermo-mechanical history results in a complex distribution of the morphology in the sample. Along the interface between the oriented and unoriented material, observed using polarized light microscopy, the morphology therefore does not have to be the same in all aspects (i.e. shish length and kebab volume), like in the startup flow experiments at a particular temperature. For example, dependent on the number of shish created and the local temperature of the melt, the over-growth of kebabs can differ, though the amount of oriented material can be the same. As a result the amount of oriented material does not necessarily correlate anymore with the total length of the shish created. Consequently, the criterion used for the startup flow experiments can not directly be used for the morphological study in injection moulding.

Since a complete description of the structure is available from the numerical simulations, other criteria can be chosen. As an example, using a simulation for the complete injection moulding cycle [from the filling stage, followed by ‘packing’ and ‘holding’ (for which the pVT model is used), up to ‘ejection’, of a rectangular strip with the following dimensions: length $l = 155 \cdot 10^{-3}[m]$, width $w = 20 \cdot 10^{-3}[m]$ and thickness $d = 3 \cdot 10^{-3}[m]$ using the processing conditions as stated in table 5.1], the structure distribution can be calculated and shown in fig. 5.8 for three positions across the duct.

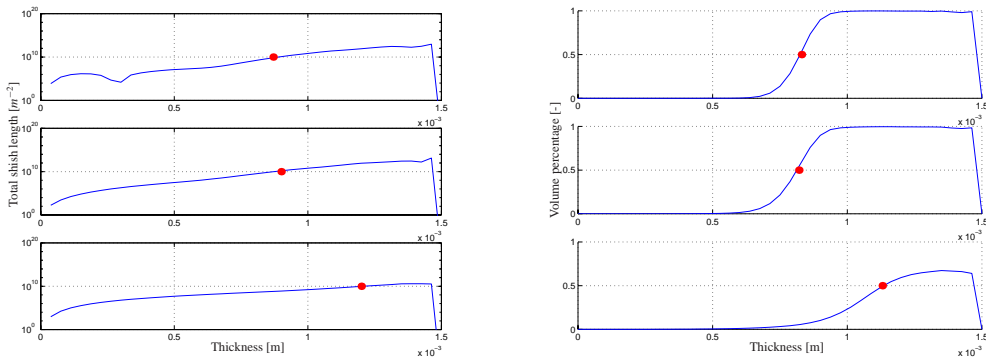


Fig. 5.8: The distribution of the flow-induced oriented structure across the thickness of the injection moulded product close to the gate (top), far from the gate (bottom) and in between (middle), for the processing conditions as shown in table 5.1. At the left side the total shish-length is shown, at the right side the volume percentage oriented material.

| no. | T_{inj} [K] | Q [$m^3 s^{-1}$] | T_w [K] |
|-----|---------------|----------------------|-----------|
| 1 | 480 | $4.65 \cdot 10^{-4}$ | 333 |

Tab. 5.1: Numerical processing conditions as applied to study the influence of these conditions on the structure distribution and accompanying shrinkage, in which T_{inj} is the temperature of the melt injected, Q the volume flux during filling and T_w the temperature of the mould wall.

The distribution of the total shish length (fig. 5.8, left side) along the flow path of the polymer (top: close to the gate; middle: central, and bottom: far from the gate) across the thickness of the duct, shows two important variations. First, the total shish length decreases with increasing distance from the gate, because the material that has been supplied there through the core of the flow, has experienced less deformation (this is most clear going from the central position to the end of the duct). Second, under the influence of the holding pressure applied, polymer is entering the mould to compensate for the shrinkage of the polymer in the rest of the duct. Since the flow in the holding stage occurs at a continuously lowering temperature, this (slow) flow can still cause considerable orientation, see Caspers (9), and thus will induce nucleation and crystallization. Flow during ‘holding’ is most pronounced at the entrance of the mould and, therefore, locally increases the total length of the shish (fig. 5.8, left side, top). With increasing holding pressure, the stronger holding flow creates more shish towards the core of the strip.

For the same positions across the duct, at the right side of fig. 5.8, the calculated volume fraction of oriented material is presented. Also in these results, the volume fraction of oriented material decreases with increasing distance from the gate, which is comparable with the observation for the distribution of the total shish length. However, only the shish closest to the wall give pronounced amounts of oriented material and the influence of the holding pressure is not present here, since the shish, created towards the center of the duct, did not grow out to a considerable amount of oriented material due the local thermal history.

Thus, different possibilities for criteria to determine the position of the interface between the oriented and unoriented material result from the numerically determined structural properties. As was calculated by Eder et al. (18), the total shish length at the interface observed in their startup flow experiments equals $L_{tot} = 6.3 \cdot 10^{10} [m^{-2}]$ (see chapter 3). Applying his criterion, the thickness of the oriented layer is indicated in fig. 5.8 (left side) with dots, and the total layer is shown at the left side of fig. 5.9. Another possibility is to assume the interface to be present at the position across the thickness of the duct, where the volume fraction of oriented material equals 50% (see fig. 5.9, right side). Both results in fig. 5.9 show a similar thickness profile along the flow path. Since the slope of volume changes versus position in thickness is steep and, thus, the position of the transition will not change much over a wide range of fractions (5 – 95%), compared to the slope and range for the total shish length ($0 \approx 1 \cdot 10^{20}$), the first criterion is less sensitive. Therefore, the position of the interface between the oriented and unoriented material is defined by choosing a constant value (50%) for the volume percentage oriented material. In case of multiple layers of oriented material, the thickness of the flow-induced oriented material is determined using the layer closest to the core since, using optical microscopy, the different layers hardly can be

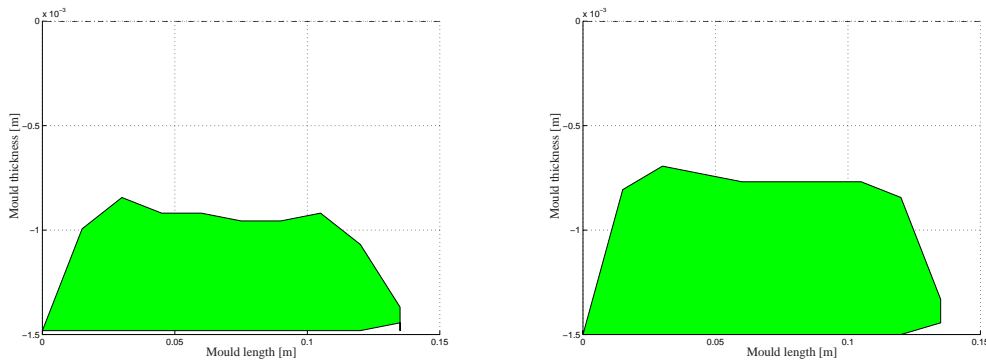


Fig. 5.9: Numerically determined flow-induced oriented layer along the flow path of the polymer melt (processing conditions used are presented in table 5.1). At the left the thickness is determined using the total shish length, at the right using the 50% oriented material.

distinguished. In the next subsection, the influence of different processing conditions on the thickness (-distribution) of the oriented material will be studied, using numerical simulations.

5.2.3 Morphological sensitivity due to processing conditions

In subsection 5.2.2, a simulation has been elucidated for the complete injection moulding cycle, from the filling stage, followed by ‘packing’ and ‘holding’, up to ‘ejection’. In fig. 5.9 a characterization of the thickness of the flow-induced oriented layer, calculated using the processing conditions from table 5.1, is shown along the flow path of the polymer. The thickness of the oriented layer shows a sharp increase at the gate, followed by a small decrease with increasing distance from the gate. This entrance behavior has also been observed by Eder (20) (see fig. 3.3). Further along the flow path, the thickness of the oriented layer becomes nearly constant. At the end of the mould, it decreases towards zero and moreover moves away from the mould wall. The flow in the holding stage takes place at a lower temperature than during filling. Consequently, this flow can still cause considerable orientation, see Caspers (9), and thus flow-induced nucleation and crystallization. Flow during ‘holding’ is most strong at the entrance of the mould and locally increases the thickness of the flow-induced oriented layer. Material, which ends up at the mould wall, has experienced the fountain flow at the flow front. Before reaching the front, it has hardly experienced any deformation in the core of the mould. As a result, with increasing distance from the gate, the amount of oriented material will decrease, and so will the thickness of the flow-induced oriented layer. This has been observed in the experiments as well (fig 5.3).

Numerical simulations were performed using similar, though not the same, variation in the processing conditions as used in the experiments (see section 5.1). Only the temperature of the mould wall matches the experimental values used. The experimental conditions applied were rather extreme, and it turned out that the high flux applied in the experiments could not be simulated, since during analyzing the injection stage, numerical instabilities

occurred. Also, a too large difference between the mould wall temperature and the temperature of the melt injected, caused the (decoupled) strain calculation to become numerically unstable. Therefore, the volume flux during filling, and the temperature of the melt injected are chosen lower than the ones used in the experiments. The position of the interface between the unoriented spherulitical core and the oriented material (and thus the thickness of the flow-induced oriented layer) is, as stated above, defined by choosing a constant value for the volume percentage oriented material (50%). The lower injection temperature and speed, used in the numerical simulations, will cause an overall increase in the thickness of the flow-induced oriented layer as compared to the experiments. Therefore, only the trends present in the numerical simulations, could be compared with the trends present in the experimental results. In fig. 5.10, the thickness of the flow-induced oriented layer is presented for the different processing conditions applied. The absence of the runner causes the material to show

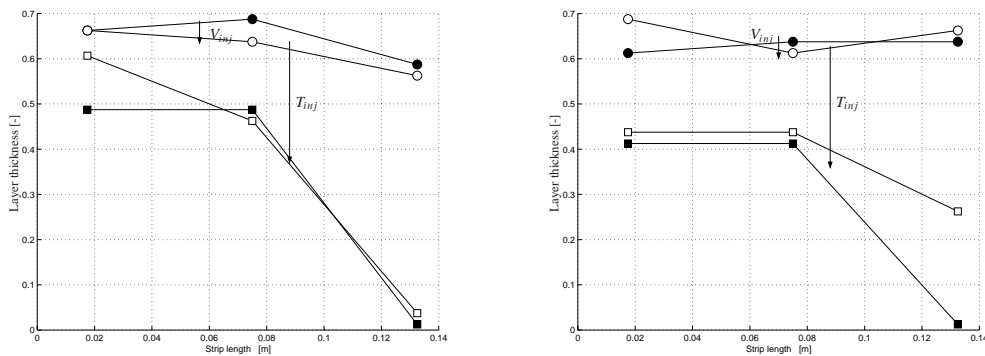


Fig. 5.10: Numerically determined dimensionless thickness of the flow-induced oriented layer along the flow path. The entrance to the strip is located at the left side. Results are presented for a low (circles) and high (squares) temperature of the melt injected, and for low (filled symbols) and high (open symbols) volume fluxes during filling. At the left the results are presented for the lower mould wall temperature, at the right for the higher one. Compare with fig. 5.4.

startup behavior when entering the mould, this in contrast with the experiments, compare with fig. 5.4. As a result, at the position close to the entrance of the strip, the numerical results are not comparable with the experimental results. The general trend in the numerical results is: a higher melt temperature results in a decrease of the thickness of the flow-induced oriented layer, just as found in the experiments. The influence of the injection speed is, though, not present. A probable reason for this is again the absence of the flow in the runner system in the numerical simulations.

The complete description of the morphological distribution, dependent on the processing conditions and flow in the cavity, might result in the ability to correlate measured shrinkage with characteristics of the morphology if the numerical processing conditions match with the experimental ones. Since this is not the case due to reasons discussed before, only an indication can be given for such a correlation. Comparable with the experimental correlation sought in fig 5.6, where the actual measured shrinkage was correlated with the thickness of

the flow-induced oriented layer, in fig. 5.11 the actual measured shrinkage is correlated with the mean volume percentage oriented material across the thickness of the duct. As stated

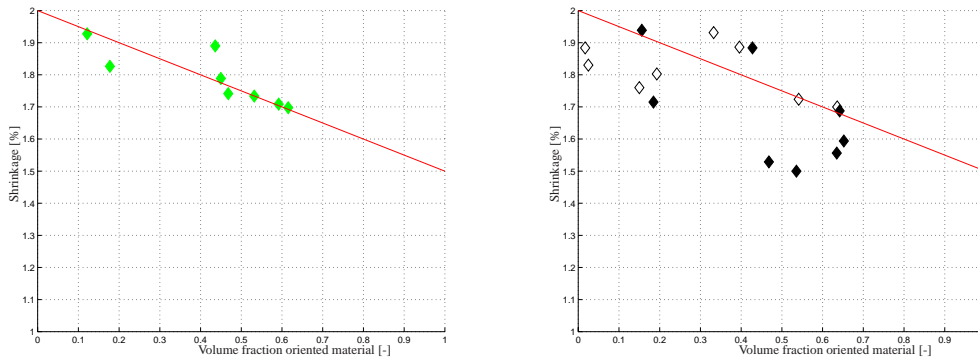


Fig. 5.11: The measured shrinkage after 220 days, at all positions in the width direction, as a function of the calculated mean volume fraction oriented material across the thickness. At the left side the gray symbols show the results at the central position and the line is to guide the eye for these results. At the right the black symbols show the results near the gate; the white symbols far from the gate, while the line is the indication for the results at the central position. Compare with fig. 5.6.

in subsection 5.1.2, when using optical microscopy to determine the thickness of the flow-induced oriented layer, the distribution across the thickness of the oriented material remains unclear. Since all (un)oriented material present contributes to the actual shrinkage, it does make sense to correlate the, local, over the thickness averaged, volume fraction oriented material with the shrinkage. When doing so (fig. 5.11), a (better) correlation seems to be present (compared with fig. 5.6, left) for the data at the central position (left hand side). Although the correlation is still weak, even the other data (right hand side) do show a better correlation than using experimental layer thicknesses. However, it is clear that experimental and numerical conditions should match first, to be able to make more founded statements.

5.3 Discussion on dimensional stability

5.3.1 Towards an accurate model evaluation

When the structure distribution in an injection moulded product can be predicted and the time dependent shrinkage behavior of both the spherulitical and oriented structures would be known, dimensional stability predictions will become possible. By combining the relative, local, presence of both phases with their individual shrinkage behavior, the relation between shrinkage and structure (-distribution) can be studied. Then, a numerical dimensional stability analysis could be performed, in dependence of the processing conditions, like in fig. 5.2. The lack of data concerning the (anisotropic) shrinkage behavior of both the spherulitical and flow-induced structures, disables the usage of the predicted structure distribution for dimensional stability analysis and only trends, like in fig 5.5 and fig. 5.6 between global properties:

layer thickness, density, moduli and dimensional stability can be shown (Gahleitner (24)).

To solve this problem, well defined experiments are needed in combination with the modeling used here, which has the advantage that it completely describes all characteristics of the structure (contrary to other flow-induced crystallization models from Bushman (8), McHugh (12), Guo (29), Isayev (35), Ito (37), Nakamura (66), see chapter 3). A good candidate for such experiments is the SCORIM process. This process is suited to create extreme situations in the injection moulding process. Nearly fully oriented samples can be made, which can be used for studying the anisotropic shrinkage behavior. In this way, this process can be applied to separately characterize the (anisotropic) shrinkage behavior of both the spherulitical and oriented structures and, therefore, it will be discussed in the next subsection.

5.3.2 The SCORIM process

In the SCORIM process, the flow is kept in motion after the mould has been filled, during solidification/crystallization of the polymer (Kalay (46)). A continuous flow in the mould will increase the degree of orientation. A stratified crystalline structure over nearly the full thickness of the cavity can be the result of such a treatment (see an example of SCORIM in fig. 5.12). Comparison of the experimentally determined layered structure (position and

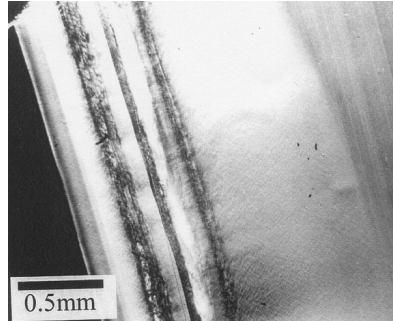


Fig. 5.12: An example of the resulting layered structure over half the thickness of the sample after the SCORIM process. After (47).

thickness of such layers), with predictions using the (flow-induced) crystallization kinetics modeling (chapter 3) does not only help to resolve the anisotropic shrinkage problem, but also can serve as a perfect benchmark problem for the (flow-induced) crystallization models used. As a numerical example, a rectangular duct (with dimensions: length $l = 120 \cdot 10^{-3}[m]$, width $w = 8 \cdot 10^{-3}[m]$ and thickness $d = 3 \cdot 10^{-3}[m]$) is filled with polypropylene K2Xmod (see appendix A.3) at a melt and wall temperature $T = 473[K]$ and history is removed by applying a waiting period (at the end of the waiting period the time is set to $t = 0.0[s]$). Next, a temperature history is created across the thickness of the mould by lowering the wall temperature to $T_w = 333[K]$. Flow is enabled from $t = 1.0[s]$ until $t = 1.5[s]$ with a flux of $Q = 2.4 \cdot 10^{-6}[m^3s^{-1}]$ and from $t = 9.5[s]$ until $t = 10.0[s]$ with the same flux in

the same direction. The calculated structural data are used to visualize the structure development during crystallization (fig. 5.13). The flow procedure creates two clearly separated

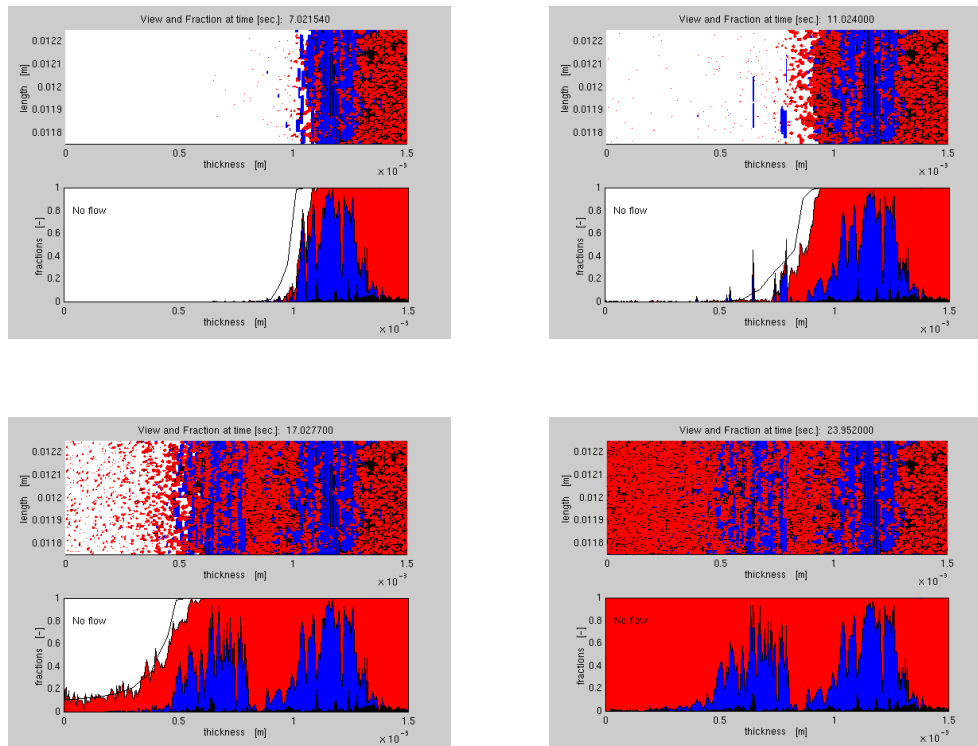


Fig. 5.13: Visualization of the structure from the center of the plate (thickness = 0 [m]) to the surface (thickness = 0.015 [m]) for different moments during crystallization (upper parts), together with the local and global degree of crystallinity (lower parts; compare fig. 3.5, fig. 3.10, and fig. 4.6).

layers in half of the thickness. Because a nucleation agent is present in this material, the number of spherulites is spatially uniform, and the cooling rate has no influence on the number of spherulites. The spherulitical growth, which depends on the temperature, is the only difference in spherulitical crystallization kinetics. Therefore, only the time scale in which crystallization occurs is different across the duct.

Since it is possible to calculate the structure distribution in any product, the SCORIM process can be used to validate models for (flow-induced) crystallization. Moreover, the structure distribution in fully oriented samples can be used to study the effect of oriented material on time dependent (anisotropic) shrinkage behavior.

5.4 Conclusion

When numerical simulations are used to analyze the experimental results, the most important restriction is that the boundary conditions in both the experimental and numerical results should be the same. For the results presented in this chapter, this is not the case due to unexpected shortcomings in the VIP modeling that expressed themselves as the occurrence of two different type of numerical instabilities. Therefore, the VIP modeling should be made numerically more stable, for example by using different types of elements for the calculation of the recoverable strain.

The complete description of the structure distribution resulting from the different processing conditions can be compared with experimental results, for instance using the SCORIM process. However, instead of using optical microscopy to analyze the layered structures in the product, different techniques like WAXD and SAXS should be used. Then the experimental characterization of the structure can catch up with different aspects of the numerical characterization, like the amount of oriented material or the shish length. In that way, the numerical characterization of the structure is the most beneficial.

The correlation sought between the experimentally obtained shrinkage and the numerically obtained characteristics of the structure can only be indicative for trends, since the boundary conditions were not the same. When the time dependent (anisotropic) shrinkage behavior of both the spherulitical and oriented crystallized material is known, predictions of the shrinkage of products, using the structure distribution calculated, come within reach. The SCORIM process, principally, represents an optimum possibility to extend the modeling, in the sense mentioned above, but, moreover, to validate models (and criteria used in these models) by using layer positions and thicknesses over the mould thickness, as easily identifiable criteria.

In conclusion, the framework presented in this chapter that is needed to predict the final properties of injection moulded products, is certainly not complete. The gaps present are (i) the unknown (anisotropic) shrinkage behavior of both the spherulitical and oriented crystallized material, and (ii) the absence of a method to characterize experimentally observed morphologies comparable with the numerical characterization. Filling these important gaps will contribute to the framework needed to predict dimensional stability.

Chapter 6

Discussion and conclusions

6.1 Crystallization

A distinction has been made between structure formation resulting from unoriented material (the spherulites) and that from oriented material (often called shish-kebabs). By doing so, different crystal structures are neglected. At the mould walls, trans-crystalline structures can be present resulting from nucleation at the mould walls. For the material considered (iPP), the two types of structures both belong to the α -phase, and, as a result, other possible crystalline conformations like the γ - and β -phase are not taken into account. Material which has not been captured by spherulites or by shish-kebabs is assumed to be present in the mesomorphic phase. These assumptions are reasonable and necessary for two reasons. (i) Most of the crystalline structure present, will show an α -phase, since this is the physically most stable one. The other phases only appear at specific processing conditions. (ii) Data concerning nucleation and growth rate are available for the α -phase crystals. For the other crystals this information is hardly available, since their appearance is rare. Nevertheless, once data become available, they can easily be taken into account in the modeling used.

6.2 Modeling

In most experiments modeled, like the startup flow experiments, the runner system does not have an influence on the structure distribution. In contrast, for the injection moulding simulations an influence by the runner is present. We focused on the phenomena present in the mould. Consequently, for the injection moulding process, the structures predicted will not match the experimentally observed ones, although the general trends resulting from differences in the processing conditions still will be present. The assumption for the modeling of the flow front region, discussed in section 2, results in the absence of the very thin layer of material, oriented by the elongational flow at the flow front. This assumption only results in a small difference between the structure resulting from the simulations and the experiments of the injection moulding process near the mould wall. Because only the thickness of the flow-induced oriented layer has been studied, the small elongational oriented layer is, automatically, included. The only difference observed is, that the flow-induced oriented layer is not connected with the mould wall. Still, it is possible to include the elongational flow at the flow front. More important, however, is to include the runner system in the analysis and to remove the, unexpected, shortcomings in the VIp modeling that expressed themselves as the occurrence of two different type of numerical instabilities.

6.3 Flow-induced crystallization modeling

Starting with the Eder model for flow-induced crystallization, which is based on the shear rate as the driving force for creating structures, a new model to describe flow-induced crystallization, based on the molecular orientation, has been proposed. In this way the process parameter ‘shear rate’ has been replaced by the material state parameter ‘recoverable strain’, equivalent with the viscoelastic stress. For very different thermo-mechanical histories, like isothermal flows with different shear rates, shear times and in steady flows, a strong correlation is found between the experimentally determined position of these layers and the ones predicted by the new model that is based on the most simple functional (the integral in time) of the second invariant of the deviatoric part of the recoverable strain for the maximum rheological relaxation time. The evolution of the recoverable strain is described using the Leonov model, which gives a reasonably good description in shear flows. However different models, for example the Giesekus, the Phan-Thien Tanner, or (modified) POM-POM models (Verbeeten (84)), can easily be implemented when more complex flows have to be studied. Since the Eder model has the important feature of including all the properties that characterize the structure, we kept that structure present when reformulating it. The proposed formulation serves as a starting point for further validation, using different experiments and, if necessary, further adaptations of the model can be made. The main difference between both models is the ability of the S_{J2} -model to predict the influence of the molecular weight distribution, that can be measured via *independent*, rheological, experiments.

6.4 pVT experiments

Since different problems occur using standard pVT measurements, like the absence of a uniform hydrostatic pressures for the piston-die technique, low cooling rates for both the piston-die and the confining fluid technique, and an unknown specific volume distribution during cooling with Piccarolo’s quenching technique, a setup based on the confining fluid technique has been developed, that can reach cooling rates of the sample up to $60[K s^{-1}]$ and pressures up to $20 \cdot 10^6[Pa]$. In this way, the specific volume has been measured during cooling, at cooling rates comparable with the ones present in the injection moulding process. This is important since the cooling rate showed to have a large influence on the specific volume. The combination of the experimental procedure used with the continuous structure formation in the material, has shown to have a large influence on the pVT data measured. Also pressure has shown to influence the structure distribution during cooling of semi-crystalline materials. Results at low cooling rates are in accordance with results presented by Ito (36), Moldflow (61) and Zoller (90). Results at elevated pressures are in accordance with results presented by He (31), Ito (38) and Leute (58). Results at high cooling rates show a resemblance with the work of Piccarolo (69). The results stress that standard techniques are not able to characterize the specific volume of semi-crystalline polymers. Moreover, they can be modeled quite good (especially the transition when crystallization takes place) using the Schneider’s rate equations for quiescent crystallization. Thus, crystallization kinetics have to be known in order to get detailed information on the specific volume for semi-crystalline polymers. An experimental-numerical approach seems inevitable. On the one hand, modeling the crystallization process accurately, results in accurate predictions for the specific

volume. On the other hand, measuring the specific volume at a range of cooling rates and pressures, gives a first impression of the crystallization kinetics in the material.

6.5 Injection moulding

Two parts for understanding the processing of semi-crystalline polymers have been presented; (i) a flow-induced crystallization model, based on the recoverable strain in the melt and, (ii) an experimentally validated model that predicts the specific volume of semi-crystalline polymers in relation to cooling rate and pressure. Both are implemented in a computer code for the numerical simulation of the injection moulding process. It has been indicated, that important parts are missing to be able to predict dimensional stability for the final product. An example is the influence of the structure formed on the viscosity. So far, it has been assumed that the crystals form a separate phase in the amorphous melt, and change the viscosity accordingly. For the viscoelastic strain calculation we used the coupling between crystallinity and the maximum relaxation time, which, so far, did not influence the injection moulding simulation. A more detailed analysis has to be performed to improve on these aspects.

Since it is possible to calculate the structure distribution, the SCORIM process can and should be used to validate the models for (flow-induced) crystallization under realistic injection moulding conditions. The calculated structure distribution, resulting from processing, can serve as a starting point for studying dimensional stability, if the time dependent behavior of both the spherulitical and oriented structures are known. Basically, the determination of the time dependent (anisotropic) shrinkage behavior of both the spherulitical and oriented crystallized material, is the essential step from the calculated structure distribution, to dimensional stability. The structure distribution in fully oriented samples, created using the SCORIM process, can be used to study the effect of oriented material on the shrinkage behavior, in a more or less, independent way. By combining both phases, with their individual shrinkage behavior, the relation between shrinkage and structure (-distribution) can be studied. Then, a numerical dimensional stability analysis can be performed, and the final shape of the rectangular strip can be compared for different processing conditions. Since, it is not known, whether the shrinkage is determined by the amount of oriented material, the number of oriented structures, their length or anything else, most of the existing models mentioned in chapter 3, are not suitable for studying the relation between structure and shrinkage. The best perspectives here are clearly for the Eder model and the S_{J2} -model, proposed in chapter 3.

In conclusion, using a decoupled non-isothermal generalized Newtonian flow modeling, the kinematic result is used in the full 3D viscoelastic calculation, in which the evolution of the recoverable strain is described using the compressible Leonov model. Crystallization kinetics are incorporated using the S_{J2} -model, which is based on the second invariant of the deviatoric part of the recoverable strain; a measure for the molecular ordering phenomena in the melt. The set of differential equations forming the S_{J2} -model completely describes all properties that characterize the resulting structure, including the main molecular orientation. Including the new formulation proposed to describe the influence of structure formation on the specific volume, results in a complete modeling for processing of semi-crystalline polymers. Detailed analysis of the relation between the structure formed with the viscosity can

improve the numerical calculations. The structure distribution in the final product than can serve as a starting point for future studies: dimensional stability analysis!

Bibliography

- [1] F.P.T. Baaijens. Calculation of residual stresses in injection molded products. *Rheologica Acta*, 30:284–299, 1991. [2.1](#)
- [2] Z. Bashir, J.A. Odell, and A. Keller. High modulus filaments of polyethylene with lamellar structure by melt processing; the role of the high molecular weight component. *Journal of Material Science*, 19:3713–3725, 1984. [1.1.2](#), [1.1.2](#), [1.1.2](#), [1.1.5](#)
- [3] Z. Bashir, J.A. Odell, and A. Keller. Stiff and strong polyethylene with shish kebab morphology by continuous melt extrusion. *Journal of Material Science*, 21:3993–4002, 1986. [1.1.5](#)
- [4] A. Bénard, S.G. Advani, and J.M. Schultz. Solidification of semicrystalline polymers using a variable interface temperature model. *Journal of Polymer Science: Part B: Polymer Physics*, 34:471–483, 1996. [1.1.3](#)
- [5] J. Berger and W. Schneider. A zone model of rate controlled solidification. *Plastics and Rubber Processing and Applications*, 6:127–133, 1986. [1.1.3](#)
- [6] D.J. Blundell, D.H. MacKerron, W. Fuller, A. Mahendrasingam, C. Martin, R.J. Oldman, R.J. Rule, and C. Riekel. Characterization of strain-induced crystallization of poly(ethylene terephthalate) at fast draw rates using synchrotron radiation. *Polymer*, 37(15):3303–3311, 1996. [3.3.2](#)
- [7] A.H.M. Boshouwers and J.J. van der Werf. *Inject3, A Simulation Code for the Filling Stage of the Injection Moulding Process of Thermoplastics*. PhD thesis, Eindhoven University of Technology, 1988. [2](#)
- [8] A.C. Bushman and A.J. McHugh. A continuum model for the dynamics of flow-induced crystallization. *Journal of Polymer Science: Part B: Polymer Physics*, 34:2393–2407, 1996. [1.1.3](#), [3](#), [3](#), [5.3.1](#)
- [9] L. Caspers. *Vip, an integral approach to the simulation of injection moulding (prediction of product properties)*. PhD thesis, Eindhoven University of Technology, 1995. [1.1.6](#), [1.2](#), [2](#), [2.2](#), [2.2](#), [2.2](#), [2.2](#), [2.2](#), [2.3.1](#), [2.3.2](#), [5.2.2](#), [5.2.3](#)
- [10] R.Y. Chang, C.H. Chen, and K.S. Su. Modifying the tait equation with cooling rate effects to predict the pressure-volume-temperature behaviors of amorphous polymers: Modelling and experiments. *Polymer Engineering and Science*, 36(13):1789–1795, 1996. [4](#), [4](#)

- [11] R.Y. Chiang and B.D. Tsaur. Experimental and theoretical studies of shrinkage, warpage, and sink marks of crystalline polymer injection molded parts. *Polymer Engineering and Science*, 35(15):1222–1230, 1995. 1.1.5
- [12] A.K. Doufas, I.S. Dairanieh, and A.J. McHugh. A continuum model for flow-induced crystallization of polymer melts. *Journal of Rheology*, 43(1):85–109, 1999. 1.1.3, 3, 3, 3, 3, 3.6, 5.3.1
- [13] A. Douillard, Ph. Dumazet, B. Chabert, and J. Guillet. A comparative model for anisothermal and isothermal crystallization of poly(ethyleneterephthalate). *Polymer*, 34(8):1702–1708, 1993. 4
- [14] L.F.A. Douven. *Towards the Computation of Properties of Injection Moulded Products: flow- and thermally induced stresses in amorphous thermoplastics*. PhD thesis, Eindhoven University of Technology, 1995. 2, 2.2, 2.2
- [15] G. Eder. Crystallization kinetics equations incorporating surface and bulk nucleation processes. In *ICIAM95-Proceedings*. ZAMM, Akademik Verlag, 1996. 1.1.3
- [16] G. Eder. Fundamentals of structure formation in crystallizing polymers. In K. Hatada, T. Kitayama, and O. Vogl, editors, *Macromolecular Design of Polymeric Materials*. Marcel Dekker, New York, 1996. 1.1.3
- [17] G. Eder and H. Janeschitz-Kriegl. Heat transfer and flow: Transport phenomena controlling the crystallization processes in polymers. In S.I. Güçeri, editor, *Transport Phenomena in Processing*, pages 1031–1042. Technomic Publ. Co., 1993. 1.1.3
- [18] G. Eder and H. Janeschitz-Kriegl. Crystallization. In H.E.H. Meijer, ed, *Processing of Polymers*, chapter 5 in volume 18 of *Material Science and Technology*, eds. R.W. Cahn, P. Haasen and E.J. Kramer, pages 296–344. VCH Verlagsgesellschaft mbH, P.O.Box 10 11 61, D-69451 Weinheim, 1997. 3, 3, 3.1, 3.2.2, 3.2.2, 3.2.3, 3.4, 3.5, 3.5, 3.6, 3.6, 3.6, 5.1.2, 5.2.2, A.2, A.2, A.2
- [19] G. Eder, H. Janeschitz-Kriegl, and G. Krobath. Shear induced crystallization, a relaxation phenomenon in polymer melts. *Progress in Colloid & Polymer Science*, 80:1–7, 1989. 1.1.3
- [20] G. Eder, H. Janeschitz-Kriegl, and S. Liedauer. Crystallization processes in quiescent and moving polymer melts under heat transfer conditions. *Progress in Polymer Science*, 15:629–714, 1990. 3.1, 3.2.2, 3.2.3, 3.3, 3.3.2, 3.3.3, 3.5, 3.5, 5.2.3
- [21] J. Fiebig, M. Gahleitner, C. Paulik, and J. Wolfschwenger. Ageing of polypropylene: Processes and consequences. *Polymer Testing*, 18, 1999. 1.1.6, 5.1.2
- [22] E. Fleischmann and J. Koppelman. Effect of cooling rate and shear-induced crystallization on the pressure-specific volume-temperature diagram of isotactic polypropylene. *Journal of Applied Polymer Science*, 41:1115–1121, 1990. 1.1.4, 4, 4.2

- [23] E. Fleischmann, P. Zipper, A. Janosi, W. Geymayer, J. Koppelman, and J. Schurz. Investigations of the layered structure of injection-molded polypropylene discs and of its behavior in tensile tests. *Polymer Engineering and Science*, 29(12):835–843, 1989. [1.1.6](#)
- [24] M. Gahleitner, J. Fiebig, C. Paulik, J. Wolfschwenger, H. Zuidema, and G. Dreiling. Processing effects on physical ageing of polypropylene. In *Proceedings of PPS-15*, 's Hertogenbosch, June 1998, On CD-ROM. [1.1.6](#), [1.1.6](#), [5.1.1](#), [5.3.1](#)
- [25] M. Gahleitner, J. Wolfschwenger, C. Bachner, and K. Bernreiter. Crystallinity and mechanical properties of pp-homopolymers as influenced by molecular structure and nucleation. *Journal of Applied Polymer Science*, 61:649–657, 1996. [1.1.6](#)
- [26] SWO Polymertechnik GmbH. *The art of Material Testing*. Dahlerdyk 31, 47803 Krefeld, Germany, 1998. [4](#)
- [27] X. Guo and A.I. Isayev. Residual stresses and birefringence in injection molding of semicrystalline polymer. part i: Theoretical formulation. *International Polymer Processing XIV*, 4:377–386, 1999. [1.1.4](#), [2.3.2](#)
- [28] X. Guo and A.I. Isayev. Residual stresses and birefringence in injection molding of semicrystalline polymer. part ii: Experiment and simulation. *International Polymer Processing XIV*, 4:387–398, 1999. [1.1.5](#)
- [29] X. Guo, A.I. Isayev, and L. Guo. Crystallinity and microstructure in injection moldings of isotactic polypropylenes. part 1: A new approach to modeling and model parameters. *Polymer Engineering and Science*, 39(10):2096–2114, 1999. [1.1.3](#), [3](#), [3](#), [3.5](#), [3.5](#), [5.3.1](#)
- [30] G.A.A.V. Haagh. *Simulation of Gas-Assisted Injection Moulding*. PhD thesis, Eindhoven University of Technology, 1998. [2](#), [2.2](#)
- [31] J. He and P. Zoller. Crystallization of polypropylene, nylon-66 and poly(ethylene terephthalate) at pressures to 200 mpa: Kinetics and characterization of products. *Journal of Polymer Science: Part B: Polymer Physics*, 32:1049–1067, 1994. [4](#), [4](#), [4](#), [4.2](#), [4.2](#), [4.2](#), [4.3](#), [6.4](#)
- [32] C.A. Hieber. Modelling the pvt behavior of isotactic polypropylen. *International Polymer Processing*, 3:249–256, 1997. [4](#), [4.2](#)
- [33] C.A. Hieber and S.F. Shen. A finite-element/finite-difference simulation of the injection-molding filling process. *Journal of Non-Newtonian Fluid Mechanics*, 7:1–32, 1980. [2.2](#)
- [34] C.M. Hsiung and M. Cakmak. Effect of injection-molding conditions on the crystallinity, orientation gradients, and mechanical properties of poly(aryl ether ketone). ii. large dumbbell parts. *Journal of Applied Polymer Science*, 47:149–165, 1993. [1.1.6](#)
- [35] A.I. Isayev and B.F. Catignani. Crystallization and microstructure in quenched slabs of various molecular weight polypropylenes. *Polymer Engineering and Science*, 37(9):1526–1539, 1997. [1.1.3](#), [3](#), [3](#), [3](#), [5.3.1](#)

- [36] H. Ito, T. Kikutani, K. Tada, J. Takimoto, and K. Koyama. Modelling and numerical simulation of polymer crystallization in injection moulding process. In *Proceedings regional PPS meeting*, Göteborg Sweden, 1998. [1.1.4](#), [2.3.1](#), [4.2](#), [4.3](#), [6.4](#)
- [37] H. Ito, K. Minagawa, J. Takimoto, K. Tada, and K. Koyama. Effect of pressure and shear stress on crystallization behaviors in injection molding. *International Polymer Processing XI*, 4:363–368, 1996. [1.1.3](#), [3](#), [3](#), [3](#), [4](#), [5.3.1](#)
- [38] H. Ito, T. Takahashi, J. Takimoto, K. Tada, I. Tsujimura, and K. Koyama. Simulation of injection molding process. crystallization and its effects on material properties. In *Proceedings of PPS-12*, pages 437–438, Sorrento, Italy, May 27-31 1996. [4](#), [4.2](#), [4.3](#), [6.4](#)
- [39] H. Janeschitz-Kriegl. Polymer solidification by crystallization under heat transfer and flow conditions. *Progress in Colloid & Polymer Science*, 87:117–127, 1992. [1.1.3](#), [3](#), [3.1](#), [4.1](#)
- [40] H. Janeschitz-Kriegl. Conditions of nucleation in crystallizable polymers: Reconnaissance of positions - a critical evaluation. *Colloid Polymer Science*, 275:1121–1135, 1997. [1](#)
- [41] J.J. Janimak, S.Z.D. Cheng, and P.A. Giusti. Isotacticity effect on crystallization and melting in polypropylene fractions: 2. linear crystal growth rate and morphology study. *Macromolecules*, 24:2253–2260, 1991. [1.1.1](#)
- [42] K.M.B. Jansen. Measurement and prediction of anisotropy in injection moulded pp products. *International Polymer Processing XIII*, 3:309–317, 1998. [1.1.6](#), [5.1.2](#)
- [43] P. Jerschow. *Crystallization of Polypropylene. New experiments, evaluation methods and choice of material compositions*. PhD thesis, Johannes Kepler Universitat, Linz, Austria, Juli 1994. [3](#), [3.2.2](#), [3.2.2](#), [3.2](#), [3.2.2](#), [3](#), [3.6](#), [3.5](#), [3.6](#), [5.1.2](#), [A.2](#)
- [44] P. Jerschow and H. Janeschitz-Kriegl. The role of long molecules and nucleating agents in shear induced crystallization of isotactic polypropylenes. *International Polymer Processing XII*, 1:72–77, 1997. [1.1](#), [3.2](#), [3.5](#), [3.5](#), [3.5](#), [3.5](#), [3.5](#), [3.5](#), [3.5](#), [3.17](#), [3.5](#), [3.18](#)
- [45] P. Jerschow and H. Janeschitz-Kriegl. On the development of oblong particles as precursors for polymer crystallization from shear flow: Origin of the so-called fine grained layers. *Rheological Acta*, 35:127–133, 1996. [1.1.3](#)
- [46] G. Kalay, P. Allan, and M.J. Bevis. γ phase in injection moulded isotactic polypropylene. *Polymer*, 35(12):2480–2482, 1994. [3](#), [5.3.2](#)
- [47] G. Kalay and M. Bevis. *Structure Development during Solidification in the Processing of Crystalline Polymers (DECRYPO)*, Report no.11, BRITE-EURAM III, project BE 95-2067. Number 11. 1998. [5.12](#)
- [48] A. Keller and J.W.H. Kolnaar. Flow-induced orientation and structure formation. In H.E.H. Meijer, ed, *Processing of Polymers*, chapter 4 in volume 18 of *Material Science*

- and Technology*, eds. R.W. Cahn, P. Haasen and E.J. Kramer, pages 189–268. VCH Verlagsgesellschaft mbH, P.O.Box 10 11 61, D-69451 Weinheim, 1997. [1.1.1](#), [1.1.2](#), [1.1.2](#), [1.2](#), [1.1.5](#)
- [49] A.N. Kolmogoroff. On the statistical theory of the crystallization of metals. (in russian). *Izvestiya Akad. Nauk SSSR*, 1, 1937. [1.1.3](#)
- [50] D.W. van Krevelen. *Properties of Polymers*. Elsevier, 1976. [A.1](#), [A.2](#)
- [51] G. Kumaraswamy, A.M. Issaian, and J.A. Kornfield. Shear-enhanced crystallization in isotactic polypropylene. 1. correspondence between in situ rheo-optics and ex situ structure determination. *Macromolecules*, 32:7537–7547, 1999. [3](#), [3.5](#), [3.5](#)
- [52] R.R. Lagasse and B. Maxwell. An experimental study of the kinetics of polymer crystallization during shear flow. *Polymer Engineering and Science*, 16(3):189–199, 1976. [1.1.4](#), [3.5](#), [3.5](#), [3.5](#), [3.5](#), [3.16](#)
- [53] R.G. Larson. *Constitutive Equations for Polymer Melts and Solutions*. Chemical Engineering. Butterworths, 1988. [2.1](#), [2](#)
- [54] R.G. Larson. *The Structure and Rheology of Complex Fluids*. Oxford University Press, 1999. [2](#)
- [55] P.J. Lemstra, L. Govaert, E. Nies, and T. Tervoort. *Polymere Materialen*. Eindhoven University of Technology. [1.2](#)
- [56] A.I. Leonov. Nonequilibrium thermodynamics and rheology of viscoelastic polymer media. *Rheologica Acta*, 15:85–98, 1976. [2.1](#)
- [57] A.I. Leonov. On a class of constitutive equations for viscoelastic fluids. *Non-Newtonian Fluid Mechanics*, 25:1–59, 1987. [2.1](#)
- [58] U. Leute, W. Dollhopf, and E. Liska. Dilatometric study on the melting of polypropylene at elevated pressures. *Colloid Polymer Science*, 256:914–922, 1978. [4.2](#), [4.3](#), [6.4](#)
- [59] S. Liedauer, G. Eder, H. Janeschitz-Kriegl, P. Jerschow, W. Geymayer, and E. Ingolic. On the kinetics of shear induced crystallization in polypropylene. *International Polymer Processing VIII*, 3:236–244, 1993. [3.1](#), [3.1](#)
- [60] H. Lobo and T. Bethard. Capturing pvt behavior of injection-molded parts using hybrid methods. (*personal communications*). [4](#)
- [61] Moldflow Pty. Ltd. *Material Testing Procedures Manual*. 259-261 Colchester Road, Kilsyth, Victoria, 3137, Australia, 1995. [4](#), [4.1](#), [4.2](#), [4.2](#), [4.5](#), [4.3](#), [6.4](#), [A.3](#)
- [62] M.R. Mackley, F.C. Frank, and A. Keller. Flow-induced crystallization of polyethylene melts. *Journal of Material Science*, 10:1501–1509, 1975. [1.1.2](#)

- [63] A. Malkin. General treatment of polymer crystallization kinetics. part 1. a new macrokinetic equation and its experimental verification. *Polymer Engineering and Science*, 24:1396–1401, 1984. 3.2.1, 3.1
- [64] A.J. McHugh, R.K. Guy, and D.A. Tree. Extensional flow-induced crystallization of a polyethylene melt. *Colloid & Polymer Science*, 271:629–645, 1993. 3
- [65] H.E.H. Meijer. Processing for properties. In H.E.H. Meijer, ed, *Processing of Polymers*, chapter 1 in volume 18 of *Material Science and Technology*, eds. R.W. Cahn, P. Haasen and E.J. Kramer, pages 3–75. VCH Verlagsgesellschaft mbH, P.O.Box 10 11 61, D-69451 Weinheim, 1997. 1.1.4, 1.1.6
- [66] K. Nakamura, T. Watanabe, K. Katayama, and T. Amano. Some aspects of nonisothermal crystallization of polymers. i. relationship between crystallization temperature, crystallinity, and cooling conditions. *Journal of Applied Polymer Science*, 16:1077–1091, 1972. 1.1.3, 3, 3, 3, 5.3.1
- [67] J. Petermann, M. Miles, and H. Gleiter. The crystalline core of the row structures in isotactic polystyrene. i. nucleation and growth. *Journal of Polymer Science*, 17:55–62, 1979. 1.1.2
- [68] G.W.M. Peters, J.F.M. Schoonen, F.P.T. Baaijens, and H.E.H. Meijer. On the performance of enhanced constitutive models for polymer melts in a cross-slot flow. *Journal of Non-Newtonian Fluid Mechanics*, 82:387–427, 1998. 2.1, 2.1, 3.6
- [69] S. Piccarolo. Morphological changes in isotactic polypropylene as a function of cooling rate. *Journal of Macromolecular Science*, B31(4):501–511, 1992. 4, 4, 4.2, 4.2, 4.2, 4.3, 6.4
- [70] S. Piccarolo, M. Saiu, V. Brucato, and G. Titomanlio. Crystallization of polymer melts under fast cooling. ii. high-purity ipp. *Journal of Applied Polymer Science*, 46:625–634, 1992. 4.2
- [71] M. Saiu, V. Brucato, S. Piccarolo, and G. Titomanlio. Injection molding of ipp. *International Polymer Processing VII*, 3:267–273, 1992. 1.1.5
- [72] Y. Sato, Y. Yamasaki, S. Takishima, and H. Masuoka. Precise measurements of the pvt of polypropylene and polycarbonate up to 330 °c and 200mpa. *Journal of Applied Polymer Science*, 66:141–150, 1997. 4
- [73] W. Schneider, J. Berger, and A. Köppl. Non-isothermal crystallization of polymers: Application of rate equations. In *Physico-Chemical Issues in Polymers*, pages 1043–1054. Technomic Publ. Co., 1993. 3.2.1, A.1, A.1
- [74] W. Schneider, A. Köppl, and J. Berger. Non-isothermal crystallization, crystallization of polymers. *International Polymer Processing II*, 3(4):151–154, 1988. 1.1.3, 3, 3.1, 4.1

- [75] G.E.W. Schultz and T.R. Naujeck. A growing 2d spherulite and calculus of variations part i: A 2d spherulite in a linear field of growth rate. *Colloid & Polymer Science*, 269:289–694, 1991. 1.1.3
- [76] C.W.M. Sitters. *Numerical Simulation of Injection Moulding*. PhD thesis, Eindhoven University of Technology, 1988. 2
- [77] R.S. Spencer and G.D. Gilmore. Equation of state for polystyrene. *Journal of Applied Physics*, 20:502–506, 1949. 4
- [78] J. Stefan. On the theory of formation of ice, in particular in the polar sea, (in german). In *Ann. Phys. u. Chem.*, page 1891. Wiedemann, 1959. 1.1.3
- [79] F.H.M. Swartjes, H. Zuidema, and U. Goschel. *A quantitative analysis of flow induced nucleation that enhances crystallisation in bulk polymers using a new cross-slot device*. *ESRF Annual Report; experimental report of sc425*. Grenoble, 1998. 3.6, 4.3
- [80] P.P. Tas. *Film Blowing from polymer to product*. PhD thesis, Eindhoven University of Technology, 1994. 1.1.5, 3.3.2, 3.3.2
- [81] N.J. Terrill, J.P. Fairclough, E. Towns-Andrews, B.U. Komanschek, R.J. Young, and A.J. Ryan. Density fluctuations: The nucleation event in isotactic polypropylene crystallisation. *Polymer: the chemistry, physics and technology of high polymers*, 39(11):2381–2386, 1998. 1.1.2
- [82] C.L. Tucker. *Fundamentals of Computer Modelling for Polymer Processing*. Hanser Publishers, Munich, 1991. 2.2
- [83] A.K. van der Vegt and P.P.A. Smit. Crystallization phenomena in flowing polymers. *Adv. Polym. Sci.*, 26(313), 1967. 1.1.5
- [84] W.M.H. Verbeeten, G.W.M. Peters, and F.P.T. Baaijens. Differential constitutive equations for polymer melts: the enhanced pompon models. *submitted to Journal of Rheology*, 2000. 2.1, 3.6, 6.3
- [85] O. Verhoyen. *Crystallization of PolyEthylene Terephthalate in Injection Moulding: Experiments, Modelling and Numerical Simulations*. PhD thesis, Universite catholique de Louvain, 1997. 1.1.4, 2.3.2, 3, 3
- [86] O. Verhoyen, F. Dupret, and R. Legras. Isothermal and non-isothermal crystallization kinetics of polyethylene terephthalate: Mathematical modeling and experimental measurements. *Polymer Engineering and Science*, 38(9):1594–1610, 1998. 1.1.3
- [87] S. Vleeshouwers and H.E.H. Meijer. A rheological study of shear induced crystallization. *Rheologica Acta*, 35:391–399, 1996. 1.1.4, 3.3.2, 3.3.2, 3.5, 3.5, 3.5, 3.5, 3.5, 3.5, 3.5, 3.14, 3.14, 3.5, 3.5
- [88] C.H. Wu, G. Eder, and H. Janeschitz-Kriegl. Polymer crystallization dynamics, as reflected by differential scanning calorimetry. part ii: Numerical simulations. *Colloid & Polymer Science*, 271:1116–1128, 1993. 4

-
- [89] W.F. Zoetelief. *Multi-Component Injection Moulding*. PhD thesis, Eindhoven University of Technology, 1995. 2, 2
- [90] P. Zoller. Pressure-volume-temperature relationship of solid and molten polypropylene and poly(butene-1). *Journal of Applied Polymer Science*, 23:1057–1061, 1979. 4, 4.1, 4.2, 4.3, 6.4
- [91] P. Zoller. A study of the pressure-volume-temperature relationships of four related amorphous polymers: Polycarbonate, polyarylate, phenoxy, and polysulfone. *Journal of Polymer Science*, 20:1453–1464, 1982. 4
- [92] P. Zoller and Y. Fakhreddine. Pressure-volume-temperature studies of semi-crystalline polymers. *Thermochimica Acta*, 238:397–415, 1994. 4, 4
- [93] H. Zuidema, G.W.M. Peters, and H.E.H. Meijer. Development of strain induced crystallisation modelling using the scorim process. In *Proceedings of PPS-15*, 's Hertogenbosch, June 1999, On CD-ROM. 3.3.2
- [94] H. Zuidema, G.W.M. Peters, and H.E.H. Meijer. Development and validation of a recoverable strain based model for flow-induced crystallization of polymers. *Submitted to Macromolecular Theory and Simulations*, 2000. 1.1.4, 1, 4.1, 4.3
- [95] H. Zuidema, G.W.M. Peters, and H.E.H. Meijer. Influence of cooling rate on pvt-data of semi-crystalline polymers. *Submitted to Journal of Applied Polymer Science*, 2000. 1

Appendix A

Material characterization

In this appendix, the materials used in the experiments are characterized for usage in the numerical simulations. Since the Polyamide 6 is only used in the quiescent crystallization experiments, only the material properties are determined together with the crystallization data (see section A.1). For both polypropylenes used in the flow experiments, besides the material properties and the crystallization data, also a rheological characterization has been done (see sections A.2 and A.3).

A.1 Polyamide 6

Schneider (73) determined the number of spherulites to be $N = 6 \cdot 10^{11} [m^{-3}]$ together with a crystal growth rate described by (see fig. A.1):

$$G = \frac{G_0}{L} e^{-\frac{C_d}{T-T_g} - \frac{CT_m}{T(T_m-T)}} \quad (\text{A.1})$$

in which T is the temperature. The parameters are listed in table A.2. From Krevelen (50) the heat of crystallization H and the maximum degree of crystallinity V_∞ are obtained (table A.1).

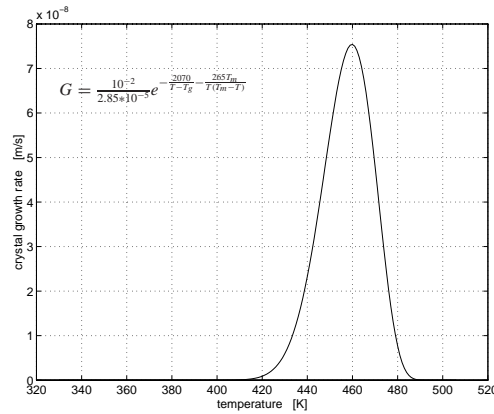


Fig. A.1: The crystal growth rate curve as a function of temperature for Polyamide 6, data from (73).

| | | |
|------------|--------|--------------------|
| c_p | 2136.9 | $[Jkg^{-1}K^{-1}]$ |
| λ | 0.21 | $[Wm^{-1}K^{-1}]$ |
| T_g | 330 | $[K]$ |
| T_m | 506 | $[K]$ |
| H | 192474 | $[Jkg^{-1}]$ |
| V_∞ | 0.35 | $[-]$ |

Tab. A.1: Material properties of polyamide 6, in which c_p the thermal capacity, λ the thermal conductivity, T_g the glass transition temperature, T_m the melting temperature, H the heat of crystallization and V_∞ the maximum degree of crystallinity.

| | | |
|-------|----------------------|-------------|
| G_0 | 10^{-2} | $[ms^{-1}]$ |
| C_d | 2070 | $[K]$ |
| C | 265 | $[K]$ |
| L | $2.85 \cdot 10^{-5}$ | $[-]$ |

Tab. A.2: Parameters of the crystal growth rate model of polyamide 6.

A.2 Polypropylene (KS10, Borealis)

Since no pVT data are available for the tested polypropylene Daplen KS10 (Borealis), the specific volume ν in the melt is taken constant (table A.3). However, this only causes a very small difference in the build-up of the recoverable strain and has hardly any influence on the results. Other material properties are listed in table A.3 as well. The number of spherulitical nuclei is determined by Eder (18) and described by the following expression (fig. A.2, left):

$$N = N_r e^{-\tilde{\beta}(T-T_r)} \quad (\text{A.2})$$

in which N the number of spherulites, N_r the number of spherulites at the reference temperature T_r (table A.4). The crystal growth rate G is also determined by Eder (18) and described by the following expression (fig. A.2, right):

$$G = G_{max} e^{-\beta(T-T_{ref})^2} \quad (\text{A.3})$$

in which G_{max} the crystal growth rate at the reference temperature T_{ref} (table A.5). From Krevelen (50) the heat of crystallization H is obtained (table A.3). The parameters for the shear induced crystallization model are determined by Eder (18) as well; the relaxation time for the nuclei is $\tau_n = \infty$ because all nuclei are assumed to grow into threads immediately after their creation, the relaxation time for the shish $\tau_l = 0.25$, and the combination of parameters $\left. \frac{g_n}{\dot{\gamma}_n^2} \right|_{T=423[K]} = 4.685 \cdot 10^{12}$ and $\left. \frac{g_l}{\dot{\gamma}_l^2} \right|_{T=423[K]} = 2.690 \cdot 10^{-10}$. These combinations consists of two critical shear rates; for the nuclei formation $\dot{\gamma}_n$ and for the shish extensioning $\dot{\gamma}_l$ together with two scale factors; for the total number of nuclei g_n and the total shish-length g_l . The viscosity η is modeled using a Carreau model in which $\dot{\gamma}$ is the shear rate, using the variables in table A.6;

$$\eta = \frac{\eta_0}{(1+(\Lambda\dot{\gamma})^m)^{\frac{1-n}{m}}} \quad (\text{A.4})$$

This viscosity is not taken crystallinity dependent since the isothermal experiments were performed at a temperature and shear time for which lamellar crystal growth during flow is negligible. The rheological behavior for the computation of the flow-induced recoverable strain and orientation is described by the compressible Leonov model. The parameters are determined using oscillatory shear experiments, shifted to the reference temperature $T_{Lr} = 473[K]$. The fits for the storage and loss modulus are shown in fig. A.3, while the parameters are listed in table A.7. The temperature dependent shift factor $\log a_T(T)$ as determined by Jerschow (43) equals $0.0106[K^{-1}]$, from which the parameters C_1 and C_2 in the WLF-equation become $10[-]$ and $1000[K]$ respectively.

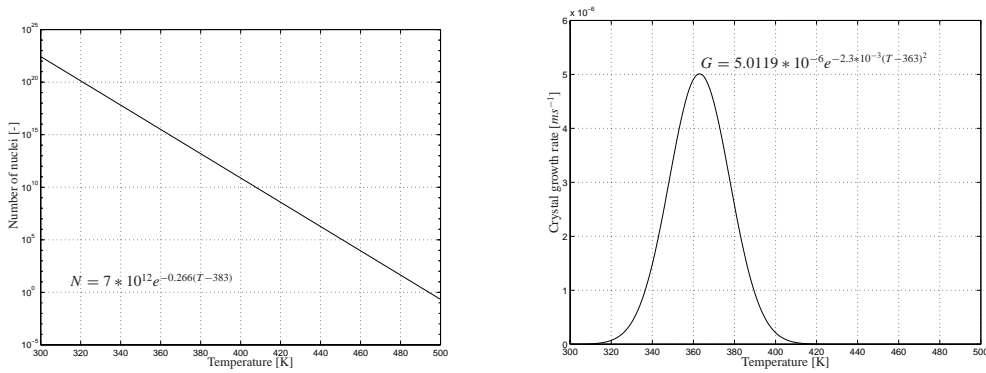


Fig. A.2: The distribution of the number of nuclei (left) and the crystal growth rate curve (right) as a function of temperature for polypropylene Daplen KS10 (Borealis).

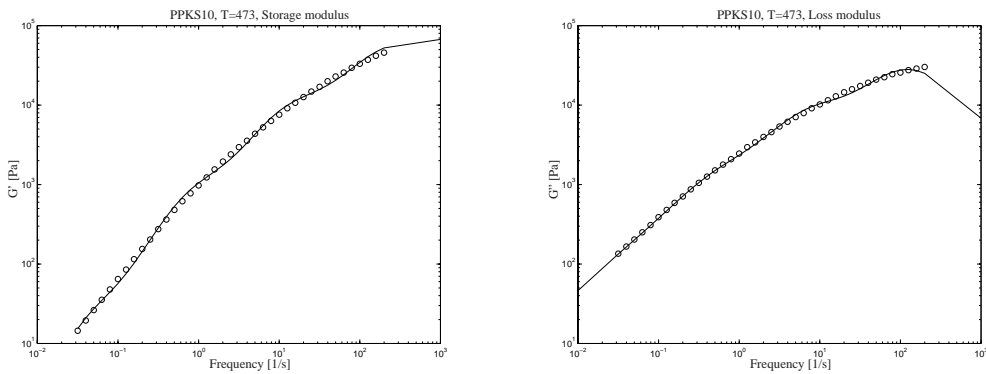


Fig. A.3: Experimental (symbols) and fitted (lines) storage modulus (left) and loss modulus (right) for polypropylene (Daplen KS10, Borealis).

| | | |
|-----------|-----------------------|-----------------------|
| ν | $9.225 \cdot 10^{-4}$ | $[m^3 \cdot kg^{-1}]$ |
| c_p | 2136.9 | $[Jkg^{-1}K^{-1}]$ |
| λ | 0.21 | $[Wm^{-1}K^{-1}]$ |
| T_g | 300 | $[K]$ |
| H | 163021 | $[Jkg^{-1}]$ |

Tab. A.3: Material properties of isotactic polypropylene Daplen KS10 (Borealis), in which ν the specific volume, c_p the thermal capacity, λ the thermal conductivity, T_g the glass transition temperature and H the heat of crystallization.

| | | |
|-----------------|-------------------|------------|
| N_r | $7 \cdot 10^{12}$ | $[m^{-3}]$ |
| T_r | 383 | $[K]$ |
| $\tilde{\beta}$ | 0.266 | $[K^{-1}]$ |

Tab. A.4: Parameters of the spherulitical nucleation model of isotactic polypropylene Daplen KS10 (Borealis), in which N_r the number of spherulites at the reference temperature T_r and $\tilde{\beta}$ a shape parameter.

A.3 Polypropylene (K2Xmod, Borealis)

This C3-homopolymer with high stereo-regularity and heterogeneous nucleation is a high-stiffness grade for injection moulding and cast film applications. Molecular data are obtained by Borealis Austria using GPC (TCB / 408[K] / mixed bed column, PS-calibration) and are shown in table A.8.

Standard pVT measurements are performed by Moldflow (61) using a GNOMIX RESEARCH confining fluid pVT apparatus in the isothermal mode starting at the ambient temperature (heating cycle) over a 10–160[MPa] pressure range (figure A.4). From these measurements the parameters are determined (table A.9), which describe the lower and higher temperature asymptotes using the specific volume model (eqn. 4.4).

The number of spherulites as a function of temperature is determined by Linz University (Austria), using a quenching technique, and is described by;

$$N = n_1 T + n_2 \quad , \quad T \leq T_m \quad (A.5)$$

for which the parameters are given in table A.10 (figure A.5).

| | | |
|-----------|------------------------|-------------|
| G_{max} | $5.0119 \cdot 10^{-6}$ | $[ms^{-1}]$ |
| T_{ref} | 363 | $[K]$ |
| β | $2.3 \cdot 10^{-3}$ | $[K^{-2}]$ |

Tab. A.5: Parameters of the crystal growth rate model of isotactic polypropylene Daplen KS10 (Borealis), in which G_{max} the crystal growth rate at the reference temperature T_{ref} and β a shape parameter.

| | | | | |
|-----------|---------|--------|---------|--------|
| T | 423 | [K] | 473 | [K] |
| η_0 | 16581.4 | [Pa.s] | 4893.5 | [Pa.s] |
| Λ | 1.11849 | [Pa] | 0.33009 | [Pa] |
| m | 0.49113 | [-] | 0.49113 | [-] |
| n | 0.35903 | [-] | 0.35903 | [-] |

Tab. A.6: Parameters for the Carreau model for the viscosity of the polypropylene Daplen KS10 (Borealis).

| | PP KS10 | $G_\infty = 0.0$ |
|-----|---------------|---------------------|
| j | $\theta_j[s]$ | $G_j[Pa]$ |
| 1 | 29.7434 | $0.0033 \cdot 10^4$ |
| 2 | 1.5679 | $0.1208 \cdot 10^4$ |
| 3 | 0.1144 | $1.2099 \cdot 10^4$ |
| 4 | 0.0080 | $5.4568 \cdot 10^4$ |

Tab. A.7: Linear viscoelastic parameters for the compressible Leonov model of the polypropylene Daplen KS10 (Borealis).

The crystal growth rate as a function of temperature is determined by Linz University (Austria), using thin film crystallization, and is described by;

$$G = G_{max} e^{-2 \frac{(T - T_{ref} - a(p - p_{ref}))^2}{\beta}} \quad (\text{A.6})$$

for which the parameters are given in table A.11 (figure A.6).

The rheological behavior for the computation of the flow-induced recoverable strain and orientation is described by the compressible Leonov model. The parameters are determined using oscillatory shear experiments, shifted to the reference temperature $T_{Lr} = 503[K]$. The fits for the storage and loss modulus are shown in fig. A.7, while the parameters are listed in table A.12.

The temperature dependent shift factor $\log a_T(T)$ is described using the WLF-equation, for which the parameters C_1 and C_2 become 9[-] and 1050[K] respectively. The viscosity η is modeled using a multi-mode Leonov model in which $\dot{\gamma}$ is the shear rate, using the variables in table A.12;

$$\eta = \eta_\infty + \sum_{i=1}^m \frac{2\eta_i a_T}{1 + \sqrt{1 + (2\dot{\gamma}\theta_i a_T)^2}} \quad (\text{A.7})$$

| | | |
|-------|-----|-------------------------|
| M_w | 365 | [kg mol ⁻¹] |
| M_n | 67 | [kg mol ⁻¹] |

Tab. A.8: Molecular data of the isotactic polypropylene (K2Xmod, Borealis) obtained using GPC.

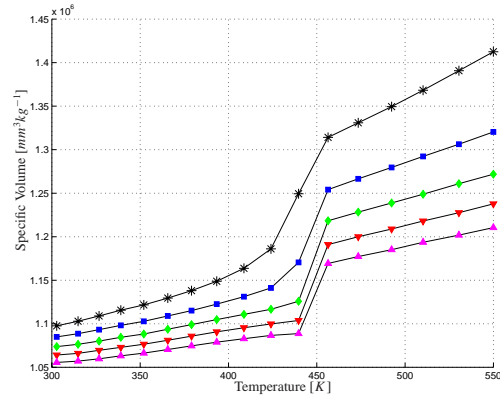


Fig. A.4: Standard pVT data of the iPP K2Xmod at pressures of 0.1 (*), 40 (■), 80 (◆), 120 (▼) and 160 [MPa] (▲).

Other material parameters are listed in table A.13 and the parameters for the S_{J2} -model for flow-induced crystallization in table A.14.

| | | |
|---|------------------------|---|
| T_{ref} | 273 | [K] |
| P_{ref} | $1 \cdot 10^5$ | [Pa] |
| V_{∞} | 0.80 | [-] |
| ρ_a | $8.7796 \cdot 10^{-7}$ | [kg mm ⁻³] |
| $\frac{\partial \rho_a}{\partial T}$ | $-6.40 \cdot 10^{-10}$ | [kg mm ⁻³ K ⁻¹] |
| $\frac{\partial \rho_a}{\partial p}$ | $6.0 \cdot 10^{-16}$ | [kg mm ⁻³ Pa ⁻¹] |
| $\frac{\partial^2 \rho_a}{\partial T^2}$ | 0.0 | [kg mm ⁻³ K ⁻²] |
| $\frac{\partial^2 \rho_a}{\partial p \partial T}$ | $2.10 \cdot 10^{-18}$ | [kg mm ⁻³ K ⁻¹ Pa ⁻¹] |
| $\frac{\partial^2 \rho_a}{\partial p^2}$ | $-2.6 \cdot 10^{-24}$ | [kg mm ⁻³ Pa ⁻²] |
| ρ_c | $9.3896 \cdot 10^{-7}$ | [kg mm ⁻³] |
| $\frac{\partial \rho_c}{\partial T}$ | $-4.24 \cdot 10^{-10}$ | [kg mm ⁻³ K ⁻¹] |
| $\frac{\partial \rho_c}{\partial p}$ | $2.0 \cdot 10^{-16}$ | [kg mm ⁻³ Pa ⁻¹] |
| $\frac{\partial^2 \rho_c}{\partial T^2}$ | 0.0 | [kg mm ⁻³ K ⁻²] |
| $\frac{\partial^2 \rho_c}{\partial p \partial T}$ | $1.30 \cdot 10^{-18}$ | [kg mm ⁻³ K ⁻¹ Pa ⁻¹] |
| $\frac{\partial^2 \rho_c}{\partial p^2}$ | 0.0 | [kg mm ⁻³ Pa ⁻²] |

Tab. A.9: Model parameters for the specific volume, using eqn. 4.4.

| | |
|-------|--|
| n_1 | $-2.6087 \cdot 10^{13}$ [K ⁻¹] |
| n_2 | $6.5783 \cdot 10^{15}$ [-] |

Tab. A.10: Model parameters for the number of crystals of the isotactic polypropylene (K2Xmod, Borealis) using equation A.5.

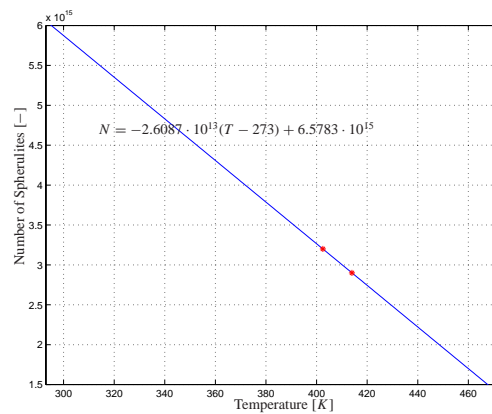


Fig. A.5: Measurements (*) and fit (-) on the number of spherulites of the iPP K2Xmod.

| | | |
|-----------|---------------------|-----------------|
| G_{max} | $8.1 \cdot 10^{-6}$ | $[ms^{-1}]$ |
| T_{ref} | 83.8 | $[^{\circ}C]$ |
| β | 1126.9 | $[^{\circ}C^2]$ |
| a | $5 \cdot 10^{-7}$ | $[KPa^{-1}]$ |
| P_{ref} | $1 \cdot 10^5$ | $[Pa]$ |

Tab. A.11: Model parameters for the crystal growth rate of the isotactic polypropylene (K2Xmod, Borealis) using equation A.6.

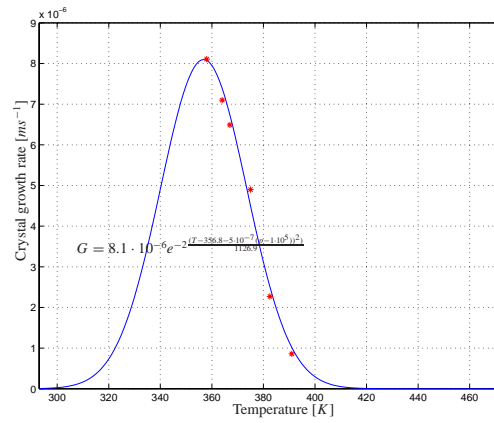


Fig. A.6: Measurements (*) and fit (—) on the crystal growth rate of the iPP K2Xmod at atmospheric pressure.

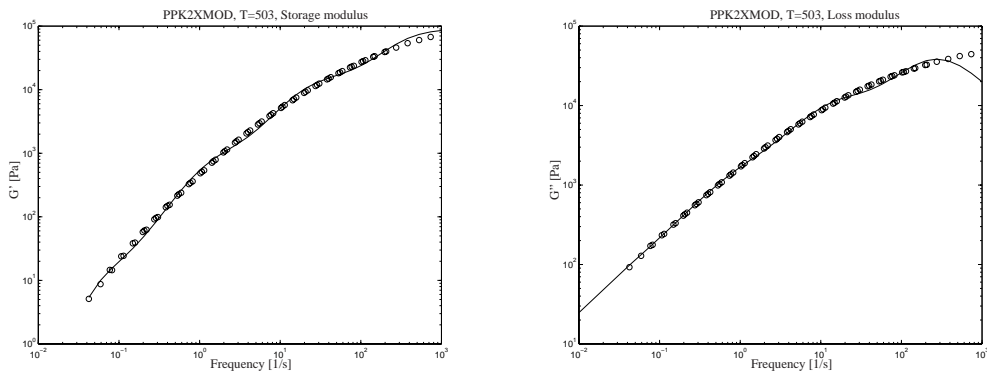


Fig. A.7: Experimental (symbols) and fitted (lines) storage modulus (left) and loss modulus (right) for polypropylene (Daplen K2Xmod, Borealis).

| | PP K2Xmod | $G_\infty = 0.0$ |
|-----|----------------|---------------------|
| j | $\theta_j [s]$ | $G_j [Pa]$ |
| 1 | 20.9476 | $0.0019 \cdot 10^4$ |
| 2 | 0.8860 | $0.1065 \cdot 10^4$ |
| 3 | 0.0597 | $1.4915 \cdot 10^4$ |
| 4 | 0.0035 | $7.4965 \cdot 10^4$ |

Tab. A.12: Linear viscoelastic parameters for the compressible Leonov model of the polypropylene Daplen K2Xmod (Borealis).

| | | |
|-----------|--------|--------------------|
| c_p | 2136.9 | $[Jkg^{-1}K^{-1}]$ |
| λ | 0.21 | $[Wm^{-1}K^{-1}]$ |
| T_g | 277 | $[K]$ |
| H | 110000 | $[Jkg^{-1}]$ |

Tab. A.13: Material properties of isotactic polypropylene Daplen K2Xmod (Borealis), in which c_p the thermal capacity, λ the thermal conductivity, T_g the glass transition temperature and H the heat of crystallization.

| | | |
|----------|-----------------------|-------|
| g'_n | $2.017 \cdot 10^{11}$ | $[-]$ |
| g'_l | $1.429 \cdot 10^{-1}$ | $[-]$ |
| α | $7 \cdot 10^{-6}$ | $[-]$ |

Tab. A.14: Parameters for the S_{J_2} -model of isotactic polypropylene Daplen K2Xmod (Borealis), in which g'_n is the scaling parameter for the influence of the driving force J_2 on the number of nuclei, g'_l the scaling parameter for the influence of the driving force J_2 on the thread-like growth of the nuclei and α the scaling parameter for the influence of the number of nuclei on the rheological relaxation time.

Appendix B

Experimental results

An experimental study has been performed on the influence of different processing conditions on the distribution of the oriented layers in the final (injection moulded) product, and the accompanying dimensional stability. Variations in the temperature of the melt injected, the volume flux during filling and the temperature of the mould wall have been used (see table B.1).

| no. | T_{inj} [K] | Q_{inj} [ms^{-1}] | T_w [K] |
|-----|---------------|-------------------------|-----------|
| 1 | 553 | $1.28 \cdot 10^{-4}$ | 333 |
| 2 | 473 | $1.28 \cdot 10^{-4}$ | 333 |
| 3 | 553 | $0.16 \cdot 10^{-4}$ | 333 |
| 4 | 473 | $0.16 \cdot 10^{-4}$ | 333 |
| 5 | 553 | $1.28 \cdot 10^{-4}$ | 293 |
| 6 | 473 | $1.28 \cdot 10^{-4}$ | 293 |
| 7 | 553 | $0.16 \cdot 10^{-4}$ | 293 |
| 8 | 473 | $0.16 \cdot 10^{-4}$ | 293 |

Tab. B.1: Experimental processing conditions applied to study the influence of these conditions on the structure distribution and accompanying shrinkage, in which T_{inj} is the temperature of the melt injected, Q_{inj} the volume flux during filling and T_w the temperature of the mould wall.

In this appendix the experimental results are presented for each combination of processing conditions. For example, for the experimental processing conditions applied as presented in table B.1 (no.1), the shrinkage measurements performed at the positions as presented in fig. 5.1, together with the reproduction of the shape resulting from the shrinkage are presented in fig. B.1.

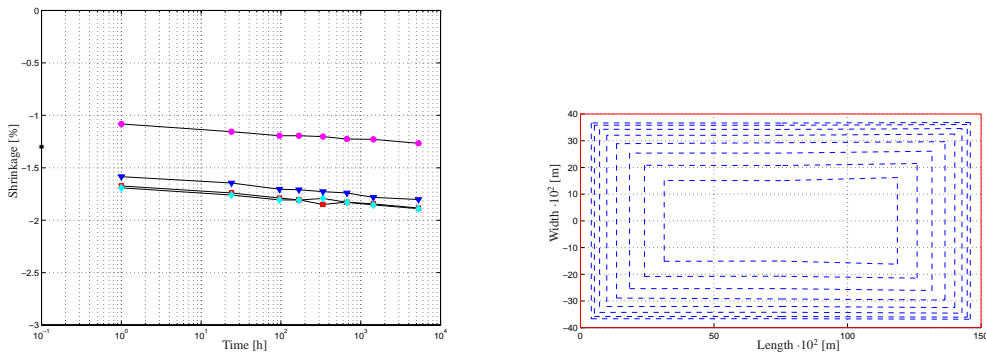


Fig. B.1: Shrinkage measurements performed at the positions as presented in fig. 5.1 (left), together with the magnified reproduction of the shape resulting from the shrinkage (right), for the processing conditions as shown in table B.1 (no.1). Bullet: longitudinal shrinkage, squares: width shrinkage near the gate, diamond: width shrinkage in between the gate and the end, and triangle: width shrinkage far from the gate.

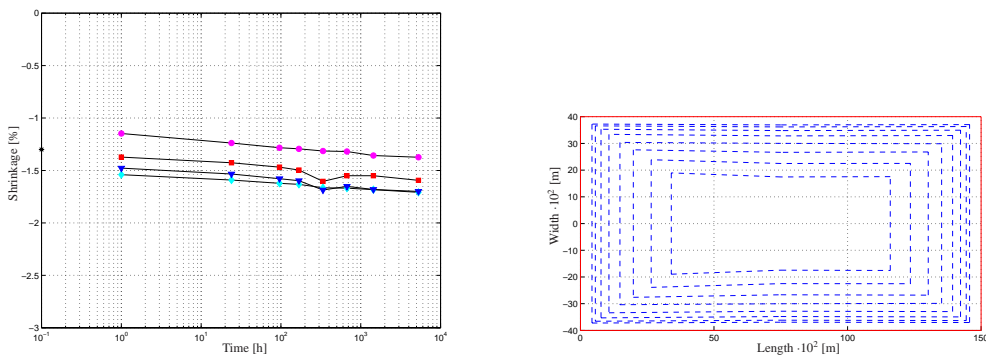


Fig. B.2: Shrinkage measurements performed at the positions as presented in fig. 5.1 (left), together with the magnified reproduction of the shape resulting from the shrinkage (right), for the processing conditions as shown in table B.1 (no.2). Bullet: longitudinal shrinkage, squares: width shrinkage near the gate, diamond: width shrinkage in between the gate and the end, and triangle: width shrinkage far from the gate.

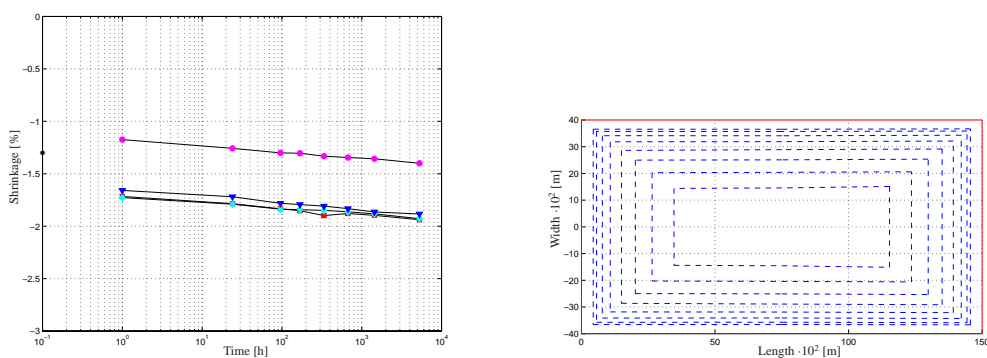


Fig. B.3: Shrinkage measurements performed at the positions as presented in fig. 5.1 (left), together with the magnified reproduction of the shape resulting from the shrinkage (right), for the processing conditions as shown in table B.1 (no.3). Bullet: longitudinal shrinkage, squares: width shrinkage near the gate, diamond: width shrinkage in between the gate and the end, and triangle: width shrinkage far from the gate.

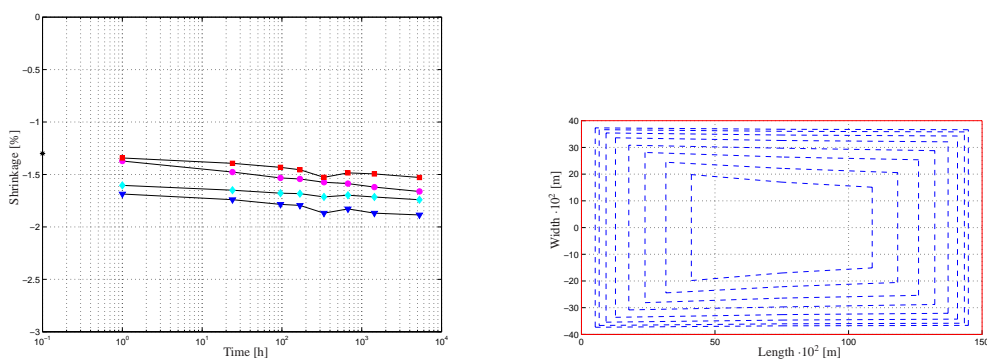


Fig. B.4: Shrinkage measurements performed at the positions as presented in fig. 5.1 (left), together with the magnified reproduction of the shape resulting from the shrinkage (right), for the processing conditions as shown in table B.1 (no.4). Bullet: longitudinal shrinkage, squares: width shrinkage near the gate, diamond: width shrinkage in between the gate and the end, and triangle: width shrinkage far from the gate.

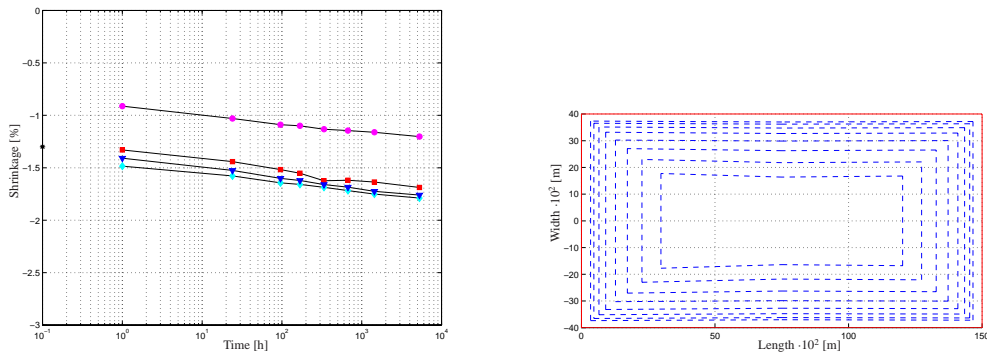


Fig. B.5: Shrinkage measurements performed at the positions as presented in fig. 5.1 (left), together with the magnified reproduction of the shape resulting from the shrinkage (right), for the processing conditions as shown in table B.1 (no.5). Bullet: longitudinal shrinkage, squares: width shrinkage near the gate, diamond: width shrinkage in between the gate and the end, and triangle: width shrinkage far from the gate.

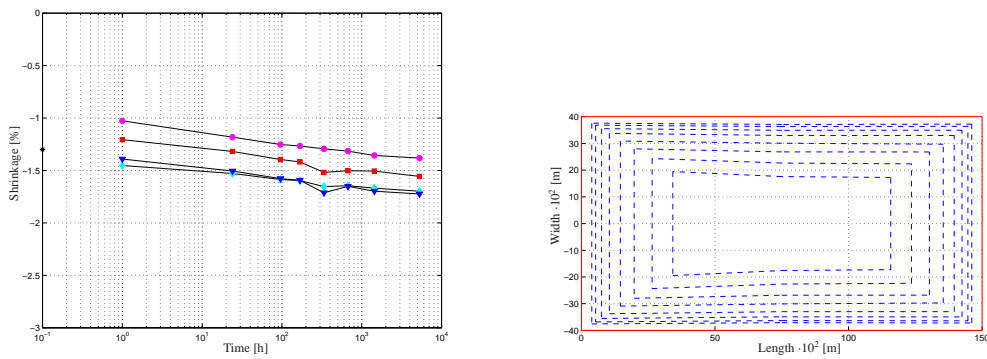


Fig. B.6: Shrinkage measurements performed at the positions as presented in fig. 5.1 (left), together with the magnified reproduction of the shape resulting from the shrinkage (right), for the processing conditions as shown in table B.1 (no.6). Bullet: longitudinal shrinkage, squares: width shrinkage near the gate, diamond: width shrinkage in between the gate and the end, and triangle: width shrinkage far from the gate.

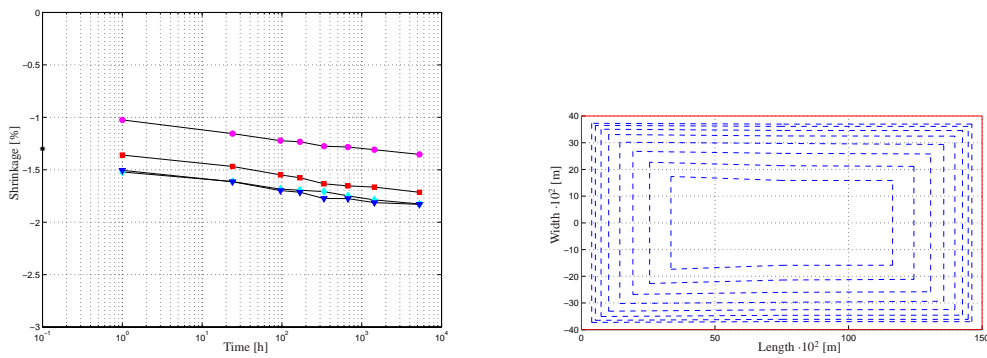


Fig. B.7: Shrinkage measurements performed at the positions as presented in fig. 5.1 (left), together with the magnified reproduction of the shape resulting from the shrinkage (right), for the processing conditions as shown in table B.1 (no.7). Bullet: longitudinal shrinkage, squares: width shrinkage near the gate, diamond: width shrinkage in between the gate and the end, and triangle: width shrinkage far from the gate.

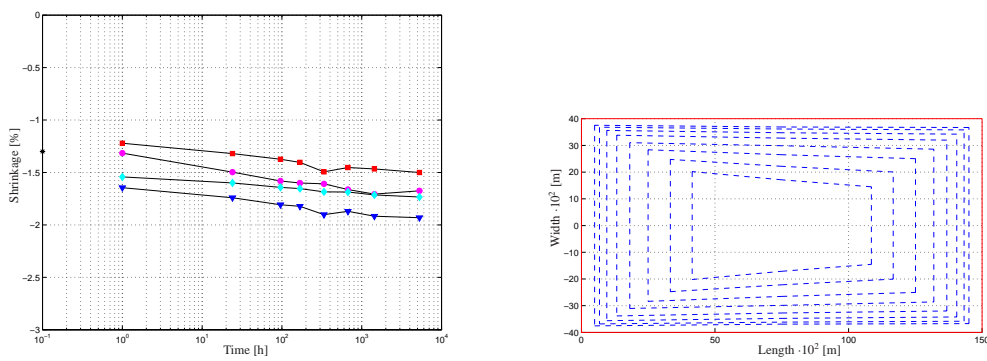


Fig. B.8: Shrinkage measurements performed at the positions as presented in fig. 5.1 (left), together with the magnified reproduction of the shape resulting from the shrinkage (right), for the processing conditions as shown in table B.1 (no.8). Bullet: longitudinal shrinkage, squares: width shrinkage near the gate, diamond: width shrinkage in between the gate and the end, and triangle: width shrinkage far from the gate.

Appendix C

Numerical results

A numerical study has been performed on the influence of different processing conditions on the distribution of the morphology in the final (injection moulded) product. Variations in the temperature of the melt injected, the volume flux during filling and the temperature of the mould wall have been used (see table C.1).

| no. | T_{inj} [K] | Q [m^3s^{-1}] | T_w [K] |
|-----|---------------|----------------------|-----------|
| 1 | 480 | $4.65 \cdot 10^{-4}$ | 333 |
| 2 | 430 | $4.65 \cdot 10^{-4}$ | 333 |
| 3 | 480 | $1.16 \cdot 10^{-4}$ | 333 |
| 4 | 430 | $1.16 \cdot 10^{-4}$ | 333 |
| 5 | 480 | $4.65 \cdot 10^{-4}$ | 293 |
| 6 | 430 | $4.65 \cdot 10^{-4}$ | 293 |
| 7 | 480 | $1.16 \cdot 10^{-4}$ | 293 |
| 8 | 430 | $1.16 \cdot 10^{-4}$ | 293 |

Tab. C.1: Numerical processing conditions as applied to study the influence of these conditions on the structure distribution and accompanying shrinkage, in which T_{inj} is the temperature of the melt injected, Q the volume flux during filling and T_w the temperature of the mould wall.

In this appendix the numerical results are presented for each combination of processing conditions. For example, for the numerical processing conditions applied as presented in table C.1 (no.1), the predicted morphology of the flow-induced oriented structure across the thickness of the injection moulded product close to the gate (top), far from the gate (bottom) and in between (middle) are presented in fig. C.1. At the left side the total shish-length is shown, at the right side the volume percentage oriented material.

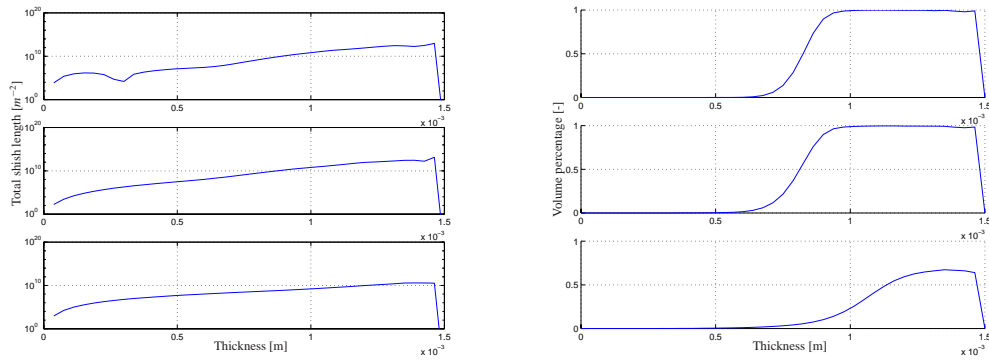


Fig. C.1: The distribution of the flow-induced oriented structure across the thickness of the injection moulded product close to the gate (top), far from the gate (bottom) and in between (middle), for the processing conditions as shown in table C.1 (no.1). At the left side the total shish-length is shown, at the right side the volume percentage oriented material.

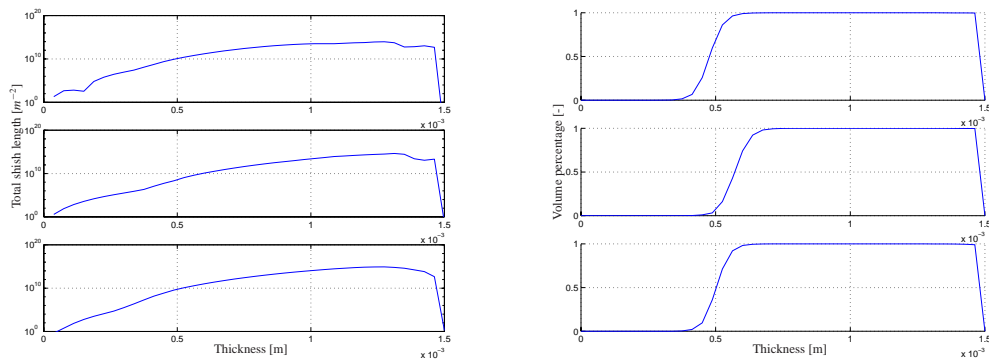


Fig. C.2: The distribution of the flow-induced oriented structure across the thickness of the injection moulded product close to the gate (top), far from the gate (bottom) and in between (middle), for the processing conditions as shown in table C.1 (no.2). At the left side the total shish-length is shown, at the right side the volume percentage oriented material.

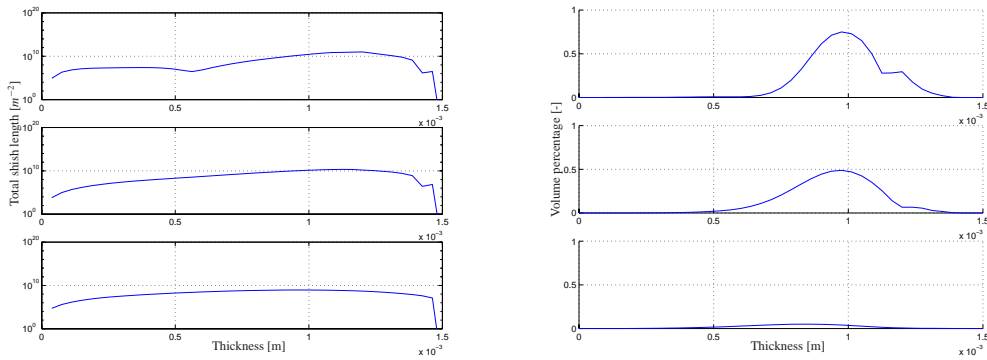


Fig. C.3: The distribution of the flow-induced oriented structure across the thickness of the injection moulded product close to the gate (top), far from the gate (bottom) and in between (middle), for the processing conditions as shown in table C.1 (no.3). At the left side the total shish-length is shown, at the right side the volume percentage oriented material.

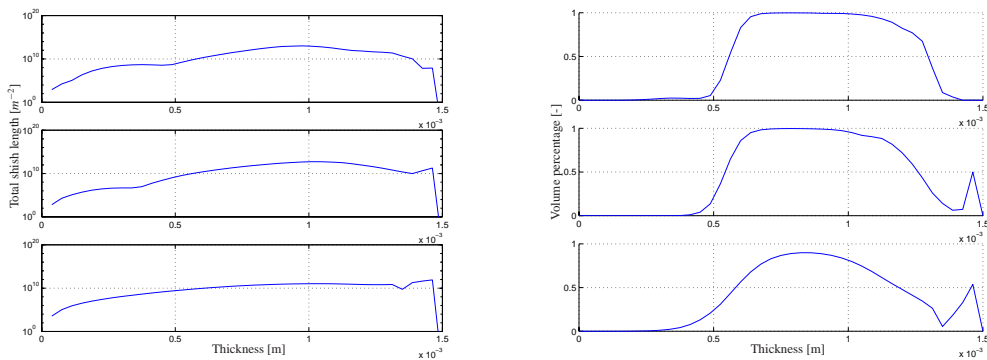


Fig. C.4: The distribution of the flow-induced oriented structure across the thickness of the injection moulded product close to the gate (top), far from the gate (bottom) and in between (middle), for the processing conditions as shown in table C.1 (no.4). At the left side the total shish-length is shown, at the right side the volume percentage oriented material.

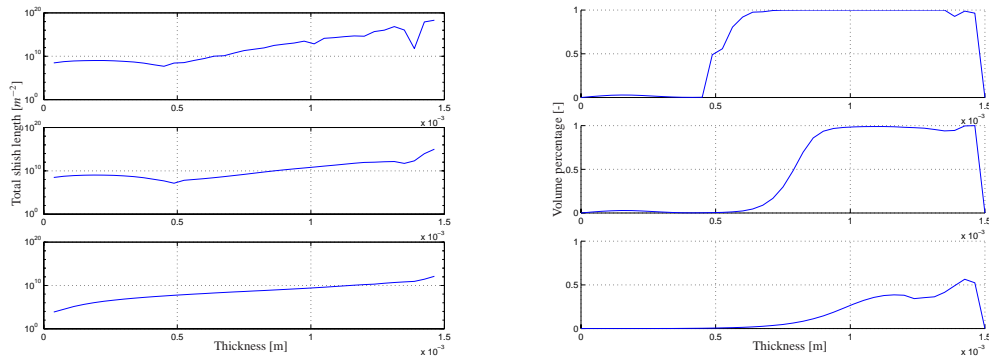


Fig. C.5: The distribution of the flow-induced oriented structure across the thickness of the injection moulded product close to the gate (top), far from the gate (bottom) and in between (middle), for the processing conditions as shown in table C.1 (no.5). At the left side the total shish-length is shown, at the right side the volume percentage oriented material.

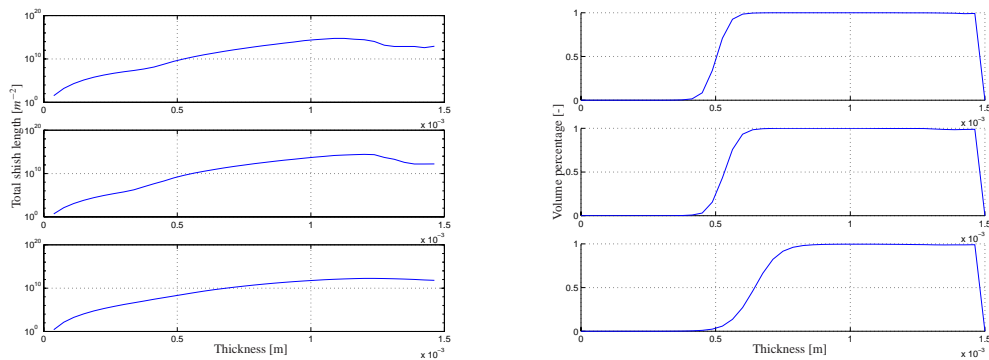


Fig. C.6: The distribution of the flow-induced oriented structure across the thickness of the injection moulded product close to the gate (top), far from the gate (bottom) and in between (middle), for the processing conditions as shown in table C.1 (no.6). At the left side the total shish-length is shown, at the right side the volume percentage oriented material.

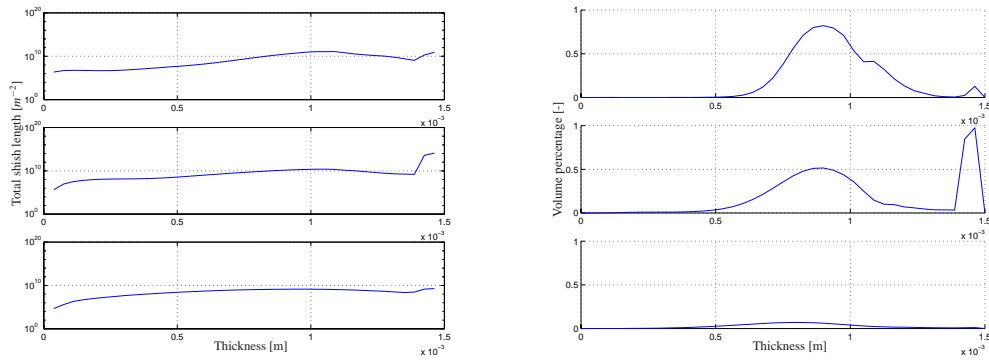


Fig. C.7: The distribution of the flow-induced oriented structure across the thickness of the injection moulded product close to the gate (top), far from the gate (bottom) and in between (middle), for the processing conditions as shown in table C.1 (no.7). At the left side the total shish-length is shown, at the right side the volume percentage oriented material.

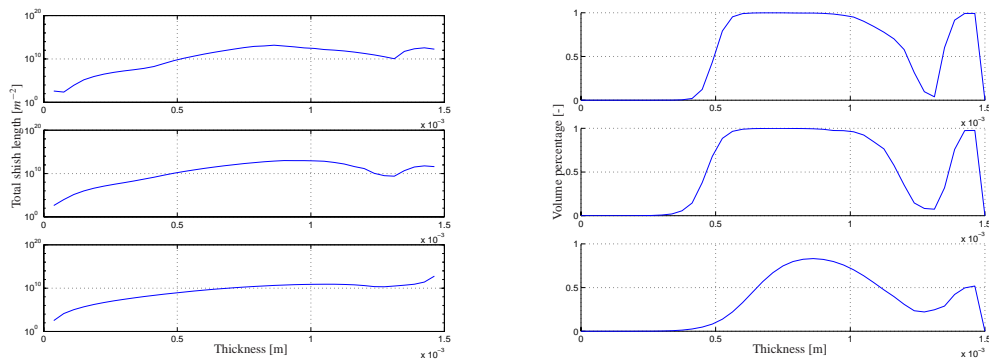


Fig. C.8: The distribution of the flow-induced oriented structure across the thickness of the injection moulded product close to the gate (top), far from the gate (bottom) and in between (middle), for the processing conditions as shown in table C.1 (no.8). At the left side the total shish-length is shown, at the right side the volume percentage oriented material.

Samenvatting

Het verwerken van semi-kristallijne polymeren tot een product resulteert in een interne verdeling van kristallijne structuren, die voor een groot deel verantwoordelijk is voor de mechanische eigenschappen van het betreffende product. Het voorspellen van deze structuur, en de ontwikkeling ervan, is echter nog steeds niet mogelijk, waardoor de invloed van de verschillende procescondities op het ontstaan van deze structuur alleen experimenteel kan worden onderzocht. De achterliggende fysica (het verband tussen de structuur en de eigenschappen) is daardoor, voor het merendeel, nog onbekend. Het modelleren van de structuurontwikkeling, tijdens en na het verwerken van semi-kristallijne polymeren, biedt de mogelijkheid de invloed van de verschillende procescondities op de ontwikkeling van de structuur te bestuderen. Deze berekende structuur kan experimenteel worden geverifieerd. De relatie tussen de structuur en de mechanische eigenschappen, zoals krimp en dimensie-stabiliteit, kan worden onderzocht door uit te gaan van de berekende structuur. Twee elementen van het modelleren van de structuurontwikkeling tijdens het verwerken van semi-kristallijne polymeren worden in dit proefschrift besproken: (i) een model voor de beschrijving van stromingsgeïnduceerde structuurontwikkeling, gebaseerd op de elastische rek in de polymere smelt, en (ii) een nieuwe experimentele techniek om het specifieke volume van semi-kristallijne polymeren te meten en de afhankelijkheid van de afkoelsnelheid en kristallisatie-kinetiek te bepalen.

Aangezien de nucleatie en groei van de kristalstructuur, die ontstaat in een stilstaande smelt tijdens het afkoelen (sferulieten), op een adequate manier is beschreven, kan de invloed van de verschillende procescondities, zoals afkoelsnelheid en druk, op de ontstane structuur worden berekend. Dit in tegenstelling tot de stromingsgeïnduceerde, geïënteerde structuren (shish-kebabs), waarvoor niet exact bekend was hoe deze zich ontwikkelen. In dit proefschrift zijn modellen voor de beschrijving van de sferuliet-groei en die van de groei van de geïënteerde structuren, op basis van afschuifsnelheid en de elastische rek in de smelt, geïmplementeerd in het numerieke simulatieprogramma VIP. Voor een volledig gekarakteriseerde polyamide en polypropyleen, zijn simulaties gedaan van kristallisatie zonder stroming, kristallisatie in een startende stroming en kristallisatie in een stationaire stroming. Deze resultaten zijn vergeleken met experimentele resultaten uit de literatuur. Het verschil tussen beide modellen voor stromingsgeïnduceerde kristallisatie wordt besproken, en enige zeer karakteristieke, uit de literatuur bekende fenomenen worden bestudeerd aan de hand van de beide modellen. Omdat het model dat gebaseerd is op de (materiaal gerelateerde) elastische rek, een betere beschrijving geeft van deze fenomenen, heeft het de voorkeur boven het model gebaseerd op de (proces gerelateerde) afschuifsnelheid.

De krimp van een polymeer tijdens en na het verwerken, bepaalt in hoge mate de dimensie-stabiliteit en de druk- en thermisch-geïnduceerde spanningen in het materiaal. Een juiste

beschrijving van het specifieke volume is nodig om deze krimp, afhankelijk van de thermo-mechanische geschiedenis van het materiaal, te kunnen berekenen. Voor amorfe polymeren worden verschillende (standaard) technieken gebruikt om het specifieke volume te meten als functie van de temperatuur en de druk, waarbij er veelal van wordt uitgegaan dat de dichtheid onafhankelijk is van de afkoelsnelheid. Voor semi-kristalijne polymeren ligt de zaak gecompliceerder, omdat het specifieke volume sterk afhankelijk is van de in het materiaal aanwezige structuur, die op zijn beurt sterk afhankelijk is van de thermo-mechanische geschiedenis. Standaard methoden voor het bepalen van het specifieke volume kunnen alleen worden gebruikt bij relatief lage afkoelsnelheden. Omdat tijdens het spuitgieten hoge afkoelsnelheden voorkomen in combinatie met hoge drukken, is een nieuwe experimentele methode ontwikkeld om bij relatief hoge afkoelsnelheden en drukken het volume te kunnen meten. Een experimentele opstelling, gebaseerd op de 'confining fluid method', is aangepast om afkoelsnelheden te halen van $60[K s^{-1}]$ en drukken tot $20 \cdot 10^6[Pa]$. Gebruikmakend van de gemeten temperatuur- en drukgeschiedenis en een model voor de beschrijving van de structuurontwikkeling en de invloed daarvan op het specifieke volume, creëerde de mogelijkheid de modelparameters te bepalen. Het vergelijken van het gemeten en berekende specifieke volume leidt tot de conclusie dat een juiste beschrijving van de structuur als vanzelf leidt tot een juiste voorspelling van het specifieke volume. Het gebruik van een gecombineerde numerieke en experimentele benadering is hiervoor essentieel.

Beide elementen zijn gebruikt in numerieke simulaties van het spuitgieten van semi-kristalijne polymeren. Zowel het nieuwe model voor de beschrijving van stromingsgeïnduceerde kristallisatie, als de nieuwe methode om het specifieke volume van semi-kristalijne polymeren te bepalen en te beschrijven, zijn toegepast om de structuur te beschrijven (i) in een SCORIM proces (een methode van spuitgieten waarin de stroming in een gevulde matrijs gehandhaafd blijft tijdens koelen teneinde de mechanische eigenschappen van het product te verbeteren), (ii) in een strip, gefabriceerd door middel van spuitgieten bij verschillende procescondities, en (iii) in relatie met dimensie-stabiliteit. Het toepassen van SCORIM verduidelijkt de invloed van de mechanische (stromings-) geschiedenis op de structuurverdeling in het product. Een voorbeeld hiervan is de mogelijkheid een laminaat te creëren, bestaande uit een aantal lagen geïoriënteerd materiaal, met daartussen lagen niet-geïoriënteerd materiaal. Omdat procescondities tijdens het spuitgieten van semi-kristalijne materialen, zoals de injectietemperatuur, de injectiesnelheid en de matrijstemperatuur, een grote invloed kunnen hebben op de structuurontwikkeling en -verdeling, is een studie uitgevoerd naar de effecten hiervan. Aangezien het gebruikte materiaal een nucleatie-initiator bevat, hebben de verschillende procescondities geen invloed op de morfologie van de kern van het product. Daarom is vooral de invloed van de procescondities op de dikte van de laag geïoriënteerd materiaal aan het oppervlak van het product onderzocht. Experimenteel en/of numeriek zijn de volgende trends waargenomen: (i) een hogere injectietemperatuur en (ii) een hoger injectiesnelheid verlagen de dikte van de (stromings-geïnduceerde) geïoriënteerde laag, terwijl (iii) de matrijstemperatuur bijna geen invloed heeft op de dikte van deze laag. Echter, enige invloed van de matrijstemperatuur is waargenomen in de experimenteel bepaalde krimp.

Aangezien de structuur (-verdeling) in een semi-kristalijn product kan worden berekend, kan de krimp tijdens en na verwerking worden bepaald, indien de krimp van zowel het niet-

geöriënteerde als het geöriënteerde materiaal bekend is. Omdat deze niet voor handen zijn op dit moment, is dit belangrijke deel van het onderzoek noodgedwongen een onderdeel van een toekomstige studie.

Acknowledgments

The work presented in this thesis was conducted within the framework of the BRITE-EURAM III project BE 95-2067 'Structure Development during Solidification in the Processing of Crystalline Polymers' (DECRYPO) with financial support by the European Commission and the Dutch Polymer Institute. We would like to thank Dr. G. Eder (Linz University, Austria) and Dr. M. Gahleitner (Borealis, Austria) for their support in the development of the strain based model for flow-induced crystallization (chapter 3). The experimental setup presented in chapter 4 to study the influence of cooling rate on pVT-behavior of semi-crystalline polymers, was initiated by Prof.Dr.Ir. F.P.T. Baaijens at Philips, and made to work by Mr. J.J.F.J. Garenfeld. We owe them for their contribution.

Graag wil ik een ieder bedanken, die een bijdrage heeft geleverd aan dit proefschrift. In de eerste plaats Gerrit Peters, voor de manier waarop we hebben geprobeerd onze groep op de kristallisatie wereldkaart te zetten. Tevens Han Meijer, voor de ondersteuning hierin, en voor de mogelijkheden stages te lopen en congressen te bezoeken. Beiden wil ik ook bedanken voor de manier waarop ze mij 'scherp' hebben gehouden aangaande het onderwerp. Mijn dank gaat ook uit naar diegenen die hun stages en afstuderen bij mij hebben uitgevoerd (in chronologische volgorde): Lesly Bloem, Edwin Wijnhoven, Andrea Giugno en Mariavittoria di Stasi. Verder ben ik dank verschuldigd aan de mensen die digitaal mijn promotiewerkzaamheden hebben ondersteund: Leo Wouters, Patrick van Brakel en Peter Kruijt. Uiteraard zijn ook mijn kamergenoten en overige collega's door de jaren heen van groot belang geweest om de zinnen te verzetten. Echter, de meeste dank ben ik verschuldigd aan Marike, die in zowel de rustige als drukke tijden, van essentieel belang is geweest. Allen: BEDANKT!

Curriculum Vitae

- 20-12-1970 Born in Steenwijk, the Netherlands.
- 1983 - 1989 R.S.G. Jan Hendrik Tromp Meesters Scholengemeenschap,
Steenwijk (grammar school).
- 1989 - 1991 H.T.S. Zwolle, Department of Mechanical Engineering.
- 1991 - 1996 Eindhoven University of Technology, Masters degree at
the department of Mechanical Engineering.
- 1996 - 2000 Research assistant at Materials Technology,
Dutch Polymer Institute, Eindhoven University of Technology.